CHARACTERIZATION AND STRUCTURAL MODELING OF MAGNESIA-ALUMINA SPINEL GLASS TANK REFRACTORIES

Final Report for the Period October 1, 2001 – October 1, 2003

October 2003

William L. Headrick, Robert E. Moore, Musa Karakus, Xiaoting Liang

University of Missouri-Rolla
Rolla, MO 65409

Mattison K. Ferber, James G. Hemrick

Oak Ridge National Laboratory
Oak Ridge, TN 37831

This material is based upon work supported by the U S. Department of Energy under Award No. DE-FC07-01ID14250.

Executive Summary

Furnace designers and furnace/refractories engineers recognize that improved optimization of furnace superstructure design and the use of appropriate refractories are needed as glass production furnaces are continually driven toward greater output and energy efficiencies (and concomitant harsher operating conditions). The conversion to oxy-fuel from traditional air-fuel-firing is a means to meet these objectives. Refractories for both oxy- and air-fuel-fired furnace superstructures are subjected to high temperatures during service and may appreciably creep or subside if the refractory material is not creep resistant or if it is subjected to high stress. Furnace designers can ensure that superstructure structural integrity is maintained or predicted if the creep behavior of the refractory material they are using is well-understood and well-represented by appropriate engineering creep models.

Several issues currently limit the abilities of furnace designers to choose the best refractory for their application, optimize the engineering design, or predict the service mechanical integrity of their refractory superstructures. Published engineering creep data are essentially nonexistent for almost all commercially available refractories used for glass furnace superstructures, and the various refractory suppliers supply the limited data that does exist. Unfortunately, these suppliers typically conduct their mechanical testing differently, and interpret and report their obtained data differently, making it difficult for furnace designers to compare competing grades of candidate refractories in an equitable fashion. Furthermore, the refractory supplier's data is often not in an available form that can be used for furnace design, modeling, or the prediction of long-term structural integrity of furnace superstructures.

The intent of this project was to meet needs in the topical areas of the Energy Efficiency and Environment. For example the application of oxy-fuel fired furnaces for glass production have several benefits over the use of currently used regenerative furnaces. The NO_x emission is an order of magnitude less for oxy-fueled furnaces compared to conventional regenerative furnaces. The particulate level is much less as well. The capital cost per ton of glass pulled is approximately 50% and 67% less for oxy-fueled furnaces compared to conventional regenerative and all electric furnaces, respectively. The downside to oxy-fuel fired furnaces is that their higher operating temperatures and alkali partial pressures in an oxygen-rich environment hastens alkali-induced corrosion (particularly in silica refractories); this necessitates that refractories with both increased creep and corrosion resistance be used in their superstructure. Through this project, the high temperature mechanical behavior of spinel refractories was quantified and modeled to aid in the efficient design of furnace superstructures; thus, realizing the beneficial energy and pollutant savings oxy-fuel firing may yield.

Goals

The completion of this project was intended to result in the generation of a database of the high temperature mechanical, thermal and chemical behaviors of spinel crown refractories so furnace superstructures can be more efficiently designed; thus, realizing the energy savings and pollutant abatement that oxy-fuel firing may yield. The resulting database will be used in three ways. First, it will be made available to the glass manufacturers for assisting them in the selection of the appropriate refractory for their furnaces. Second, the data will be used to refine existing models describing the stress, temperature and microstructural dependencies of the creep rate. Third, the data will be used in conjunction with finite element analysis (FEA) to predict the time-dependent deformation of a glass-tank crown. Note that in the present study, the model will not only account for creep effects, but the influence of time-dependent changes in the key thermal properties and corrosion as well. In the case of the thermal properties, time-dependent changes in thermal expansion and thermal conductivity will be used to estimate time-dependent changes in the temperature and stress-state. As a first approximation, the affect of corrosion will be accounted for by assuming that it leads to a uniform loss of the crown structure. This information will be used in conjunction with FEA to calculate the changes in the stress-state arising from the loss of structure.

Task 1: Assessment of Compressive Creep Behavior

Engineering creep data for selected refractory materials was generated to a temperature of 3000°F (1650°C) in ambient air. A specially-designed testing frame was used for the project. As shown in Figure 1, the frame consisted of a large clamshell resistance-heated furnace, a contacting extensometer for precise measurements of the axial-dimension-changes, and silicon carbide (SiC) push rods. The SiC push rods were subsequently replaced with fusion-cast spinel rods to eliminate unfavorable chemical reactions between the push rods and the test sample at high temperatures.

Extensometry methods, other than the capacitance contacting extensometers proposed for this project (Figure 2), are often used for the measurement of refractory creep. However, the capacitance contacting extensometer circumvents problems other techniques inherently possess[1]. The deformation of refractories is frequently measured continuously during compressive creep testing using two (sometimes more) linear variable differential transducers (LVDTs) whose mutual displacement coincide with the continuous position of the specimen ends[2,3]. The creep results generated from this technique are accurate only as long as the accumulated measured deformation coincides with the actual specimen heights measured before and after testing. Deformation and/or translation of the load train during the creep testing of the specimen, reaction of the specimen ends with

[1] J.G. Hemrick and A.A Weresczcak, "Creep Measurement and Analysis of Refractories", Fundamentals of Refractory Technology, Ceramic Transactions, Vol. 125, (2001).

[2] S. Shin and O. Buyukozturk, Material Property Development for Refractories, US DOE Report ORNL/Sub/79-07862/02 (1990).

[3] "Standard Test Method for Load Testing Refractory Brick at High Temperatures," ASTM C16, Vol. 15.01, American Society for Testing and Materials, West Conshohocken, PA, 1998.

the fixturing, and "bedding-down" of the specimen all have been shown to cause a lack of correlation between the measured deformation during testing and the change in pre- and post-test specimen height. If any of these events are occurring then the measured contraction during testing is not solely due to creep. Consequently, caution must be exercised when interpreting deformation data generated using this LVDT technique, because it will only be representative creep data if the experimenter verified and correlated pre- and post-test specimen height with the accumulated measured deformation. The advantage of the contacting extensometers used in the present study is their accurate operation is independent of any rigid body motion or deformation of the test hardware, specimen (*e.g.*, "end-crushing") and push rods.

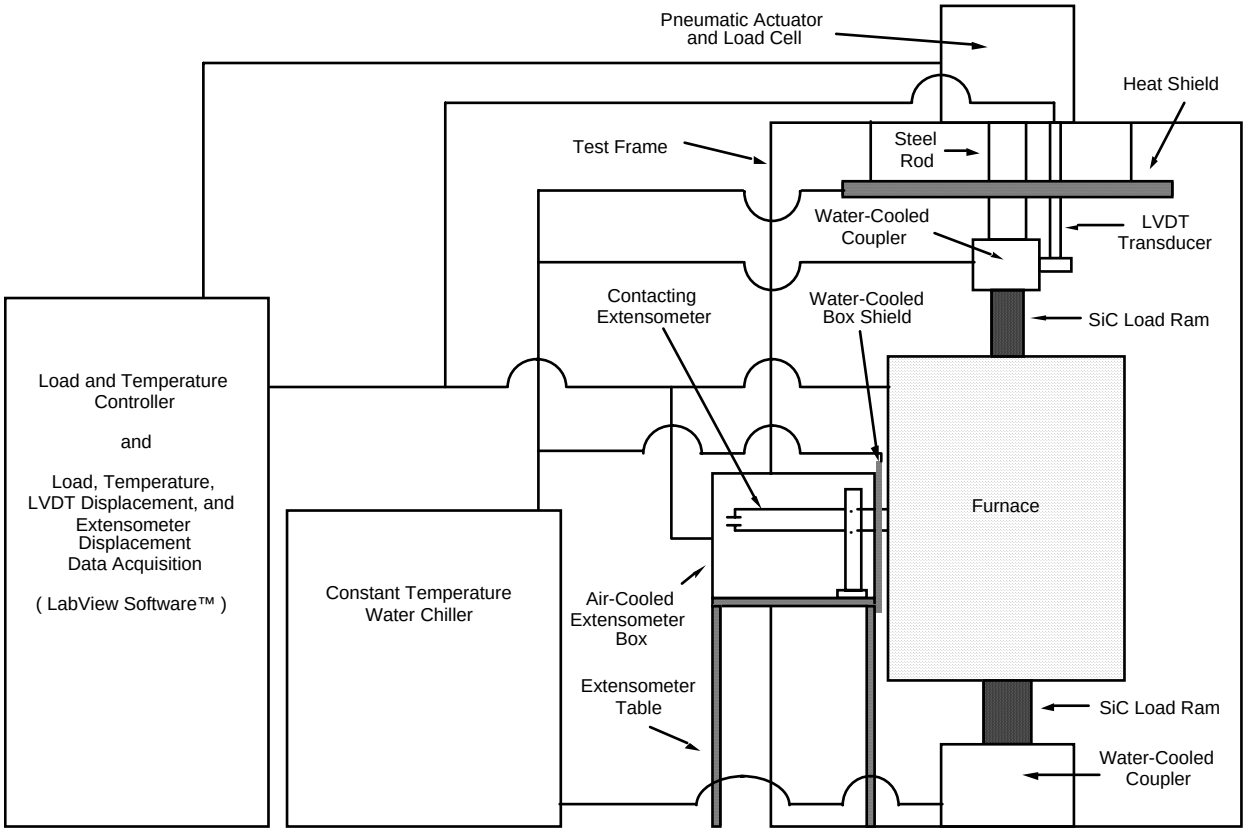

Figure 1 Schematic of CCF1 and Supporting Instruments.

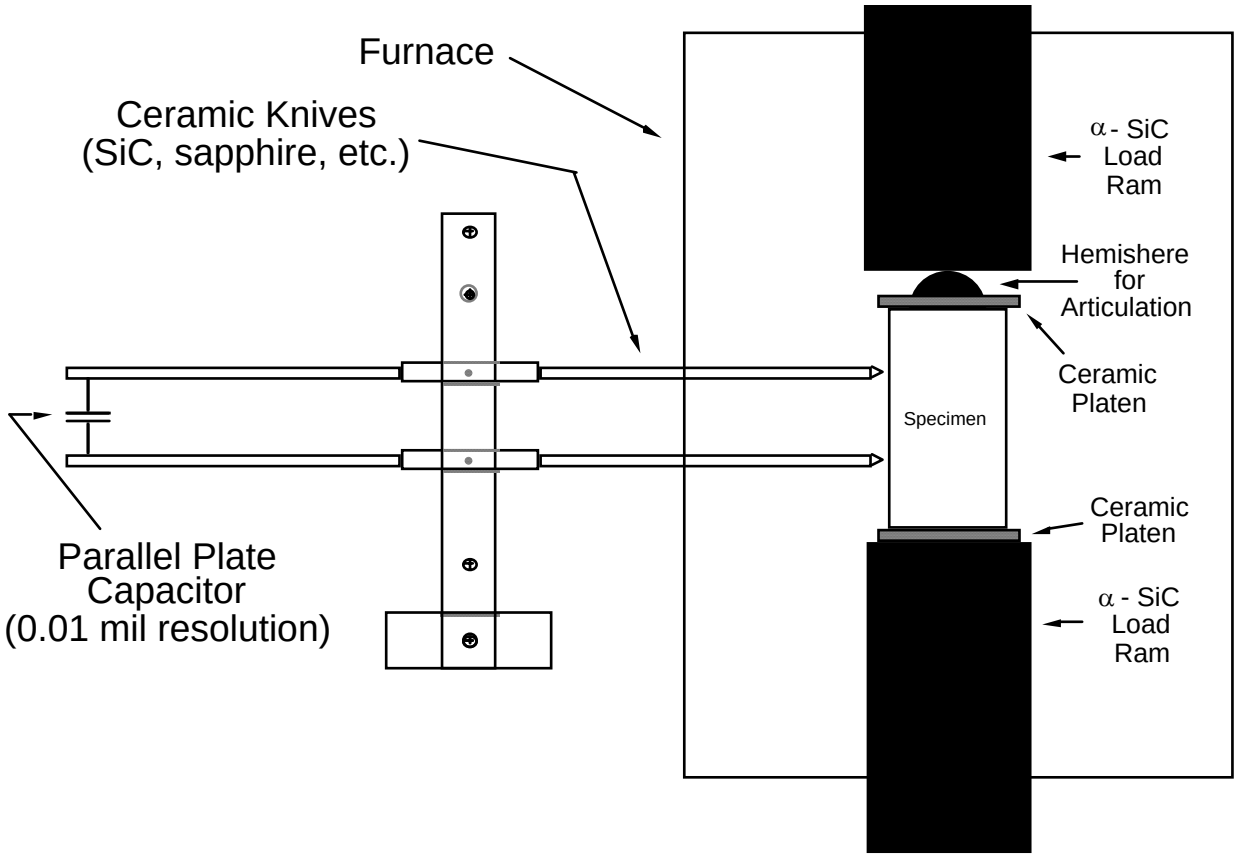

Figure 2 Schematic of CCF1's Extensometer Layout.

Modifications to the creep apparatus have been required to address corrosion issues in previous programs, such as those to measure creep of alumina refractories specimens which emitted substantial quantities of Na_2O vapor, which attacked components of the test furnace. To generate valid data, a specially designed shroud was required to encase the test specimens and thus minimize loss of Na_2O vapor (Figure 3). Such an arrangement was not found to be necessary in the present testing.

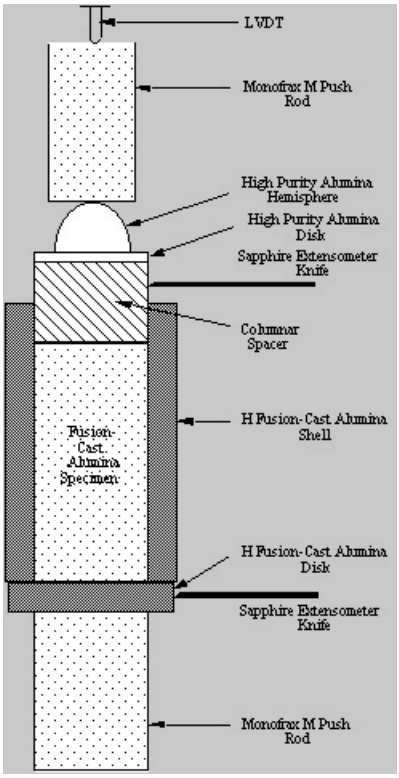

Figure 3 Shroud Arrangement used to Minimize Na_2O Vapor Attack During Creep Testing.

Most creep analyses for long-term applications (*i.e.*, where steady state creep accumulation dominates the accumulation of strain, not the amount of primary creep) involve the determination of a steady-state or minimum creep rate and its examination as a function of applied stress and temperature. The steady-state or minimum compressive creep rate ($d\varepsilon/dt_{min}$) can be related to the applied compressive stress and temperature by an empirical Arrhenius power law or the familiar Norton-Bailey creep equation[4]:

$$d\varepsilon/dt_{min} = A\ \sigma^n \exp(-Q/RT), \qquad [1]$$

where A is a constant, σ is the applied stress, n is the stress exponent, Q is the activation energy, R is the gas constant and T is the absolute temperature. Multilinear regression may be performed to determine the constants A, n and Q for each material. By performing the analysis in this manner, it is implied the same dominant (or rate-controlling) creep mechanism is active at all temperatures and stresses. Recent data generated at ORNL indicate the time-dependent changes in the microstructure (grain size and phase composition) can lead to either shrinkage or expansion of the material in the absence of an applied stress for some refractories [1,5]. As a first approximation Equation 1 can be modified to account for this effect by including a second temperature-dependent term,

---

[4] F. H. Norton, The Creep of Steel at High Temperature, McGraw Hill, New York, 1929.

[5] A.A. Wereszczak, M. Karakus, K.C. Liu, B.A. Pint, R.E. Moore and T.P. Kirkland, "Compressive Creep Performance and High Temperature Dimensional Stability of Conventional Silica Refractories" ORNL/TM-13757, March 1999.

$$d\varepsilon/dt_{min} = A\ \sigma^n \exp(-Q_c/RT) + B \exp(-Q_a/RT), \quad [2]$$

where Q_c is the activation energy for creep and Q_a is the activation energy for the microstructural-dependent aging. The validity of this model will be assessed for the materials examined in this project. If necessary other creep expressions will be evaluated as well.

Task 2: Corrosion testing

Corrosion rates are often measured using the ASTM "lid test" in which refractories of interest are placed over a crucible containing the appropriate glass composition and heated in a conventional furnace[6]. Unfortunately, this method does not adequately simulate then effects of the combustion environment which is particularly important for oxy-fuel fired furnaces. Based upon suggestions from members of the Glass Industry Advisory Committee (GIAC), a glasstank simulator was used to expose specimens to the environment in an actual glasstank. In this simulator, which is currently in use at UMR, combustion gases are generated in a simulative glass tank that is melting glass with oxy-fuel firing. Test samples are located on ledges protruding from the side walls in the vicinity of the crown. Corrosion is evaluated by conducting detailed microstructural analysis of samples before and after exposure.

Task 3: Thermal Conductivity Measurements

Temperature is a key factor in determining the rates of corrosion and creep. In order to predict these temperatures, one must know the thermal properties of the refractories and how these properties change with time. The purpose of this task was to measure the thermal expansion and thermal conductivity of the same refractories used in the creep testing.

Task 4: Microstructural and Phase Analysis

The specimens generated in Tasks 1-3 were subjected to detailed microstructural and phase analysis. One objective of this task was to better understand how creep and corrosion behavior relates to microstructure and microchemistry. For example, in the case of creep, grain size and distribution are expected to be a major factor in determining creep resistance. A second objective is to correlate changes in the microstructure and microchemistry with changes in the thermal conductivity.

Disks were sectioned from core-drilled “as-received” specimens, as well as from specimens subjected to creep and corrosion testing, in preparation for reflected light (RL) and cathodoluminescence (CL) imaging. The disk sections were then polished using well

[6] “Standard Practice for Vapor Attack on Refractories for Furnace Superstructures,” ASTM C987, Vol. 15.01, American Society for Testing and Materials, West Conshohocken, PA, 1998.

established metallographic techniques. The CL microscopy characterization technique has been described in detail by Karakus and Moore but is briefly described here[7]. The CL imaging system utilizes an energetic electron beam that is produced from a cold cathode ray tube. The electron beam is trained on the surface of uncovered polished or unpolished specimens in a low vacuum environment. As a result of the electron beam-solid specimen interaction, minerals or phases in the specimen produce characteristic colored light known as "cathodoluminescence." The CL technique is unique in that it often provides microstructural information that cannot be obtained by any other technique. The CL microscopy system can provide immediate assessment of the phases in refractory materials through the identification of characteristic CL color and crystal habits minerals exhibit. The CL microscopy system can also be used in conjunction with RL and SEM for elemental analysis of individual phases.

Certain minerals produce characteristic CL color. For example, corundum (α-Al_2O_3) is characterized by a characteristic bright red CL color while spinel ($MgAl_2O_4$) produces a characteristic green color. These CL emissions are due to "activator" elements present in trace amounts in these mineral structures; Cr^{3+} in corundum produces a characteristic CL emission at approximately 694 nm and tetrahedrally coordinated Mn^{2+} in spinel produces a CL emission at approximately 520 nm. Activator elements related to CL emission centers in these minerals often require low voltages ($\approx$ 8kV) for excitation.

Task 5: Modeling and Verification

In this task, FEA was used to model the glass tank crown structure. The required boundary conditions for this exercise were based on input from the glass and refractory manufacturers. Note that in the present study, the model not only accounts for creep effects, but the influence of time-dependent changes in the key thermal properties and corrosion as well. In the case of the thermal properties, time-dependent changes in thermal expansion and thermal conductivity were used to estimate time-dependent changes in the temperature and stress-state. As a first approximation, the affect of corrosion was accounted for by assuming it leads to a uniform loss of the crown structure. This information was used in conjunction with FEA to calculate the changes in the stress-state arising from the loss of structure.

This model can initially be applied to existing glass-tank refractories such as those based on silica using creep and thermal property data available from a previous study. Glass tank manufacturers were asked to evaluate the initial predictions generated by the model based upon there own experience. Once the model was verified, it was then applied to the more advanced refractories evaluated in this project. The model, will also be made available to the glass manufacturers for application to their specific furnaces, for; (1) the optimization of crown geometry, (2) selection of the most cost effective refractory, and (3) estimation of the expected lifetime.

---

[7] M. Karakus and R. E. Moore, "CLM - A New Technique for Refractories," *Ceramic Bulletin*, **77** 55-61 (1998).

Project Summary

Task Identification Number	Description	Planned Completion Date	Actual Completion Date
1	Creep	July 2002	September 2003
2	Corrosion	March 2002	May 2002
3	Thermal Conductivity	June 2002	March 2003
4	Microstructural Analysis	July 2002	July 2002
5	Modeling	August 2002	June 2003

Results

Task 1: Assessment of Compressive Creep Behavior

Engineering creep data for selected refractory materials was generated to a temperature of 1650°C (3000°F) in ambient air. Tests for the fusion cast material were performed at 1650°C and 3.0 MPa as shown in Figure 4. One test was run on bulk material and one was run on material with a longitudinal columnar structure running parallel to the loading direction. There is some initial movement seen in both samples due to the application of the load (the samples were heated to temperature under low load (30-50lbs) and allowed to dwell for 24 hours before the main load (768.909lbs) was applied), then very little creep over the time of testing. The test frame was re-fitted with a larger air cylinder and load cell, to enable testing at higher loads in an attempt to increase the amount of measurable creep generated. Also examined was the effect of using smaller samples to obtain higher loads, but this concept was deemed not feasible due to the large grain sizes of the refractory materials under investigation.

The behavior exhibited by the transverse columnar structure (columnar structure running perpendicular to the loading direction) was not as expected, Figure 4. It was expected that it would be similar to the behavior of the longitudinal columnar sample with maybe even less accumulated strain. Instead, the behavior is more similar to that of the bulk structure with about the same amount of total accumulated strain but a slower initial rate of strain accumulation. Curves from two separate samples both show the same initial strain accumulation, showing that this data is repeatable.

Rather than analyzing the final 100 hours of the test, all the data available past 100 hours of testing, shown in Figures 4-7, was analyzed, shown in Table 1. This provided a better representation of the apparent "steady-state" creep rates exhibited by these materials. One conclusion was that the fusion-cast material does not appreciably creep (even at 8.5 MPa). There was more initial strain due to application of the load (about 3% more which corresponds with the increase from 3 to 8.5 MPa), but there was not a change in "steady-state" creep rate with the increased load. The creep rate for the longitudinal columnar structure was lower, but the transverse columnar structure showed a similar creep rate to the bulk structure.

Table 1 Calculated Strain Rates

Material	Temperature	Stress	Strain Rate
Fused Spinel Longitudinal Columnar	1650 C	3.0 MPa	1.27×10^{-6}/h
Fused Spinel Transverse Columnar	1650 C	3.0 MPa	4.27×10^{-6}/h
Fused Spinel Bulk	1650 C	3.0 MPa	5.66×10^{-6}/h
Fused Spinel Bulk	1650 C	8.5 MPa	5.00×10^{-6}/h
Bonded Spinel Bulk	1650 C	0.07 MPa	48.0×10^{-6}/h
Bonded Spinel Bulk	1550 C	0.06 MPa	8.89×10^{-6}/h
Bonded Spinel Bulk	1550 C	0.3 MPa	23.8×10^{-6}/h

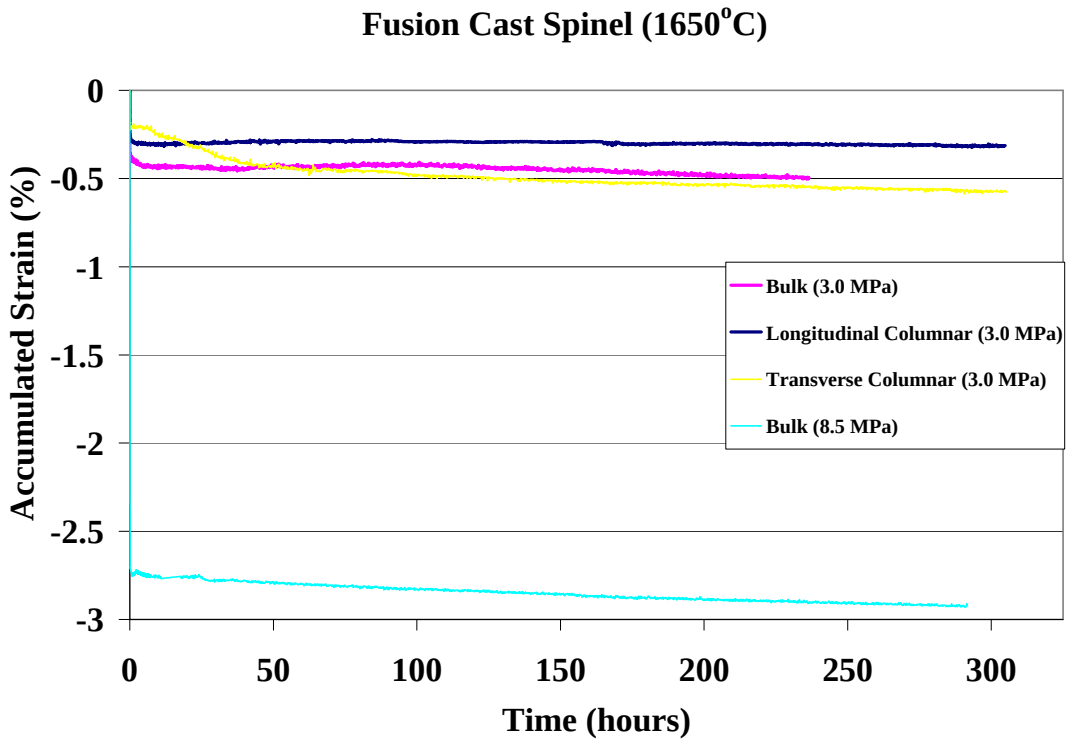

Figure 4 Fused Spinel Accumulated Strain Curves.

The bonded material did show significant creep (even at low stresses and temperatures) and was deemed far inferior in creep resistance to the fusion-cast as shown in Figures 5-7. Initial testing was planned at 1650°C and 3.0 MPa, but application of the load resulted in immediate failure of the sample as shown in Figure 5. Even under a nominal preload of 0.07 MPa, the bonded material experienced creep greater than that seen in the fusion-cast samples at much higher stresses and a greater "steady-state" creep rate a shown in Table 1. Testing at a lower temperature of 1550°C and a stress of 0.06 MPa also resulted in measurable levels of creep as shown in Figure 6 and a similar "steady-state" creep rate to that seen in the fusion-cast materials at higher temperatures and stresses (see Table 1). Finally, a sample was tested at 1550°C and 0.3 MPa. This sample showed considerable creep (as shown in Figure 7) and a much greater "steady-state" creep rate than what was previously measured (as given in Table 1).

Due to the difficulty in generating measurable creep in the fusion-cast samples, regression of the data for fitting with the Norton-Bailey Arrhenius creep relationship was not possible. Data from the testing of the bonded specimens (as shown in Table 1) was analyzed through regression and fit to the Norton-Bailey Arrhenius creep relationship. This analysis resulted in a calculated stress exponent of 0.6 and an activation energy of 110 kcal/mole. These values are plausible as a stress exponent of approximately 1.0 would be indicative of diffusion controlled creep and the calculated activation energy is on the order of that of fine-grained alumina (≈130 kcal/mole).

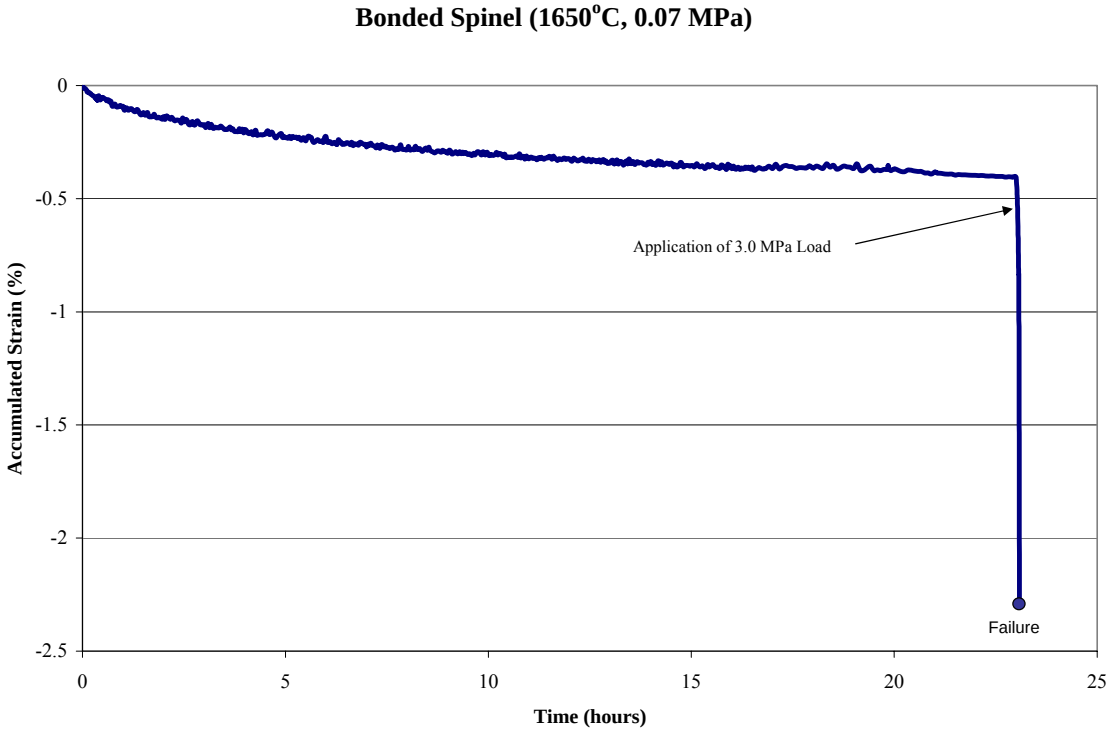

Figure 5 Bonded Spinel Accumulated Strain Curve at 1650°C.

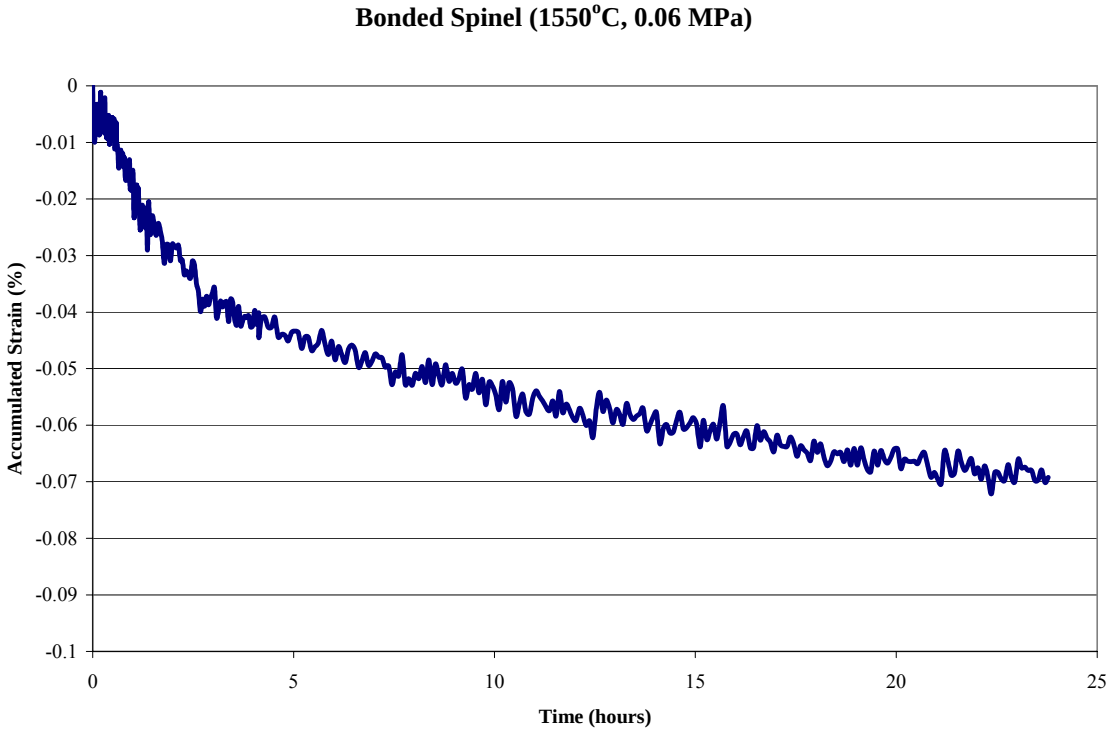

Figure 6 Bonded Spinel Accumulated Strain Curve at 1550°C.

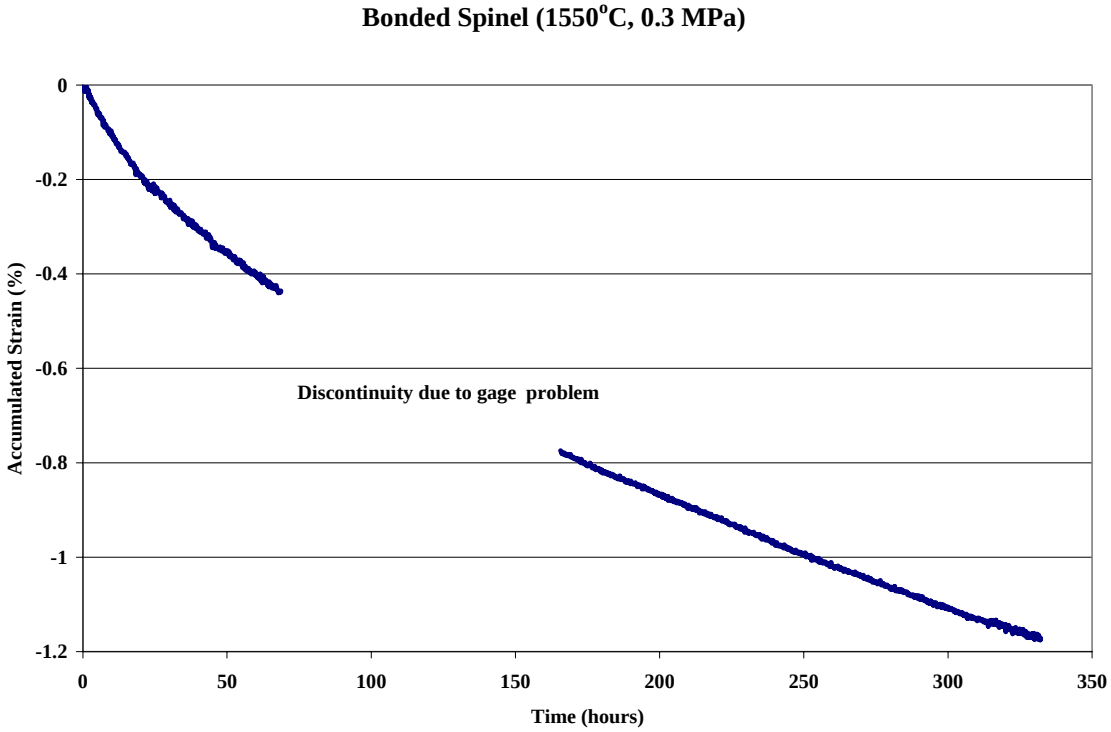

Figure 7 Bonded Spinel Accumulated Strain Curve at 1550°C.

Task 2: Corrosion testing

A glasstank simulator was used to expose the specimens to the environment in an actual glasstank. In this simulator combustion gases were generated by melting glass with oxy-fuel firing. Test samples were located on ledges of zircon protruding from the side walls in the vicinity of the crown. Corrosion is evaluated by conducting detailed microstructural analysis.

Task 3: Thermal Conductivity Measurements

Refractory materials will be subjected to elevated temperatures where rates of corrosion and creep will be of importance. In order to fully predict behavior at these temperatures, one must know the thermal properties of the refractories and how these properties change with time. The purpose of this task was to measure the thermal conductivity of the same refractories used in the creep testing. Thermal diffusivity measurements were completed by the laser flash method.

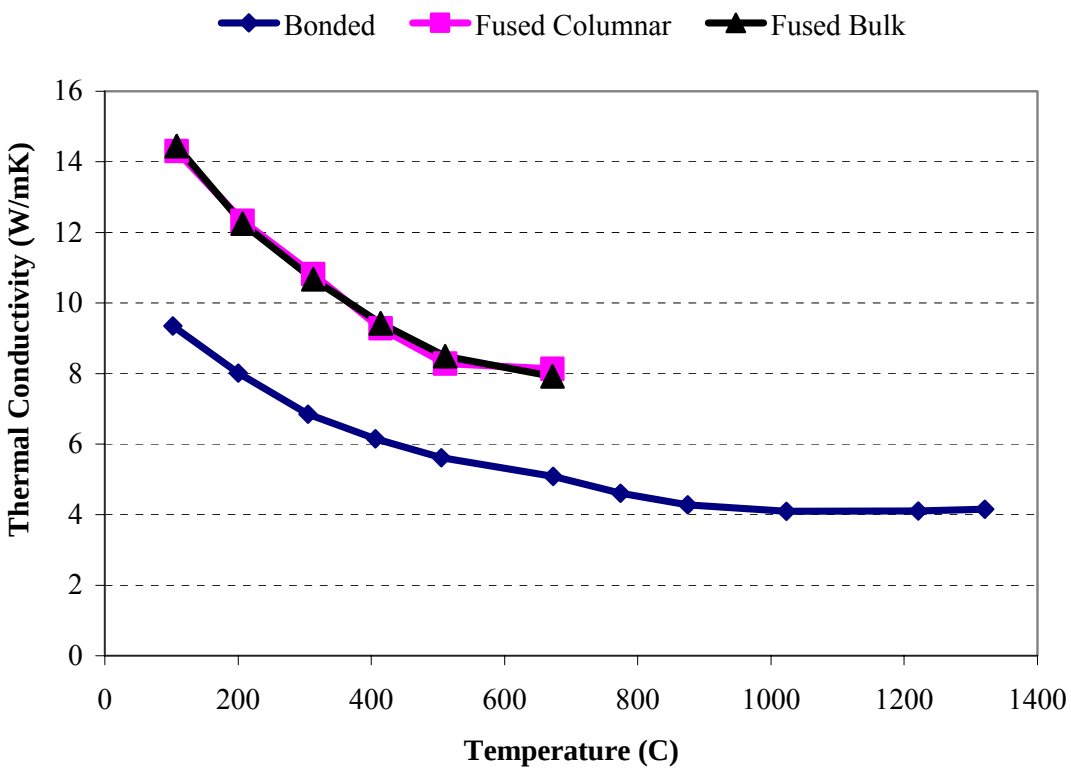

Figure 8 Calculated Thermal Conductivity of Fused and Bonded Spinel from Laser Flash Diffusivity

Density and thermal diffusivity are required as input into the calculation of thermal conductivity. The density of the fused cast spinel was measured as 3.47 g/cc with a porosity of 2.3%, the density of the columnar structure and bulk structure were 3.47 g/cc and 3.5 g/cc with porosities of 2.1% and 2.5%, respectively. The density of the bonded spinel was measured as 3.04 g/cc with a porosity of 14.2%. Thermal diffusivity results are shown in Figure 9. As expected, thermal diffusivity/conductivity is seen to decrease with increasing temperature. This is characteristic of most ceramic materials. The thermal diffusivity of the fused materials could not be measured above 800°C due to transparency of the material to the laser wavelength used.

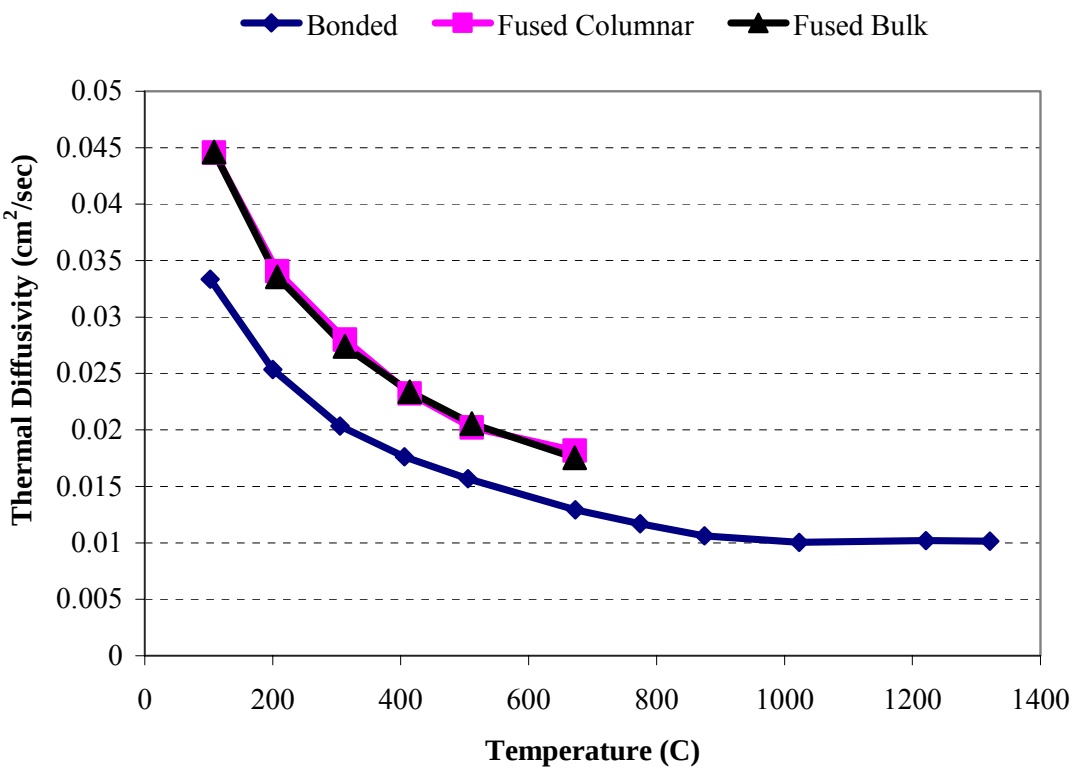

Figure 9 Thermal Diffusivity of Fused and Bonded Spinel

Task 4: Microstructural and Phase Analysis

The specimens generated in Tasks 1-3 were subjected to detailed microstructural and phase analysis. One objective of this task was to better understand how creep and corrosion behavior relates to microstructure and microchemistry. For example, in the case of creep, grain size and distribution were expected to be a major factor in determining creep resistance. A second objective was to correlate changes in the microstructure and microchemistry with changes in the thermal conductivity.
Two different spinel refractory materials are studied by RL/CL microscopy and X-ray diffraction to determine the unusual microstructural features that would affect the creep behavior of the materials. Samples of sintered spinel brick included specimen SB, STB and CB. Specimen ST, STT and CT are identified as fused spinel block.
XRD showed little differences in the patterns between the “as supplied” and “exposed samples” as shown in Figure 10 and Figure 11. There were no additional phases found after exposure in the simulative glasstank.

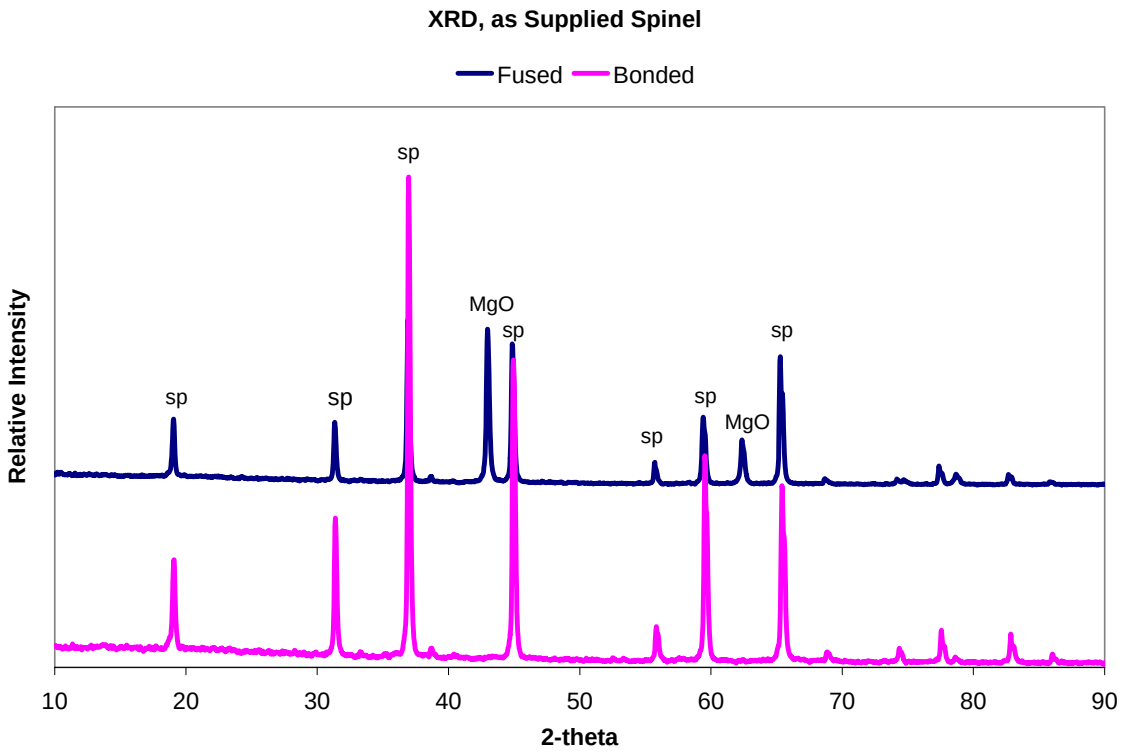

Figure 10 XRD of Bonded and Fused Spinel, as supplied.

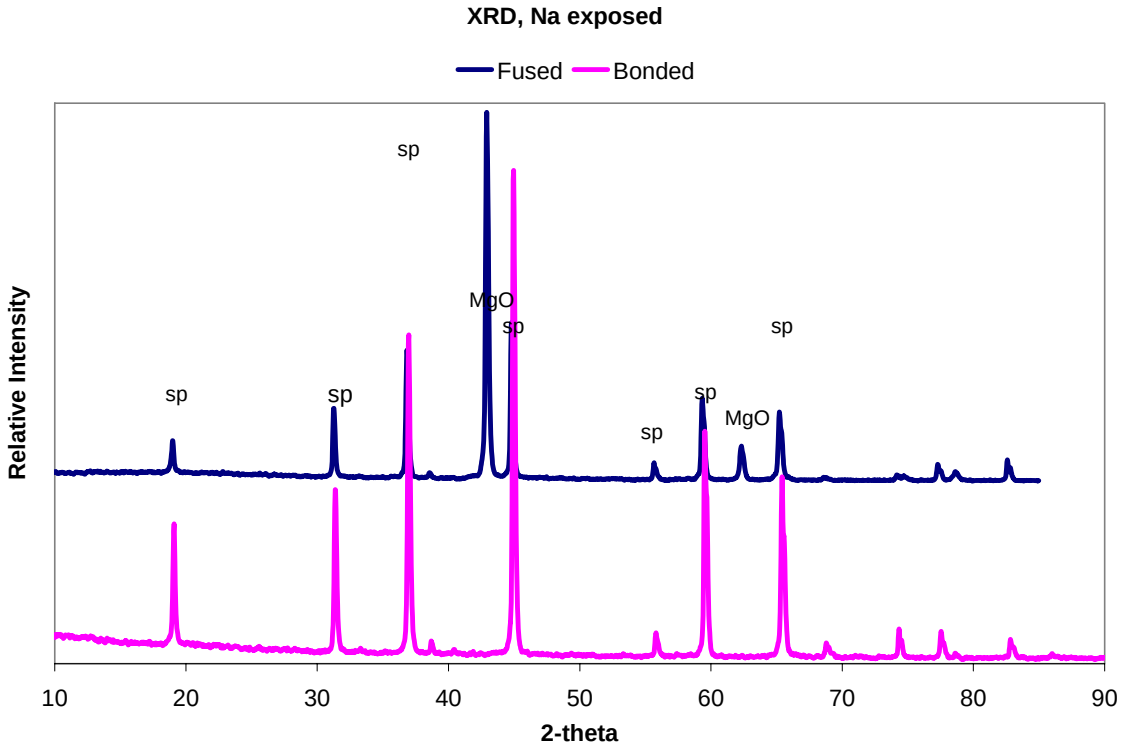

Figure 11 XRD of Bonded and Fused Spinel, after soda exposure in glasstank

Sintered spinel brick is made from high purity, large fused spinel grains. The matrix is porous (approximately 16-18 % apparent porosity as estimated from the microscopy, 14.2% measured) but well sintered. No impurity phase (forsterite, monticellite, merwinite or melilite) were identified/recognized at the magnification scale of the RL/CL microscope used. This does not, however, exclude the presence of small amounts of glassy or ternary phases, which would coat the smaller spinel grains in the matrix. The porous spinel matrix exhibited brighter green (brighter than the CL color of the large fused spinel grains) CL color. Such brightness in CL color may be related to two factors; (1) thermal disturbance and sintering resulting in recrystallization of smaller spinel crystals in the matrix, and (2) simply because of the smaller size of the spinel matrix (intrinsically small crystals exhibit bright CL color at the edges (broken edges) most likely due to mechanically introduced stress/strain concentration. In all three specimens, no unusual features were observed. Microstructures were very similar and found to be typical of spinel materials in all three samples sectioned in various directions.

RL/CL analysis of fused spinel material, however, revealed microstructural irregularities. For example, in specimen STT, two unequivalent microstructures are observed. In the upper portion of the specimen (real direction is not actually known), magnesia has formed large and round isolated grains while it is retained as encapsulated MgO inclusions in the spinel phase. Such microstructural difference could affect the creep behavior of the sample.

In general, the fused spinel block consists of green CL spinel and magnesia. The presence of free magnesia or magnesia inclusions in spinel suggests that the liquid was rich in MgO. The composition of spinel could also be expected to be rich in MgO. All the magnesia beyond the solubility limit of MgO in the spinel structure is rejected as free magnesia. Due to the rapid cooling or crystallization columns of spinel skeletons are formed and the magnesia is segregated as tiny inclusions within these skeletal spinel columns.

Such rapid crystallization appears as linear or locally oriented features in the fused block as observed in three specimens (ST, STT and CT). The orientation of these skeletal spinel columns is, in general, also random. In a single section both transverse or longitudinal microstructures are observed (see microstructures of Sample ST).

Also, in macro-scale, large dendritic patterns and irregular linear features are observed in Specimen ST and Specimen CT, respectively. These features appeared to be microcracks to the unaided eye. They are however, through further investigation identified to be boundaries of rapidly crystallized skeletal spinel columns separated by open spaces.

See RL/CL microstructures of Sample CT, Figure 12. These microstructures are very similar to those observed in Sample ST. Note the feature running diagonally (NE to SW, dark line in RL micrograph or bright line in CL micrograph). Although it appears to be a microcrack, it in fact represents the outline of rapidly growing spinel columns. These lines may act as a week centers during deformation (creep).

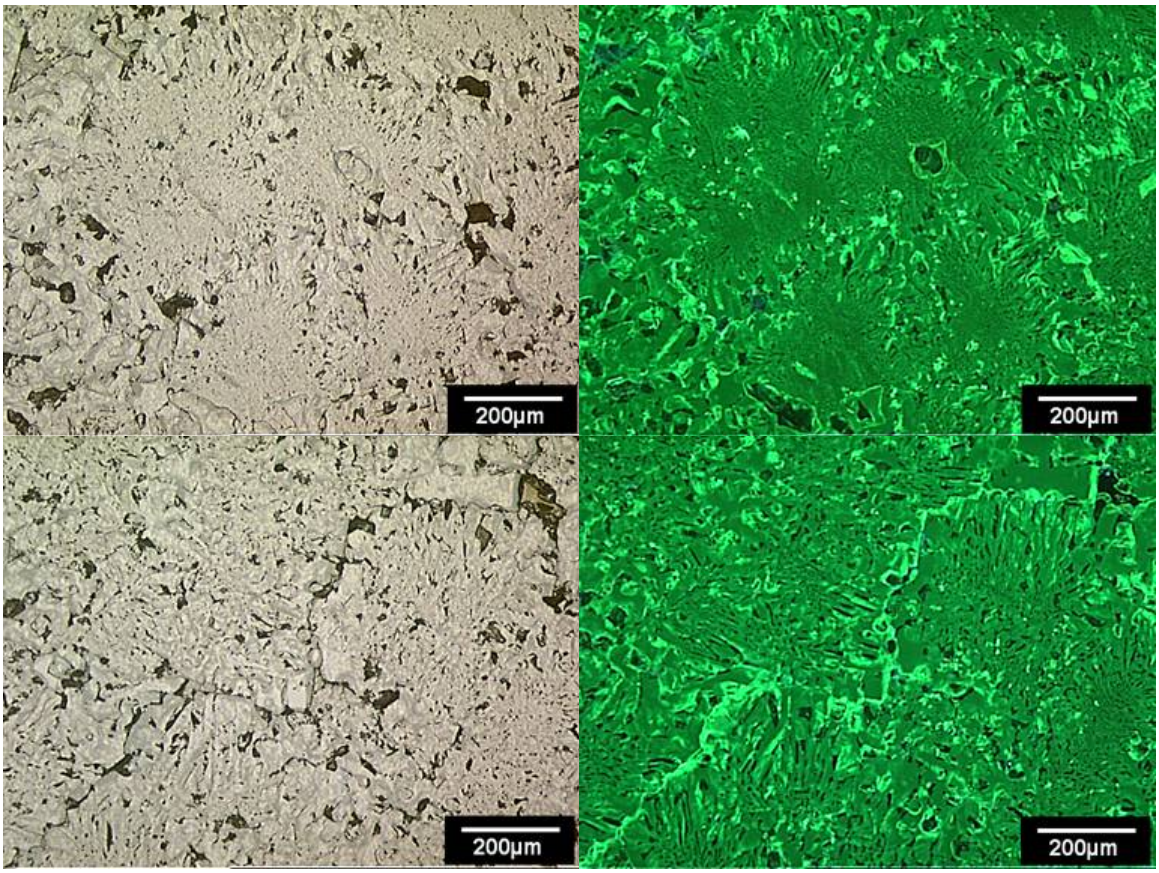

Figure 12 Bulk Fused Spinel Microstructure, Sample CT

Figure 13 shows RL/CL microstructures of Sample ST with diagonal (NW to SE) crystallization features. Although, spinel (green CL) crystals still exhibit random orientation, overall there is a diagonal (in these micrographs) feature developed during crystallization of spinel liquid. These micrographs illustrate the microstructure of rapidly crystallized spinel columns sectioned perpendicularly along the axis of the column.

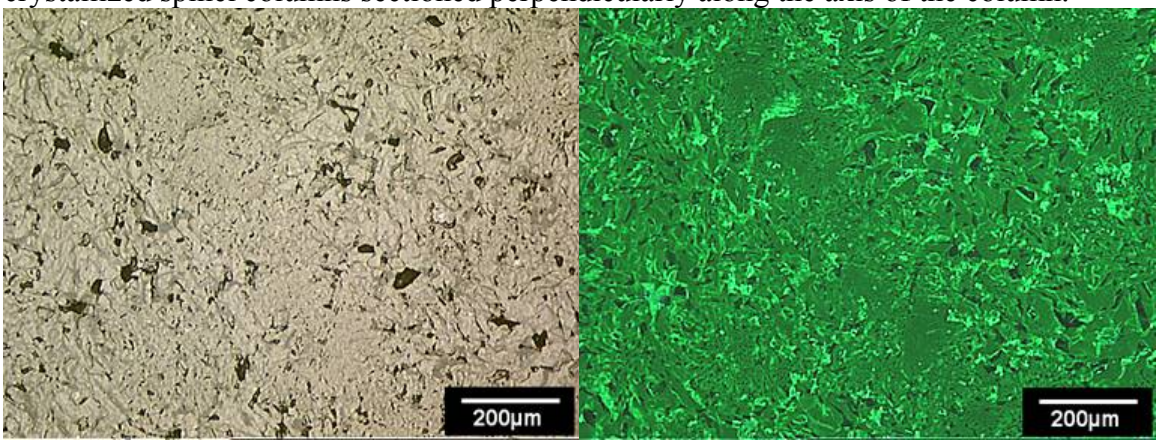

Figure 13 Surface Fused Spinel Microstructure, Sample ST

Figure 14 shows the RL/CL microstructure of Sample ST as transverse sections of spinel columns. Spinel crystals have the tendency to grow outward from the center of column. At the intersections among the columns, open spacing (voids or pores) is observed (dark

or black areas in RL micrograph). Note at the center of a column, due to the rapid growing of spinel, the magnesia component of the liquid is separated as encapsulated MgO inclusions (dark fibrous areas in CL micrograph).

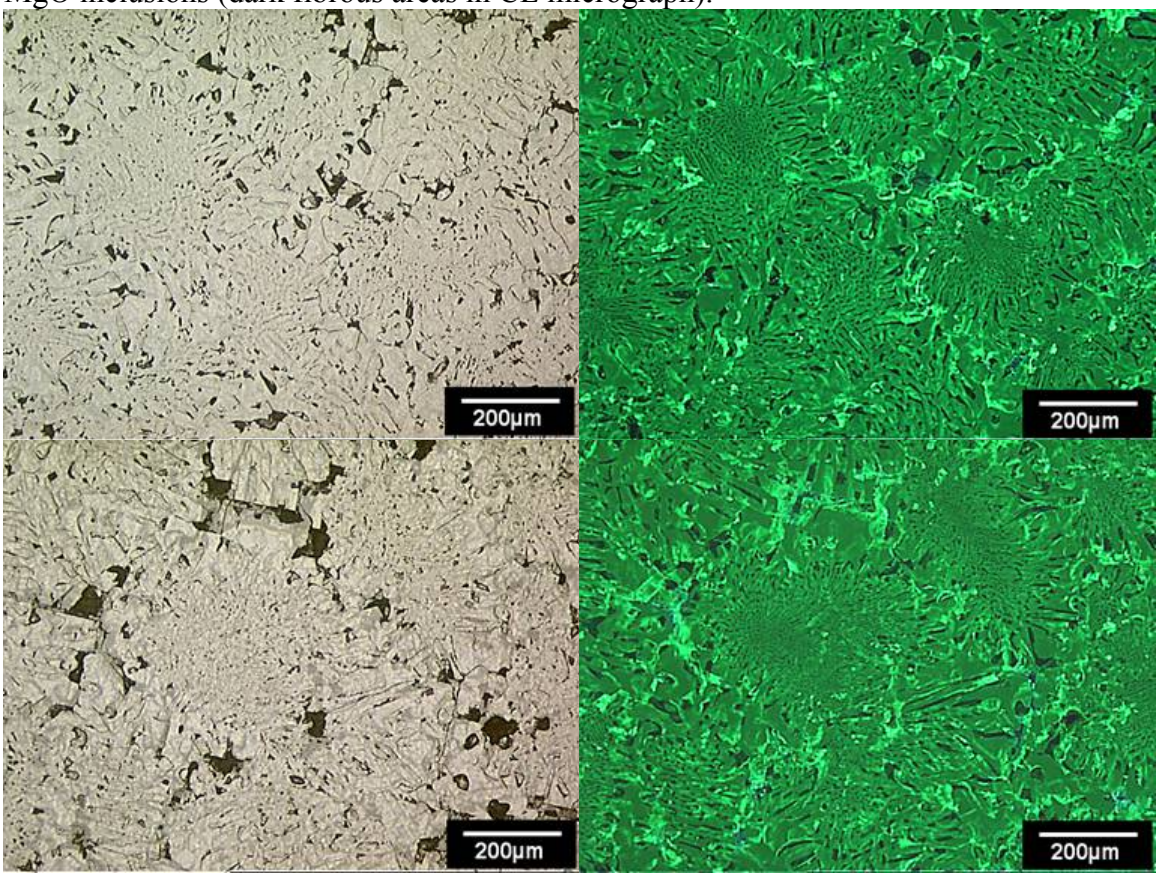

Figure 14 Surface Fused Spinel Microstructure, Sample ST showing spinel columns

Figure 15 shows the RL/CL microstructure of Sample STT taken from upper portion of the section, showing large magnesia (MgO) grains and spinel (green CL). No orientation of crystals is observed in the upper portion of this sample.

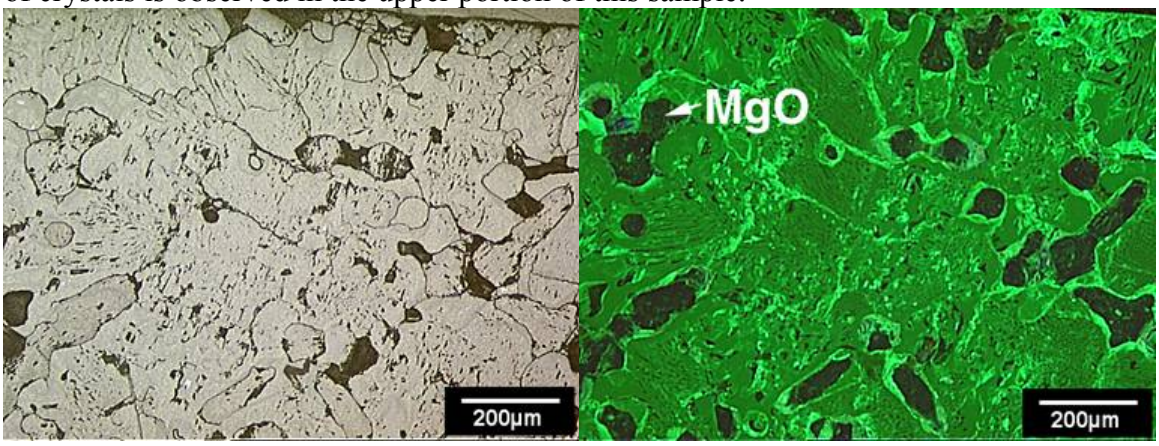

Figure 15 Surface Fused Spinel Microstructure, Sample STT cut perpendicular to the chill zone

Figure 16 shows RL/CL microstructures of Sample STT taken from the lower portion of the section, showing absence of isolated large magnesia grains. Magnesia is however still present as encapsulated inclusions (dark fibrous) within spinel grains.

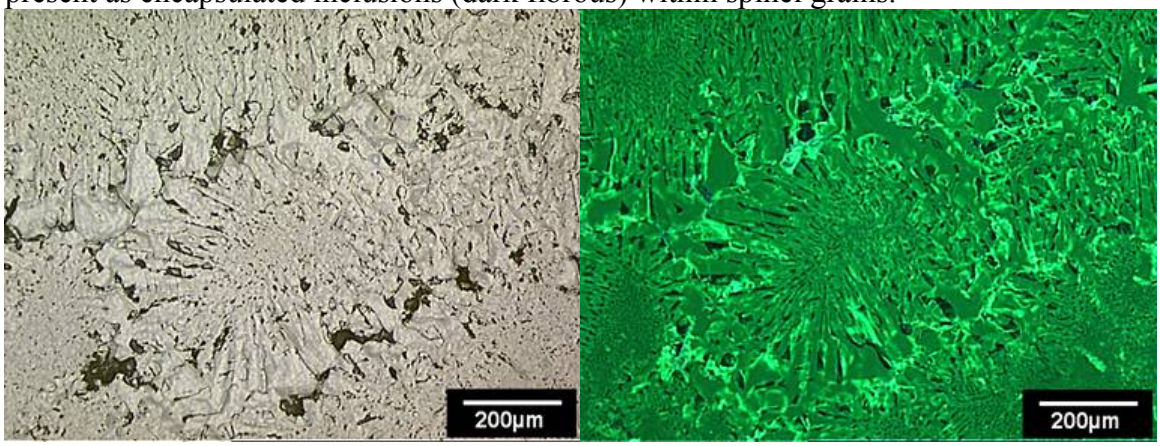

Figure 16 Surface Fused Spinel Microstructure, Sample STT cut perpendicular to the chill zone

Figure 17 shows Low magnification CL micrographs taken from (A, first) upper portion and (B, second) lower portion of the sample STT, show quite different micro textures. The arrows in the second micrographs indicate the triple junction of rapidly solidified spinel grains.

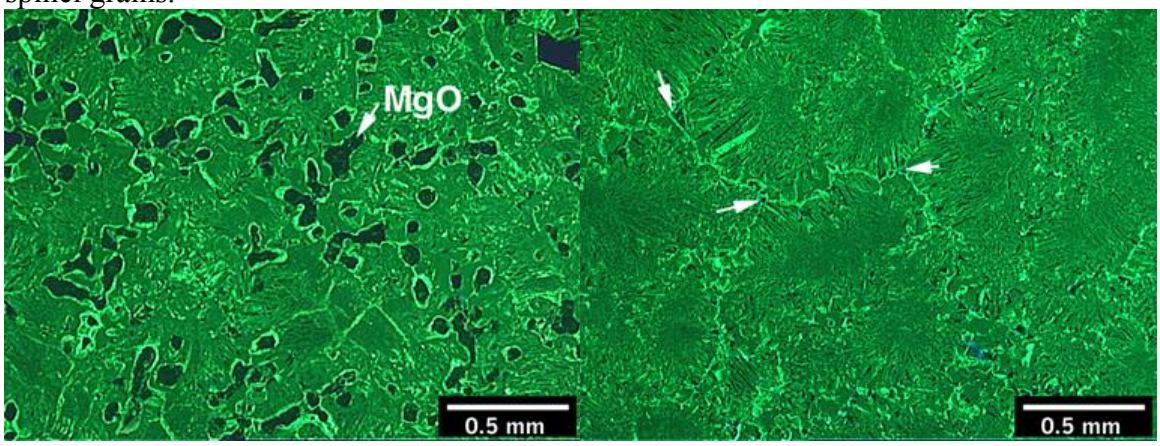

Figure 17 Surface Fused Spinel Microstructure, Sample STT cut perpendicular to the chill zone

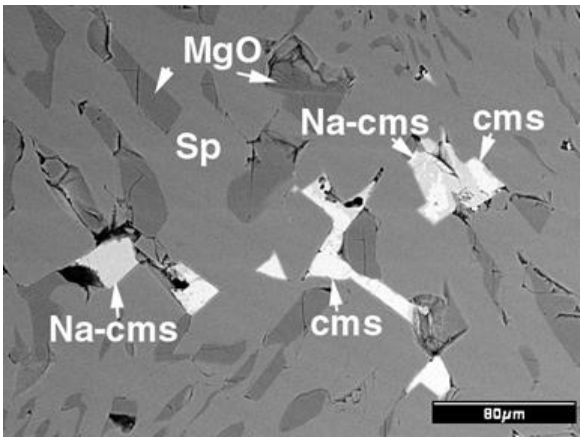

Figure 18 SEM-BSE microstructures of an unused fused spinel sample taken from the chilled zone. Two distinct impurity phases are identified in grain boundaries and junction of MgO and Spinel: (1) a ternary Ca-Mg-silicate (cms) and (2) N

Samples corroded by 200-400 ppm Na for 10 days showed minimal corrosion by the soda. However, silica in the same atmosphere and from the zircon setters reacted with free magnesia to form forsterite as shown in the following series of micrographs. Comparison of CL and SEM-BSE micrographs is shown in Figure 18. The white phase in the SEM micrograph is identified as Ca-Zr-silicate phase (czs) by EDS analysis. Micrographs are taken from the hot face (or the face in contact with NaOH). Figure 19 is a higher magnification SEM image of the same area.

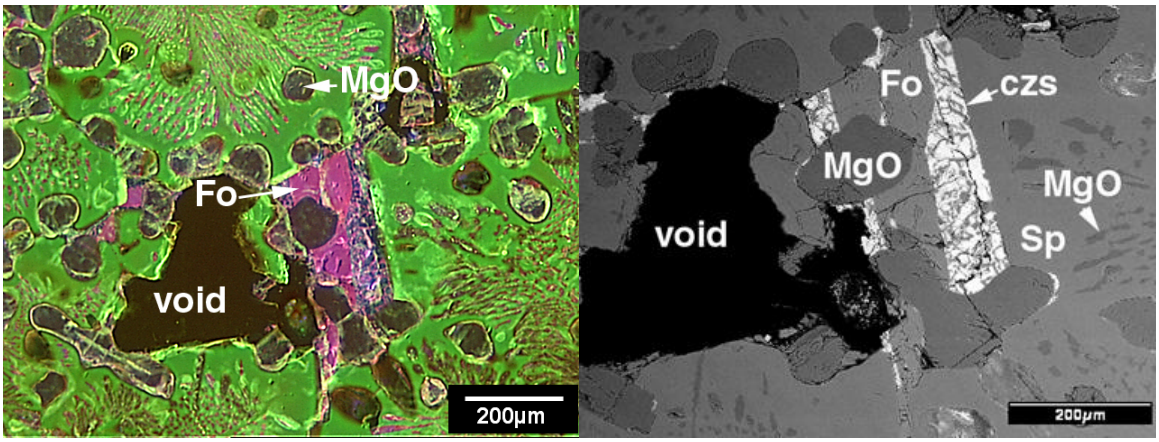

Figure 19 Low magnification CL and SEM micrographs of exposed fused spinel

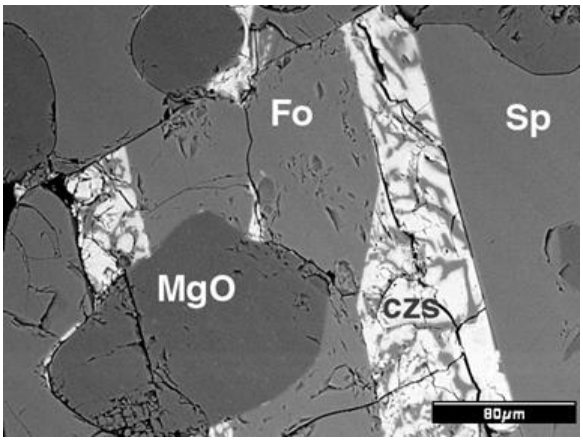

Figure 20 SEM-BSE image of the same field of view as above at higher magnification

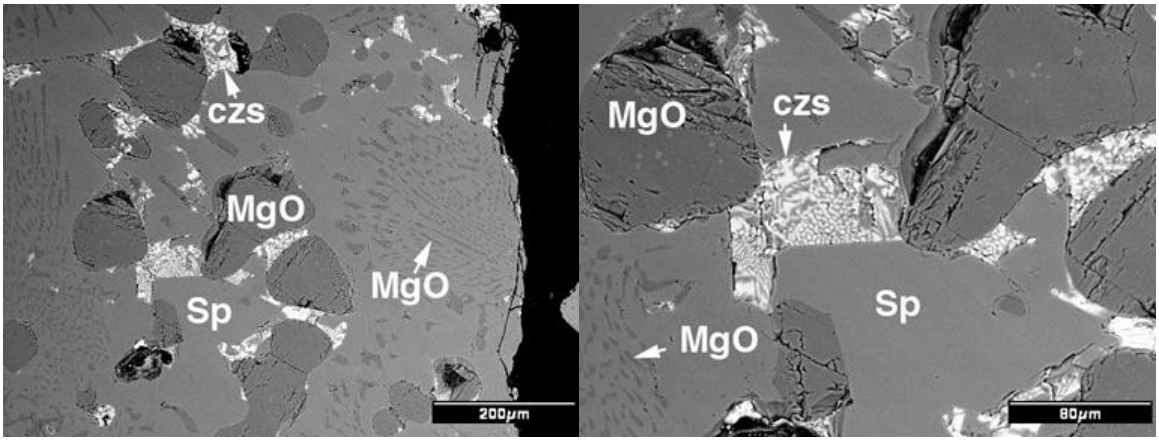

Figure 21 SEM-BSE micrographs taken from the hot face, showing eutectic-like Ca-Zr-silicate phase (czs) in the matrix

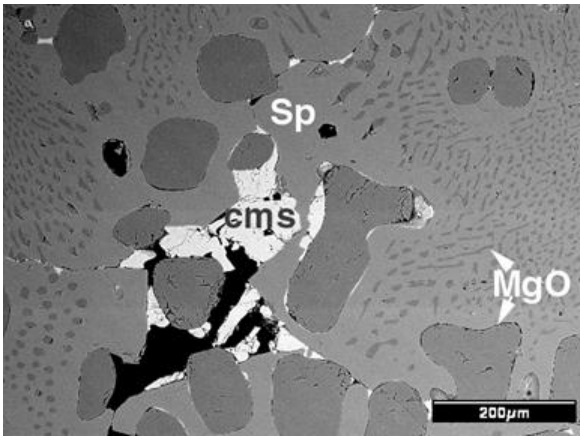

Figure 22 SEM-BSE microstructure of the same sample but taken from the cold side (precisely 1/2" from the hot face). Here, the white phase is a ternary Ca-Mg-silicate phase. No zirconium compound is identified

Bonded samples were made from fused spinel grains (dark green CL large angular grains) bonded with a porous and sintered spinel matrix (brighter green CL). The brighter green CL color may be related to sintering (recrystallization) of smaller spinel particles in the matrix. This fired spinel brick contain no impurity phases. Silicate or glassy phase

content in the matrix is very low and it is not observed at this scale of illustration. No orientation features were observed as shown in Figure 23.

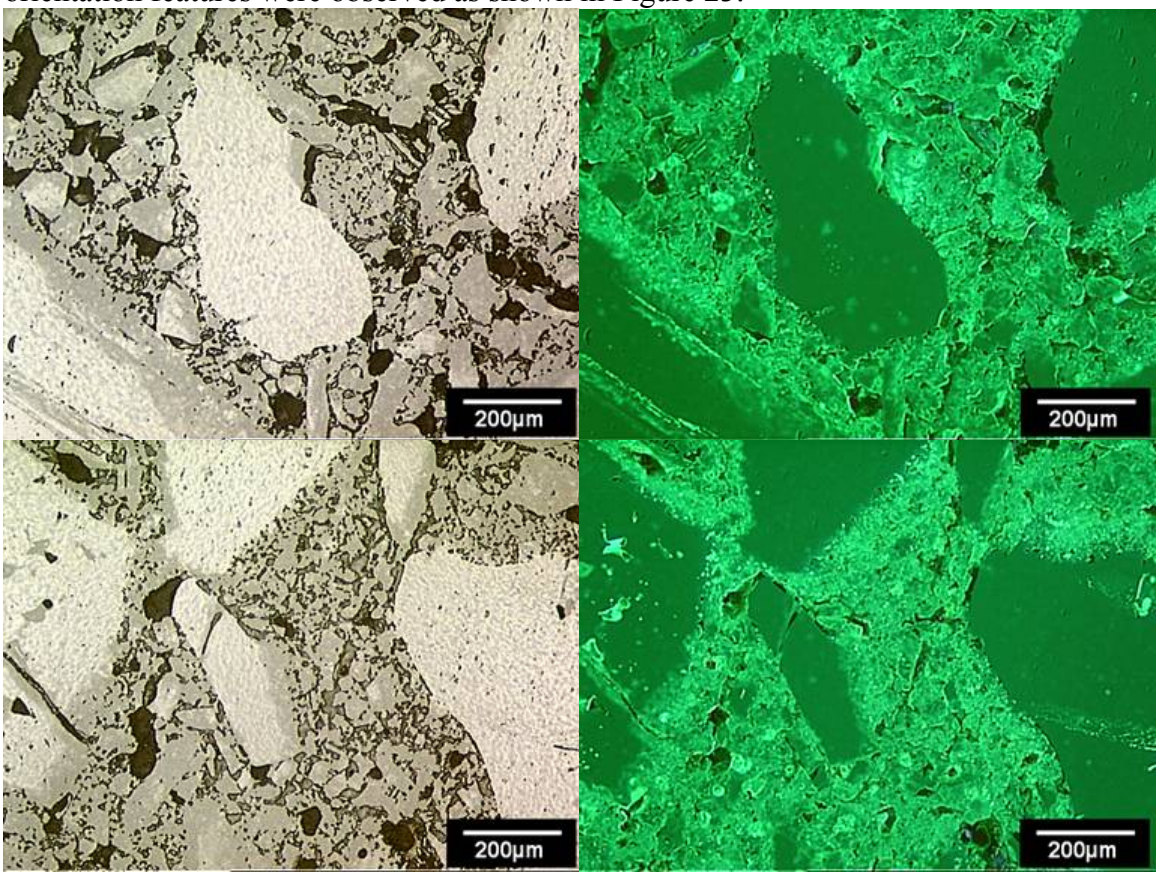

Figure 23 RL/CL microstructures showing large and angular fused spinel fillers (dark green grains) in a porous but well-sintered spinel matrix (brighter green CL). The amounts of porosity and the content as well as composition of glassy phase surroun

Samples corroded by 200-400 ppm Na for 10 days showed minimal corrosion by the soda, Figure 24 and Figure 25. However, small amounts of ternary Ca-Al-silicate (cas) phase is identified in the matrix. The calcia and silica is not identified by XRD nor is it present in the “as received” samples. Therefore it was determined that the calcia and silica must be from the glasstank atmosphere or the zircon setters.

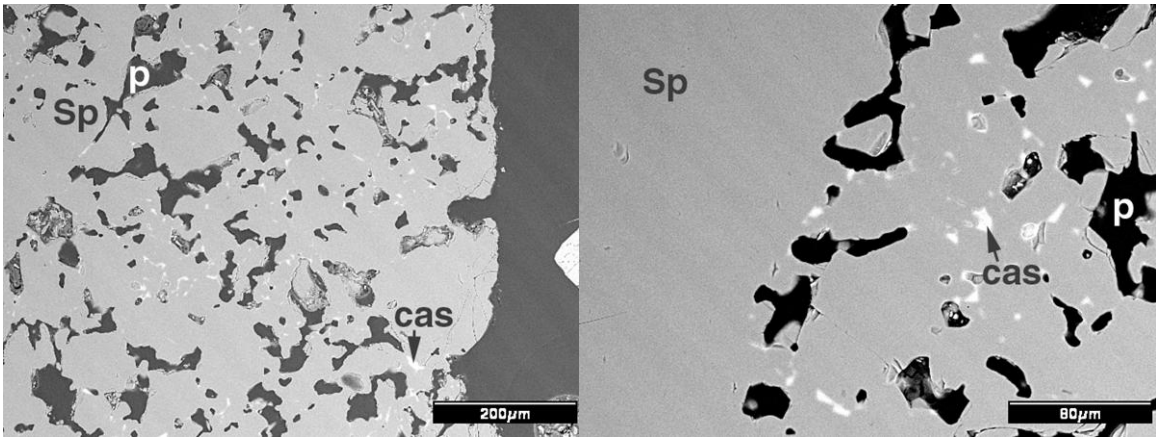

Figure 24 SEM-BSE microstructures, (A) taken from hot face, and (B) taken from 1/2" from the hot face. No Na containing phase is identified. Small amounts of ternary Ca-Al-silicate (cas) phase is identified in the matrix

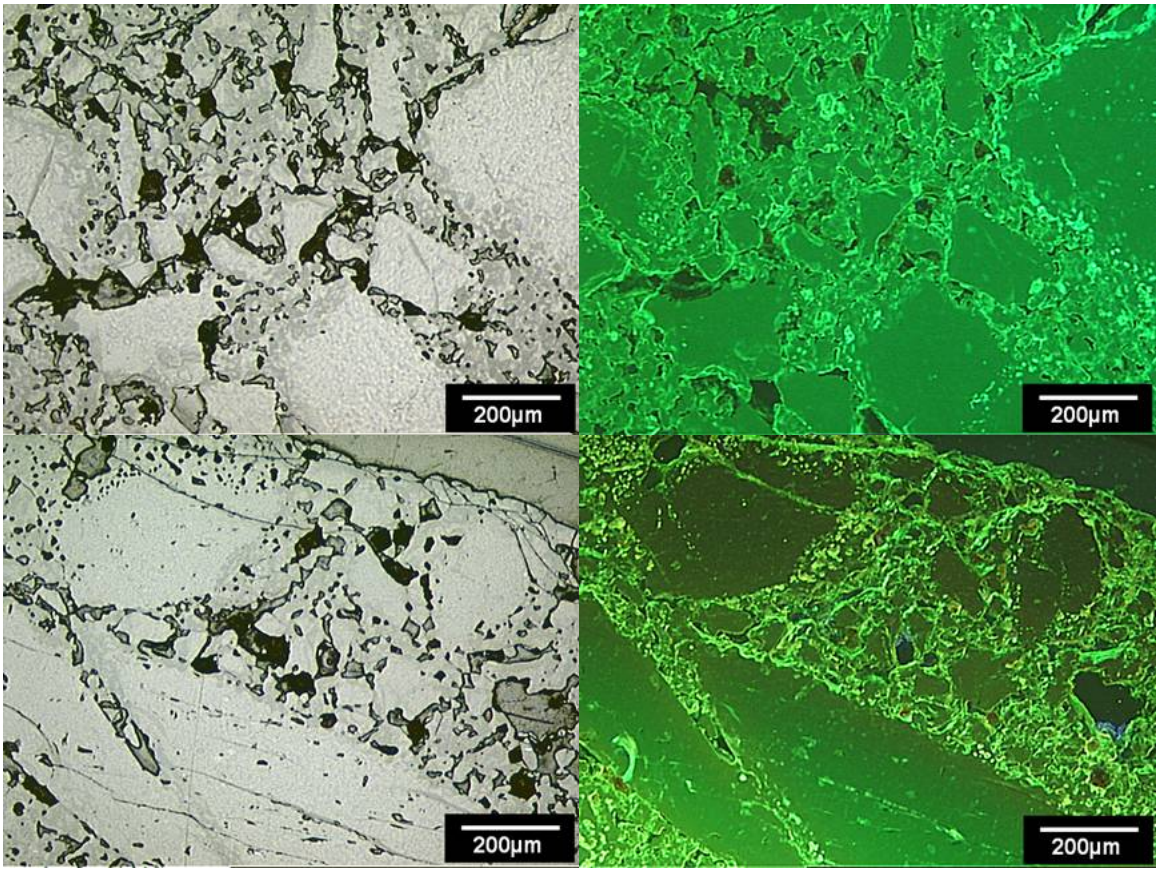

Figure 25 RL and CL images of 11B showing lack of reaction with Na as compared to virgin samples

Task 5: Modeling and Verification

In this task, FEA was used to model the glass tank crown structure. The required boundary conditions for this exercise were based on input from the glass and refractory manufacturers. The model not only accounted for creep effects, but the influence of time-dependent changes in the key thermal properties and corrosion as well. In the case of the

thermal properties, time-dependent changes in thermal expansion and thermal conductivity were used to estimate time-dependent changes in the temperature and stress-state. As a first approximation, the affect of corrosion was to be accounted for by assuming it leads to a uniform loss of the crown structure, however it was determined in Task 4 that there would be no appreciable loss of material. The results of the model are given in the attached thesis, "MODELING OF THEMOMECHANICAL, CRACKING AND CREEP BEHAVIOR IN GLASSTANK CROWN"

Summary

The fused spinel materials had negligible creep rates up to 1650°C at 8.5MPa of stress. The bonded spinel, surprisingly, crept substantially compared to the fused material. However, this must be compared to other common crown materials, the total creep of the bonded material is less than 0.5% over 100 hours at 1550°C and 0.3 MPa which are fairly standard temperature and pressure for testing refractory materials The creep of silica materials is approximately 0.4% over 100 hours at 1450°C and 0.3 MPa[8]. The spinel materials did not react with soda in the exposure tests. There was some limited reaction with silica and calcia from the gasifier atmosphere. Thermal conductivity was determined by laser flash and found to decrease as temperature increases from 14 (100°C) to 8 (700°C) W/mK for the fused spinel and 9.5 (100°C) to 4 (1300°C) for the bonded spinel. A model of the glass tank crown was developed which takes into account non-linear changes in the refractory material due to time, temperature and corrosion. Results are temporarily available at http://web.umr.edu/~bill/projects/creep/. Microstructures have been presented to http://www.udri.udayton.edu/udri_extranet/DLCM/home.asp for inclusion in the Digital Library of Ceramic Microstructures. All results are being submitted to Refractories.Net, http://www.refractories.net/ for database inclusion. Creep rates at lower temperature should be measured in the future on the bonded spinel and competitive bonded spinel. Based on the results in this report both spinel are very promising for the future of energy efficient high temperature glass melting.

[8] A.A. Wereszczak, M. Karakus, K.C. Liu, B.A. Pint, R.E. Moore and T.P. Kirkland, "Compressive Creep Performance and High Temperature Dimensional Stability of Conventional Silica Refractories" ORNL/TM-13757, March 1999.

MODELING OF THEMOMECHANICAL, CRACKING AND CREEP BEHAVIOR IN GLASSTANK CROWN

by

XIAOTING LIANG

A THESIS

Presented to the Faculty of the Graduate School of the

UNIVERSITY OF MISSOURI-ROLLA

In Partial Fulfillment of the Requirements for the Degree

MASTER OF SCIENCE IN ENGINEERING MECHANICS

2003

Approved by

_____	_____
Dr. Lokeswarappa R. Dharani, Advisor	Dr. William L. Headrick, Co-advisor

_____

Dr. K. Chandrashekhara

ABSTRACT

Conventional air-fuel furnaces have been converted to oxy-fuel furnaces rapidly since 1990 in the competitive world of glass manufacturing. This new technology brings many benefits: reduced NO_x, SO_x, and particulate matter emissions; improved energy efficiency and furnace operation; improved glass quality; and increased glass pull rate. However, it also creates problems to the glass furnace refractory life with the increased alkali concentrations on refractory surfaces, especially on the crown refractories. The creep behavior of refractory materials also brings problems to the glasstank crown.

Finite element analysis models for both single glasstank crown refractory brick and glasstank crown were established by using commercial software package ABAQUS 6.3. A nonlinear finite element method was applied to simulate the creep performance of a single brick first; the results from the model were compared to the experimental creep results. Then, a nonlinear finite element method was applied to simulate the response of the glasstank crown to thermo-mechanical loading.

Mullite refractory material was selected for the glasstank crown modeling. The heat transfer, the thermo-mechanical response of the crown, the cracking behavior, and the creep deformation were analyzed.

This thesis was prepared with the support of the U. S. Department of Energy, under Award No. DE-PS07-01ID14123. However, any opinions, findings, conclusions, or recommendations expressed herein are those of the author(s) and do not necessarily reflect the views of the DOE.

ACKNOWLEDGMENTS

I would like to express my sincere gratitude and appreciation to my thesis advisors, Dr. Lokeswarappa R. Dharani and Dr. William L. Headrick, for all the advice, guidance and encouragement they gave me throughout my studies at the University of Missouri-Rolla (UMR). I'm also very thankful to Dr. K. Chandrashekhara for helping me gain an understanding of the fundamentals of finite element method and providing me with valuable comments towards the improvement of my thesis. I would like to express my sincere gratitude to the late Dr. Robert E. Moore, for his suggestions and comment towards the improvement of my research. I would like to express my deep thanks to my colleague, Mr. Jun Wei, for his help, comments and informative discussions towards the improvement of my thesis. I would like to thank Dr. James G. Hemrick for the data and initial model he provided.

Acknowledgement is also due to the U. S. Department of Energy for funding the project.

I would like to thank my family for the love and support they provided. This work would not have been possible without the support of my wife Shuangmei Zhao, and my parents Yuwu Liang and Yuchun Zhou. I would like to give my special thanks to my daughter, Eileen Liang, for the happiness she brought to me during my research work.

Finally, I would also like to thank all my friends at UMR for their support and help during my stay here.

TABLE OF CONTENTS

LIST OF ILLUSTRATIONS

Figure Page

LIST OF TABLES

1. INTRODUCTION

1.1. OVERVIEW

Oxy-fuel glass melting technology in the United States has rapidly grown since 1990 in the competitive world of glass manufacturing. Oxy-fuel firing has dramatically reduced NO_x, SO_x, and particulate matter emissions, is more energy efficient than air firing, provides for increased glass pull rate and regenerator structures are not necessary as in air fuel systems, thus capital effectiveness is improved[1–4].

But there is also a drawback, oxy-fuel firing produces more water vapor which in turn reacts with soda in the glass melt to form sodium hydroxide vapor[5], it causes 1.5 to 6 times higher alkali concentrations on refractory surfaces compared with conventional air-fuel firing methods[6,7], Figure 1.1 shows a schematic of alkali concentration area in glass melting furnace.

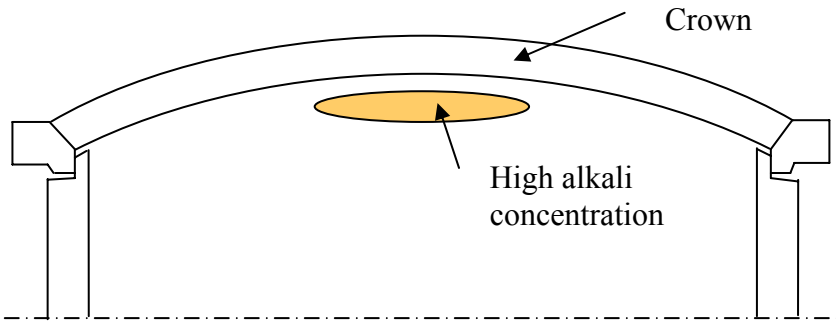

Figure 1.1. The high alkali concentration area in glass melting furnace demonstration

Because of the high alkali concentration, high operating temperature (1400-1650^{o}C) and long-term service (twelve years or up) of the oxy-fuel furnace, the chemical and mechanical stability becomes more and more important for the selection of crown refractories.

Many tests for the corrosion resistance and creep performance of refractory materials have been done recently. Most of these tests are done on single bricks. The thermo-mechanical and creep performance of the whole glass furnace crown during long term operation has not been well understood. An appropriate glass furnace crown model is needed to help furnace designers select crown refractories, optimize the crown geometry and estimate the expected glass furnace lifetime. This will also help furnace operators operate the expensive glass furnace in a more efficient mode in the future.

1.2. LITERATURE REVIEW

To date, various refractories have been installed in the crowns of oxy-fuel fired glass melting furnaces. Among them, conventional silica (SiO_2), fused cast alumina (Al_2O_3), bonded and fused cast mullite ($3AL_2O_3$-$2SiO_2$), and bonded and fused cast spinel (MgO-Al_2O_3) are the materials with highest interest[8]. The literature review in the following sections shows that the corrosion resistance and creep performance of these refractory materials has been studied. Some glass tank crown models with the properties of the above materials have been used for investigating the performance of glass tank crown.

1.2.1 Glass Furnace Crown Refractories. Traditionally, silica is the most widely used refractory material in furnace crown construction in the glass making industry. It has

a high refractoriness under load and high creep resistance, but silica is also the refractory most affected by the high alkali concentration. There have been many reports of increased silica crown corrosion such as hot face corrosion and rat holing, liquid phase rundown and other excessive silica crown wear from glass makers[7,9,10]. Some precautions[11,12] have been taken so that silica can still be used as crown refractory. However, a better solution would be to build crowns with a material which will perform well for the entire operational life of the furnace. There have been many studies of silica and other refractories under oxy-fuel firing condition in order to find an alternative to the silica refractory.

Faber and Verheijen[13] studied corrosion performances of silica and fused mullite refractories from the crown of an oxy-fuel glass furnace. After a 2-year cycle of operation, the observations showed that the silica crown was heavily corroded at lower temperature regions, especially above the batch area, the mullite samples were attacked by NaOH and KOH also, but less than silica. Boillet et al.[14] also conducted corrosion tests for silica and mullite refractories under oxy-fuel firing condition. Gupta and Winder[10] studied the corrosion resistances of silica, mullite and fused cast alumina refractories under oxy-fuel firing conditions. They found that silica refractory was corroded at an accelerated rate under oxy-fuel conditions. Oxy-fuel firing increases the potential for exacerbated rat holing and increased corrosion in silica crowns. Mullite appears to perform a little better than silica in short term corrosion tests, but it is thermodynamically unstable in the presence of NaOH and KOH in oxy-fuel environments. Alumina-based refractories are more thermodynamically stable. Among alumina refractories, fused cast αβ-alumina is considered the preferred material for most

glass melting environments. Pressed and fired refractories exhibit rapid reaction due to their high porosity, dense fused-cast materials show superior corrosion resistance.

Shulver[15] studied the physical properties of silica refractories used for glass furnaces. He found that conventional silica has nonlinear expansion behavior with respect to temperature. The coefficient of expansion shows a moderate change at about 600 ^{o}C.

Wereszczak et al.[16] studied the high temperature compressive creep performance of silica refractory at Oak Ridge National laboratory (ORNL). Six commercial brands of silica materials were selected. Among the six silica products, the compressive creep of five brands was negligible between 1550-1650 ^{o}C (2820-3000 ^{o}F) and compressive stresses between 0.2 to 0.6 MPa (29-57 Psi). The compressive creep rates of all six brands were unable to be represented as a function of temperature and compressive stress using the conventionally used Arrhenius Norton-Bailey creep equation [17] discussed elsewhere in this thesis.

Hemrick et al.[18] studied the thermophysical and creep performance of mullite. Ten different brands of mullite products were tested at 1300-1450 ^{o}C and at static stresses between 0.2-0.6 MPa. All ten brands of mullite have an average thermal conductivity of 3.1 W/mK at room temperature. Seven of the ten brands of mullite have creep rates on the order of 10^{-9}/s to 10^{-11}/s at compressive stresses between 0.2 and 0.6 MPa for higher temperature and lower temperature, respectively. Three brands of mullite have creep rates on the order of 10^{-8}/s to 10^{-9}/s at 0.4 and 0.6 MPa for higher temperature and lower temperature, respectively. The compressive creep rates follow Arrhenius Norton-Bailey creep equation, the activation energies for the various refractories brands ranged from 50 to 223 kcal/mol.

Hemrick[19] also measured the compressive physical and creep behavior of alumina refractories. Several different products from Corhart and Monofrax were selected. Creep measurements were performed at stresses ranging from 0.6-1.0 MPa and temperatures from 1450-1650 ^{o}C. Fusion-cast alumina does not exhibit sufficient deformation or significant chemical changes during creep testing at 1550^{o}C/1.0 MPa. Creep testing at 1650^{o}C/1.0 MPa was sufficient to cause some structural changes for the Monofrax bulk sample, but not for the Corhart bulk sample. Creep rates were unable to be represented as a function of temperature and compressive stress using the conventionally used Arrhenius Norton-Bailey creep equation.

Gupta and Clendenen[20] studied fused alumina crowns from field experience. They concluded that fused alumina crowns are physically and chemically stable in glass melting furnaces, fused αβ-alumina refractory is preferred for crown and superstructure application because of its higher density, strength, and superior resistance to batch dust.

Although the alternative of using αβ-alumina is successful, the adoption is costly. Windle and Bentley[21] pointed out that magnesia-alumina spinel is a viable alternative to fused cast alumina and silica for crown construction. It has lower cost than fused cast alumina and can be bricked in traditional crown construction. They conducted a number of corrosion resistance tests to demonstrate the difference in alkali resistance between spinel and crown quality silica. After the tests, the spinel specimens showed no measurable volume change. In contrast the silica specimens lost 30% of their original volume on average. They also compared thermo-mechanical properties of spinel, silica and αβ-alumina refractories. Spinel and αβ-alumina have lower and linear thermal

expansion which ensures tight joints. All of the three materials have high creep resistance which is suited for crown applications.

Boymanns et al.[22] also studied the chemical and physical properties of spinel bricks for glass furnace crown. He pointed out that the spinel bricks have no slagging reaction in comparison with mullite and other refractories. He also recommends the spinel material as crown refractory for oxy-fuel glass melting furnace.

Table 1.1[15,21,23,24] gives the cost and properties of silica, mullite, spinel and αβ-alumina refractories. Among them, spinel and αβ-alumina refractories have the greatest corrosion resistance against alkaline attack and excellent thermo-mechanical behavior. They are good candidate refractory materials for crowns in oxy-fuel firing glass melting furnaces. The spinel material would be a better candidate because of its lower cost.

Table 1.1. Cost and properties comparison of the considered refractories

Property	Glass tank refractories materials			
	Silica	Mullite	Spinel	αβ-alumina
Cost per m^3 (compared to silica)	1	5	7	10
Density (g/cm^3)	1.79	2.7	3.0	3.4
Corrosion resistance	Poor	Medium	Excellent	Excellent
Thermal conductivity (W/mK @ 1200°C)	2.0-2.3	3.1	3	5.2
Thermal expansion	nonlinear	linear	linear	linear

1.2.2. Glass Furnace Crown Modeling. To date, Finite Element Analysis has been used to model the thermo-mechanical performance of glass furnace refractories and it is discussed below. Some work has been done concentrated on the side wall refractories[25,26]. The limitation of these analyses is that they are restricted to only elastic analysis and do not consider time dependent creep behavior in the life of the arch. Also, in the above work, some fairly restrictive assumptions were made. They are: stress-strain relations are purely elastic; steady-state thermal conditions exist and transient heating and cooling can be neglected; thermal conductivity, thermal expansion and elastic modulus are uniform throughout the geometry.

Very little work has been done on the modeling of glass furnace crown refractoreis. Hemrick[19] established a model for fusion-cast alumina refractory crown by finite element analysis using the commercial software package ANSYS 5.4**.** A full crown was first modeled and a temperature gradient was applied across the thickness of the crown to simulate furnace heat-up. A thermal model was first run to generate the temperature fields within the arch and then a stress model was generated based on these temperature fields and the resulting expansion occurring in the arch. Then a half section of the crown was modeled and the creep and stress relaxation was considered. The model produced results that were not completely accurate, especially, the deformation analysis. Also, only a linear case was analyzed since this is the strength of the ANSYS code.

Koyuncu and Carlson[27] analyzed the glasstank crown thermal stress analysis during heat up by finite element modeling. They built a crown model which is made up of individual blocks capable of sliding on each other. αβ-alumina refractories were considered for the model. Stress distribution in the crown during heat up, displacement

and the effect of block geometry were studied. Koyuncu and Carlson[27] concluded that the crown displaces down slightly as the block expand; the thicker blocks will result in higher maximum stresses throughout the heating period and higher stresses concentration at block-to-block interfaces. This model helps to understand the development and magnitude of thermal stresses experienced by the glass furnace crown refractories. But it is not completely accurate and sufficient to investigate the thermo-mechanical and creeping performance of glass furnace crown over its long term operation, since glass furnace crowns are made up of refractory bricks which may separate partly from each other during heat up. This will affect the stress distribution and deformation of the crown. Also, the creep performance is a very important consideration in the operation of a glass furnace.

From the foregoing discussion, it is clear that there is an urgent need to develop a rigorous and mechanics based non-linear finite element crown model for the selection of crown refractories, the optimization of crown geometry and the estimation of the expected operational life.

1.3. OBJECTIVE

To date, several compressive creep tests for single glass tank refractory brick have been done. The compressive creep performance for single bricks exposed to high temperature environment has been studied. However, the whole glass tank crowns are exposed in high alkali concentration and high temperature environment. The operational environment of the glass tank crown is significantly different from that of the single brick experiment. It is hard to understand the thermo-mechanical and creep performance of a

whole glass tank crown by the experimental creep data. There is a great need of a glass tank crown model to simulate the operational environment of glass tank crown. Thereby provide detailed insight to help furnace designers select crown refractories, optimize the crown geometry and estimate the expected glass furnace lifetime. And also help furnace operators operate the expensive glass furnace in a more efficient mode in the future.

The model will be used to simulate the performance of the glass tank crown with both commonly used refractory materials, such as silica, mullite and alumina and new refractory materials such as spinel. The simulation will consist of heat transfer analysis, thermo-mechanical analysis, crack propagation and creep analysis.

Mullite refractory material will be selected for the initial glasstank crown modeling. The heat transfer, the thermo-mechanical performance of the crown and the creep deformation of the crown will be analyzed.

This problem is solved using the commercial finite element package ABAQUS[28].

2. GLASS FURNACE CROWN

The glass furnace crown is a part of the glass furnace. It is made of refractory bricks in one or several layers and is exposed to a high alkali concentration and high temperature environment during its long term service. The service life of furnace crown may be up to 12 years or longer. The length of the crown varies from less than one meter to more than thirty meters.

2.1. BASIC GLASS FURNACE CONSTRUCTION

Glass melting furnace usually consists of melter for melting raw materials, refiner for refining and homogenizing and controlling the temperature of the molten glass, upper structure for keeping combustion space and other parts[23,29]. A schematic of a typical oxy-fuel furnace is shown in Figure 2.1[19].

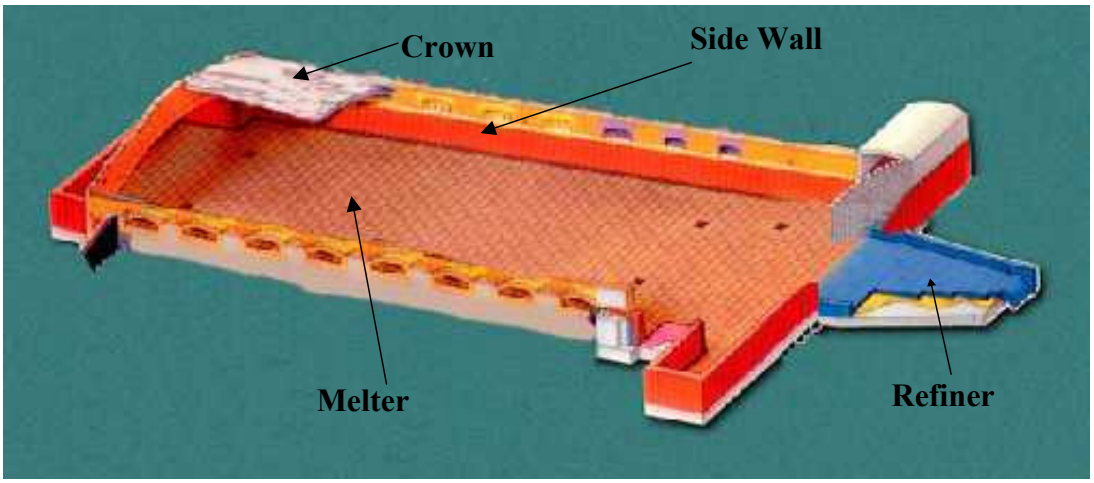

Figure 2.1. Typical oxy-fuel glass furnace construction

2.2. GLASS FURNACE CROWN

The crown belongs to the upper structure of glass furnace. It employs the arch construction.

2.2.1. Arch Theory. The primary loads imposed on the refractory brick arch are the thermal expansion loading and the gravity load. The stresses caused by the gravity load are quite small compared to the thermal expansion stresses in the constrained arch. An arch design that has worked successfully in industry is the sprung arch design[30], which is show in Figure 2.2.

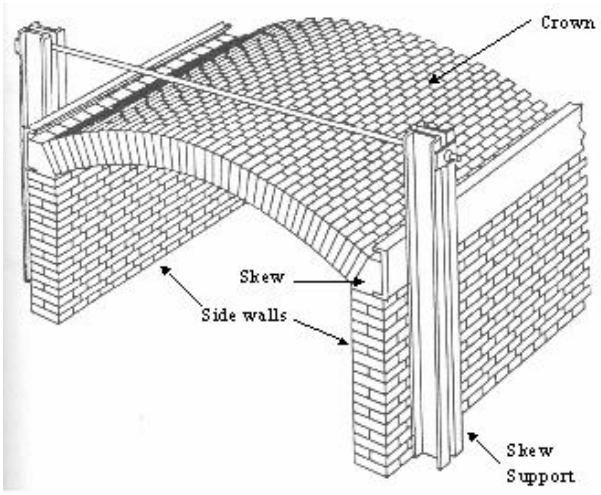

Figure 2.2. The refractory brick sprung arch construction

Figure 2.3 shows the support details of the basic refractory arch construction[30]. In such design, the crown typically terminates at a skew on each end, and is supported by continuous horizontal steel beam along the exterior end of each skew. The skew transmits

the vertical force to the supporting wall and transmits the horizontal force to the external steel beam. The steel beam is connected to vertical columns which are spaced at uniform intervals. The base of each vertical column is designed as a pin connection, allowing the column to rotate from the base without resistance. The top ends of each column pair are connected by a spring and bolt system. The spring stiffness is chosen to resist the crown horizontal thrust due to gravity load. The bolts are loosened periodically during the initial heat up to allow for the appropriate horizontal outward movement of arch

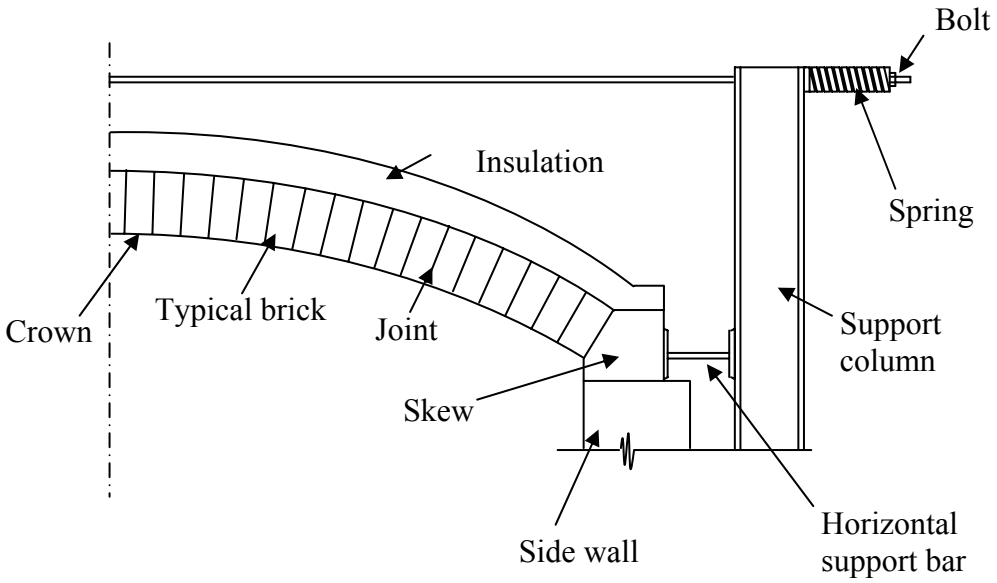

Figure 2.3. The support details of sprung arch

2.2.2. High Temperature Behavior of Arch. The refractory arch is typically exposed to a temperature environment which makes the arch have a hot face with higher temperature in the inside of arch and a cold face with lower temperature in the out side of

arch. Because of the temperature gradients through the thickness of the glass tank crown, an expansion difference will be produced through the crown thickness.

Because of the thermal expansion, the arch geometry will change. The new expanded crown does not fit the installed skew position due to two primary changes: the expanded size due to the average increase in temperature and the rotation due to the through thickness temperature differences. These changes cause the arch to transform from having all of its joints in contact to a three-hinged arch configuration.

Expansion allowance is controlled to accommodate the expanded arch geometry. The skew can be displaced horizontally to allow the increase in the arch span. However, the skew will not rotate to fit the change of the angle of the crown totally, so a slight excess in expansion allowance usually creates a more stable heated arch. Figure 2.4 shows the three-hinge configuration with excessive expansion allowance[30].

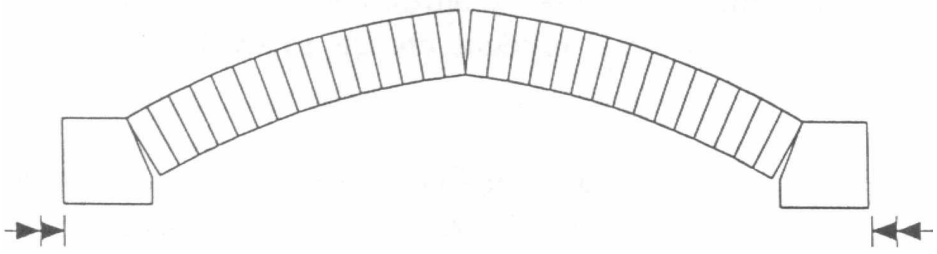

Figure 2.4. Three-hinge configuration with excessive expansion allowance

Figure 2.5 gives the geometry definition of arch[30] in which t is the thickness of arch, v is the height of the skew, θ is the central angle of the arch. McDowell provides a

limit to the arch thickness t as a function of the rise h, span S and the central angel θ.

$$t < \left\{ \; h - \left[1/(48S)\right] \; \right\} / \cos(\theta/2) \tag{1}$$

The limitation of the arch thickness is to minimize the adverse condition. As the thickness increases, the vertical distance between hinges becomes quite small. When this condition occurs, the thrust becomes very large. The refractory would experience either excessive plastic flow or brittle fracture at the hinges, leading to instability.

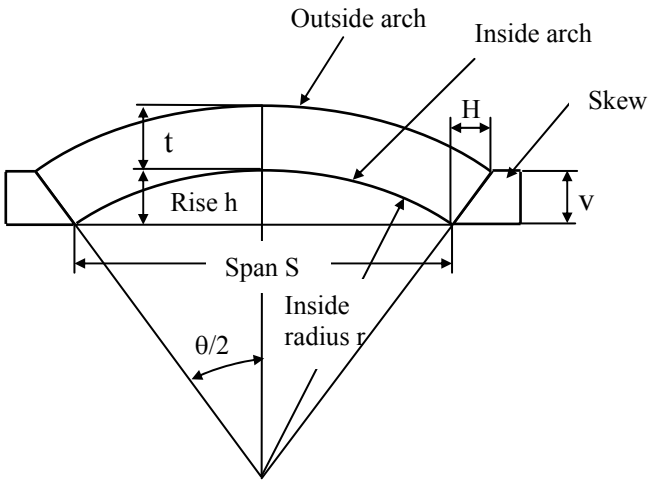

Figure 2.5. Definition of arch geometry

Expansion allowance is determined by the horizontal thermal expansion of the arch. The thermal expansion can be solved approximately by using the average temperature, $T_{avg.}$ given by

$$T_{avg.} = \left(T_h + T_c\right)/2 \tag{2}$$

where T_h is the hot face temperature and T_c is the cold face temperature.

The horizontal thermal expansion at the inside of the arch consists of two portions, as shown in Figure 2.6, one is the thermal growth of the arch span, and the other portion is the part which occurs due to the through-thickness temperature gradient.

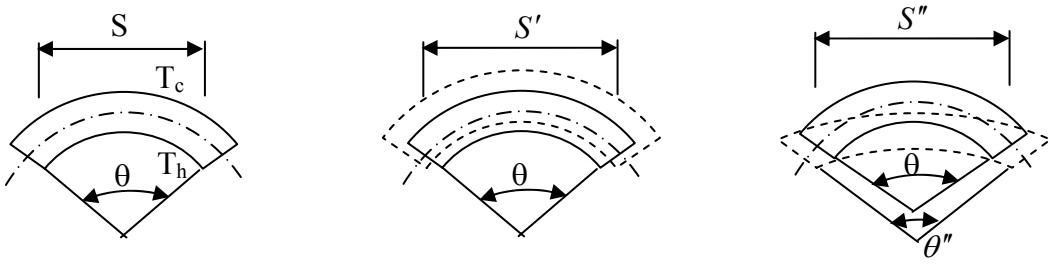

a. cold arch b. span expansion c. arch rotation

Figure 2.6. Typical arch thermal expansion illustration

With refrence to Figure 2.6, the total horizontal thermal expansion is expressed as

$$dS = dS' + dS'' \tag{3}$$

where dS' is the thermal growth of the arch span and dS'' is the part which occurs due to the through-thickness temperature gradient.

The thermal growth of the arch span dS' is given by

$$dS' = \alpha\left(T_{avg.} - T_r\right)\ S \tag{4}$$

where α is the thermal expansion coefficient of the arch refractory material, and T_r is the installed or room temperature, S is the span of the arch.

The second part, dS'' is caused by the rotation of the arch. Because of the through-thickness temperature gradient, the expansion in the crown inner face is larger

than that in the crown outer face. This causes the central angle to increase from the original installed angle of θ to a smaller angle θ''. The change in the central angle is defined as:

$$\beta = \theta'' - \theta \tag{5}$$

The angle β can also be defined in terms of the temperature difference, dT through the arch.

$$dT = T_H - T_c \tag{6}$$

The thermal growth for unit length is

$$dL = dT\alpha \tag{7}$$

The unit angle of rotation is

$$d\beta = \tan^{-1}\left(2dT\alpha/t\right) \tag{8}$$

The total angular change β is

$$\beta = Ld\beta \tag{9}$$

where L is the arch length along the arch centerline

$$L = \left[2\pi\left(r + t/2\right)\right]\ \theta/360 \tag{10}$$

Therefore

$$\beta = \tan^{-1}\left(2dT\alpha/t\right)\left[2\pi\left(r + t/2\right)\right]\ \theta/360 \tag{11}$$

The revised arch radius is taken as the inverse of the central angle change

$$r'' = \left(\theta/\theta''\right)\ r \tag{12}$$

The revised span

$$S'' = 2r''\sin\theta'' \tag{13}$$

Based on the through thickness temperature difference, the addition span length due to rotation is:

$$dS'' = S'' - S \tag{14}$$

here θ is the central angle of the arch, r is the inside radius, dT is the temperature difference, α is the coefficient of thermal expansion, t is the thickness of the arch.

The primary load-carrying crown components are crown bricks. The brick joints may be either mortar joints or dry (unmortared) joints. The joints can not resist significant tensile load. They will separate under tensile stress. Due to the through thickness temperature gradients, the cold face side will develop tensile stress, so the brick-to-brick joints will open from the cold face. This phenomenon is illustrated by Figure 2.7. Theoretically, the hot face side of the crown experiences the compressive stress, and the open joint part has no stress.

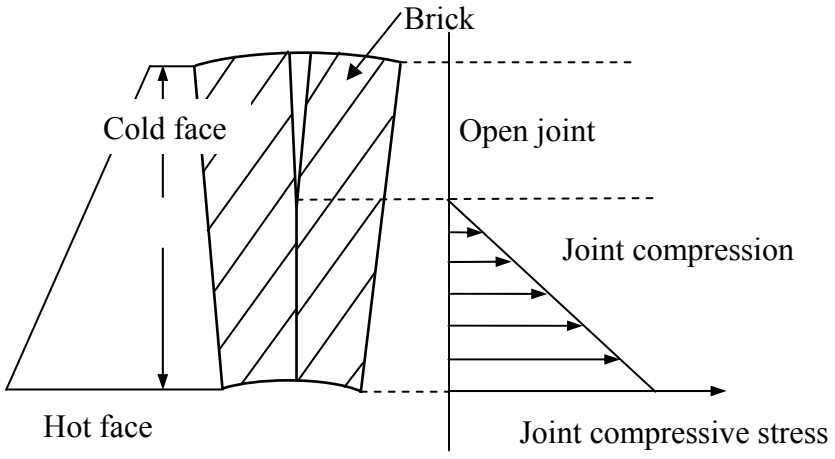

Figure 2.7. Arch bricks joint opening illustration

3. BASIC CONCEPTS

The crown is exposed to a high temperature environment. The crown refractories experience a combination of gravity and thermal loads during service. These two loads are classified as external stress-controlled load which is from the structural gravity load and internal strain-controlled load which is the thermal load. The primary stresses in the crown are developed due to the temperature gradients and restraint of adjacent elements of the body by the supporting structure. In the constrained arch, the stresses developed by the gravity load are quite small compared to those developed by the thermal loads. The crown is made up of bricks. The bricks are bonded tightly before heat up, but they may separate from each other during heat up. This mechanism of opening of the brick-to brick joints is similar to crack propagation. Usually, the creep phenomenon plays a predominant role in the failure of refractories exposed to high temperature environment.

The basic concepts of heat transfer, thermo-mechanics, fracture mechanics and creep needed for solving this problem are presented next.

3.1. HEAT TRANSFER CONCEPTS

The heat conduction process is assumed to obey Fourier's law[31] given by

$$q_i = -kT_{,i} \qquad (i = 1,2,3) \tag{15}$$

where $k > 0$ is the thermal conductivity of the material; q_i is the vector of the heat flux, and $T_{,i}$ is the temperature gradient.

Each component q_i denotes the amount of heat flowing in the direction x_i. Thus, through the elemental areas $ABCD$ and $A'B'C'D'$ (Figure 3.1), the rates of heat flow are given by, respectively

$$-kT_{,1}\,dx_2dx_3 \tag{16}$$

and

$$-\left[kT_{,1}+\left(kT_{,1}\right)_{,1}dx_1\right]\,dx_2dx_3 \tag{17}$$

the net rate of heat flow in the x_1 direction through the elemental volume $ABCDA'B'C'D'$ is given by

$$\left(kT_{,1}\right)_{,1}dV \tag{18}$$

where dV is equal to $dx_1dx_2dx_3$. Changing subscripts of the equation, the net rate of heat flow in other directions can be obtained.

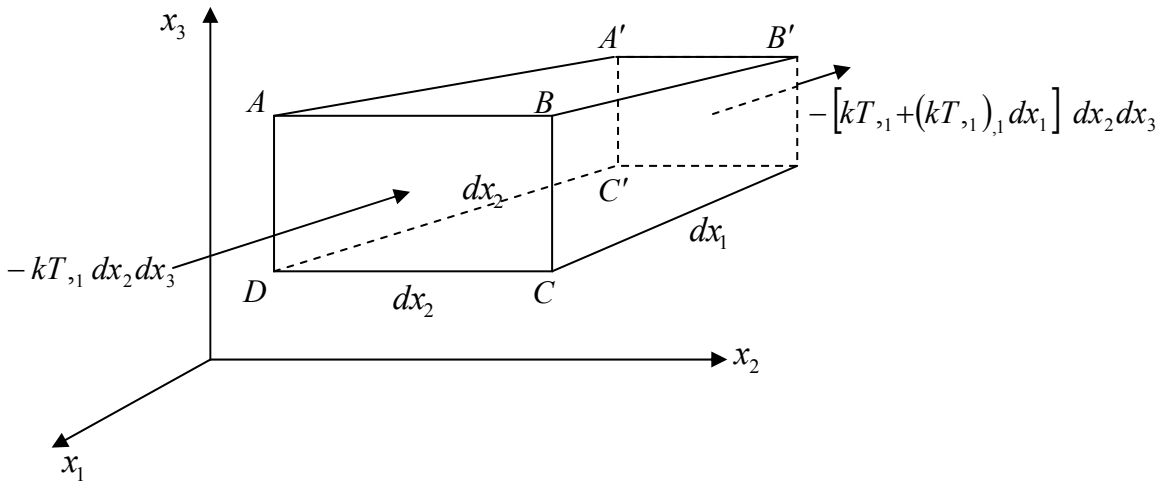

Figure 3.1. Heat flow rate through the element

Assuming in the body the existence of heat sources which generate heat at the rate Q per unit time and unit volume, and knowing that the total rate of change of internal

energy is $\rho c\dot{T}$ where ρ is the density and c is the specific heat, the balance of energy is:

$$\left(kT_{,1}\right)_{,1} + \left(kT_{,2}\right)_{,2} + \left(kT_{,3}\right)_{,3} + Q = \rho c\dot{T} \tag{19}$$

Assuming that the thermal conductivity k is the same at all points of the body, the heat conduction equation is obtained as

$$T_{,ii} + Q/k = \dot{T}/\kappa \tag{20}$$

where $\kappa = k/\rho\ c$ is the thermal diffusivity, in which higher density and higher heat capacity increase thermal energy storage, and reduce the temperature diffusivity[32]. The repeated index ii means summation over values 1, 2, and 3, thus:

$$T_{,ii} = \nabla^2 T \tag{21}$$

If there are no heat sources within the body ($Q = 0$) and the temperature does not depend on time ($\dot{T} = 0$) the heat conduction equation reduces to the Laplace equation:

$$T_{,ii} = 0 \tag{22}$$

The heat conduction equation is solved with appropriate initial and boundary conditions. The initial conditions specify the temperature field at a prescribed moment of time. The boundary conditions belong usually to the following five types:

1. Given surface temperature of body:

$$T(P,t) = f(P,t) \tag{23}$$

where P is a point on the surface, t is the time, and $f(P,t)$ is a prescribed function.

2. Given heat flux:

$$q_n(P,t) = -kT_{,n} = g(P,t) \tag{24}$$

where n indicates a normal to the surface, and $g(P,t)$ is a prescribed function.

If the body is exposed to the radiation of an external heat source of temperature T_1, then this condition follows the Stefan-Boltzmann law:

$$kT_{,n} = C\left(T_1^4 - T^4\right) \tag{25}$$

where C is a constant coefficient

3. Insulated surface is a special case of type (b):

$$T_{,n} = 0 \tag{26}$$

4. Convection boundary condition:

$$kT_{,n} = h\left[T_1 - T(P,t)\right] \tag{27}$$

where h and T_1 denote the boundary conductance and the temperature of the ambient, respectively.

5. The contact of two bodies:

$$T_1(P,t) = T_2(P,t) \tag{28}$$

$$k_1 T_{1,n} = k_2 T_{2,n} \quad \text{(at P and t)} \tag{29}$$

where P is a point of the surface of contact, n is a common normal to the surface of contact and subscripts 1 and 2 refer to the first and second body, respectively.

3.2. THERMO-MECHANICAL CONCEPTS

The general equations of thermal stresses and thermoelasticity are based on the law of motion, the principle of conservation of mass, and the principle of conservation of energy. For the case of small deformation and of small and slow changes of the temperature, the theory of thermal stresses simplifies considerably[31].

In the classical theory of thermal stresses, the solutions are obtained in two steps. First, the temperature $T(P,t)$ is established, the temperature is assumed to be independent of deformations. Second, the temperature $T(P,t)$ is used in finding the displacements, strains, and stresses in the body.

The strain-displacement relations are based on purely geometrical consideration and do not change whether thermal effects are on. They are given by

$$2\varepsilon_{ij} = u_{i,j} + u_{j,i} \tag{30}$$

The six compatibility equations are given by

$$\varepsilon_{ij,kl} + \varepsilon_{kl,ij} = \varepsilon_{ik,jl} + \varepsilon_{jl,ik} \tag{31}$$

The principle of conservation of linear momentum may be written in the differential form

$$\sigma_{ij,j} + f_i = \rho\dot{v}_i \tag{32}$$

where f_i is the body force, and $\dot{v}_i$ is the acceleration. For the static case, the equations of equilibrium are

$$\sigma_{ij,j} + f_i = 0 \tag{33}$$

The stress tensors are symmetric

$$\sigma_{ij} = \sigma_{ji} \tag{34}$$

Mechanical boundary conditions are usual given by displacement or surface traction of the following types:

1. Given surface displacements u_i

$$u_i = F_i(P) \tag{35}$$

2. Given surface traction S_i

$$S_i = \sigma_{ji} n_j \tag{36}$$

where, n_j indicate direction cosines of the unit surface normal n.

The above equations of the theory of isothermal elasticity do not contain the temperature. However, the changes in temperature must be included in the expression for the internal energy of the body.

Assume the elastic strain energy U per unit volume of the form

$$U = \frac{1}{2} a_{ijkl} \varepsilon ij \varepsilon kl + b_{ij} \varepsilon_{ij} \tag{37}$$

where, a_{ijkl} is the tensor of elastic moduli and b_{ij} is a linear function of the temperature rise T.

$$b_{ij} = -\gamma_{ij} T \tag{38}$$

where γ_{ij} is a tensor of coefficients.

In the case of an isotropic body,

$$U = \mu \varepsilon_{ij} \varepsilon_{kl} + \frac{1}{2} \lambda \varepsilon_{kk}^2 - m \varepsilon_{kk} T \tag{39}$$

where $\varepsilon_{kk} = \varepsilon_{11} + \varepsilon_{22} + \varepsilon_{33}$ and $\varepsilon_{kk}^2 = \varepsilon_{11}^2 + \varepsilon_{22}^2 + \varepsilon_{33}^2$, λ and μ are Lame constants and

$$m = (3\lambda + 2\mu)\ \alpha \tag{40}$$

α is the coefficient of linear thermal expansion.

Using relations

$$\sigma_{ij} = \partial U / \partial \varepsilon_{ij} \tag{41}$$

the stresses can be written as

$$\sigma_{ij} = 2\mu\varepsilon_{ij} + \lambda\varepsilon_{kk}\delta_{ij} - mT\delta_{ij} \tag{42}$$

where δ_{ij} is the Kronecker delta.

Equation (42) represents the Duhamel-Neumann equations. They are constitutive equations of the isothermal theory of elasticity (Hooke's law) augmented by temperature terms $-mT\delta_{ij}$

Solving equation (42) for strains results in

$$\varepsilon_{ij} = \frac{1}{2\mu}\left(\sigma_{ij} - \frac{\lambda}{3\lambda + 2\mu}\sigma_{kk}\delta_{ij}\right) + \alpha T\delta_{ij} \tag{43}$$

In terms of shear modulus G and Poisson's ratio, ν, equations (42) and (43) become

$$\sigma_{ij} = 2G\left[\varepsilon_{ij} + \frac{\nu}{1-2\nu}\delta_{ij}\left(\varepsilon_{kk} - \frac{1+\nu}{\nu}\alpha T\right)\right] \tag{44}$$

$$\varepsilon_{ij} = \frac{1}{2G}\left(\sigma_{ij} - \frac{\nu}{1+\nu}\sigma_{kk}\delta_{ij}\right) + \alpha T\delta_{ij} \tag{45}$$

The elastic moduli are related by

$$G = E/2(1+\nu) \tag{46}$$

Considering equation (43) or (45), the first two terms on the right hand side are due to mechanical loads and also they ensure that the body remains continuous. The temperature term indicates that there is a uniform expansion proportional to the temperature rise T. The temperature term contributes only to normal strains ε_{11}, ε_{22} and ε_{33}.

3.3. FRACTURE MECHANICS CONCEPTS

Linear elastic fracture mechanics can be applied if a load is applied to a cracked body. The crack surfaces move relative to each other, and there are three possible modes of crack surface displacement. These are Mode I, the opening mode where opposing crack surfaces move directly apart, Mode II, the slipping mode, where crack surfaces move over each other along the crack line, and Mode III, the tearing mode where crack surfaces move over each other perpendicular to the crack line[33]. This is illustrated in Figure 3.2

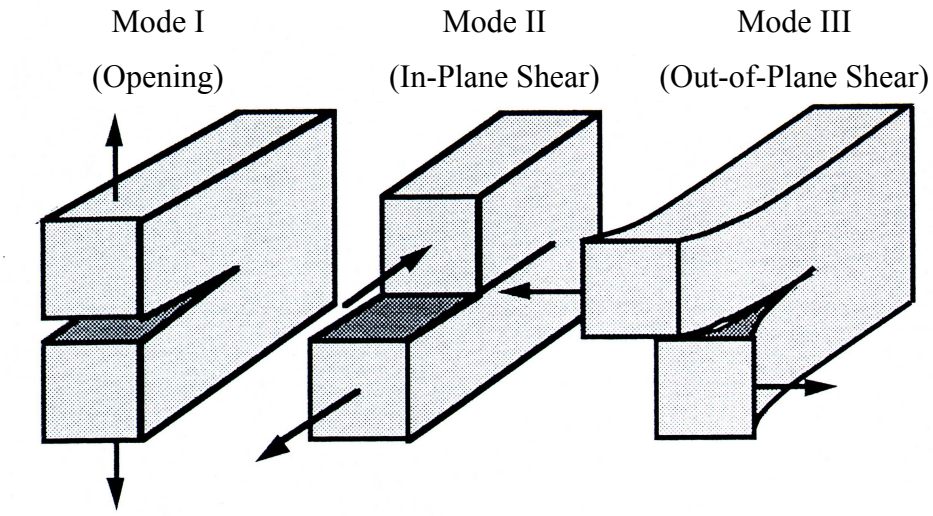

Figure 3.2. The three modes of loading that can be applied to a crack

Each mode of loading produces $1/\sqrt{r}$ singularity at the crack tip. Stress tends to be unbounded at the crack tip (as r $\Rightarrow$ 0), as shown in Figure 3.3.

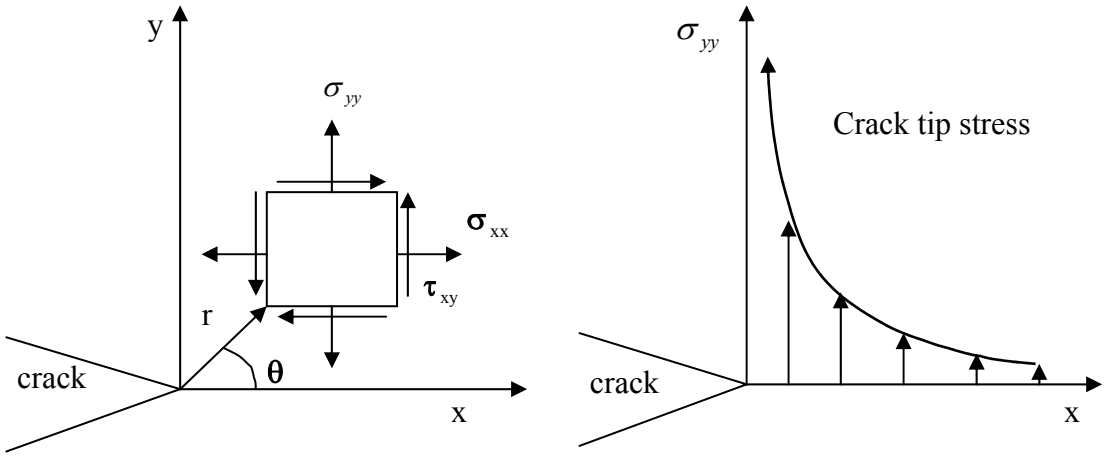

(a) Coordinate axis near the crack tip (b) Crack tip stress singularity

Figure 3.3. Crack tip stress singularity

3.4. INELASTIC CONCEPTS

3.4.1. Linear Visoelastic Model. Refractory materials will generally behave in a linear elastic manner at lower temperatures and in a nonlinear inelastic manner at higher temperatures, traditionally inelastic behavior included creep and stress relaxation of materials. The time-dependent phenomena may have a significant effect on the stress distribution thereby on the deformation developed in a member. Therefore, a linear viscoelastic theory is needed for the analysis of refractories under to hightemperature loading. All linear viscoelastic models are combination of linear springs and linear viscous dashpots as are shown in Figure 3.4 Viscoelasticity models (a), with the following relationships[34].

For linear spring:

$$\sigma = E\varepsilon \tag{47}$$

For linear dashpot:

$$\sigma = \eta \frac{d\varepsilon}{dt} = \eta \dot{\varepsilon} \tag{48}$$

where: σ = stress

E = linear spring constant or Young's Modulus

ε = strain

η = coefficient of viscosity

t = time

$\dot{\varepsilon}$ = strain rate

The spring element has instantaneous elasticity and instantaneous recovery. The dashpot will be deformed continuously at a constant rate when it is subjected to a step of constant stress. In other words, if a constant strain is imposed on the dashpot, the stress will then rapidly diminish and approach zero.

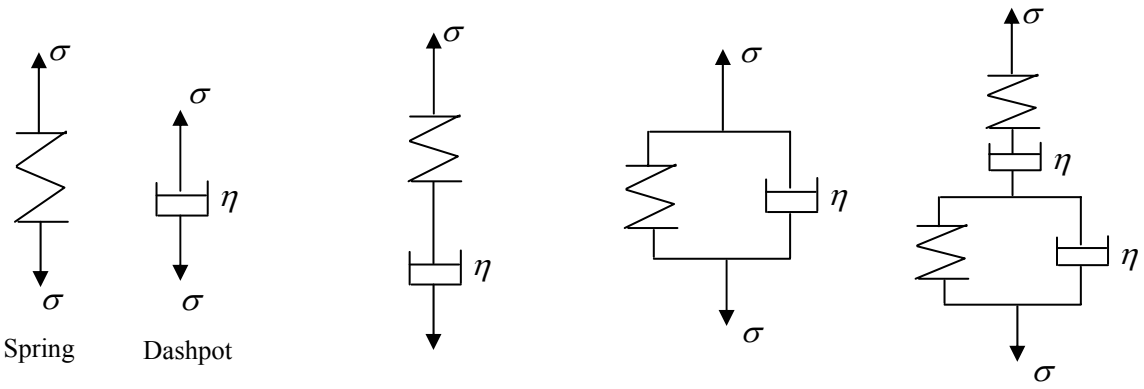

(a) spring and dashpot (b) Maxwell Model (c) Kelvin Model (d) Burgers Model

Figure 3.4. Viscoelasticity models

Several visoelastic models have been defined. The first two are the Maxwell and Kelvin models[34], which consist of a single linear spring and a single linear viscous dashpot in series and parallel, respectively.

Maxwell model:

$$\dot{\varepsilon} = \frac{\dot{\sigma}}{E} + \frac{\sigma}{\eta} \tag{49}$$

Kelvin model:

$$\dot{\varepsilon} = \frac{\sigma_o}{\eta} e^{-Et/\eta} \tag{50}$$

where: $\dot{\sigma}$ = stress rate

σ_o = constant stress at t = 0

Neither the Maxwell model nor the Kelvin model is accurate for the viscoelastic behavior. The Maxwell model shows no time-dependent recovery and does not show the decreasing strain rate under constant stress. The Kelvin model does not exhibit time-independent strain on loading or unloading and does not describe a permanent strain after unloading.

By combining Maxwell and Kelvin models in series, a more accurate model, the Burger's Model is obtained[34]. The strain in this model will be related to a spring in series with both a dashpot and a combination of a spring and dashpot in parallel. The Burger's Model is expressed as:

$$\dot{\varepsilon} = \frac{\sigma_o}{\eta_1} + \frac{\sigma_o}{\eta_2} e^{-E_2 t/\eta_2} \tag{51}$$

where: η_1 = coefficient of viscosity for the series dashpot

η_2 = coefficient of viscosity for the parallel dashpot

E_2 = Young's Modulus for the parallel spring

The creep behavior of the Burger's model is the sum of the creep behavior of the Maxwell and Kelvin models. It represents both the instantaneous elastic strain and viscous flow of the Maxwell model and the delayed elasticity of the Kelvin model.

3.4.2. Creep In Refractories. Deformation and failure behavior of refractories at very high temperature is predominantly governed by creep effects[35-38].

Creep is the time dependent deformation of a material under combined influence of temperature and applied stresses. Various mechanisms may allow creep to occur. Figure 3.5 illustrates a typical creep curve for a tensile specimen. The creep strain-time curve can be divided into three distinct regions: (I) primary creep, (II) secondary creep and (III) tertiary creep.

The primary creep represents the interval in which the structure is change and is characterized by a decreasing strain rate. The secondary creep region of the curve is the most useful for predicting the life of a ceramic material. It is often referred to as steady state or constant rate creep. The steady state creep rates of refractory materials are affected by the temperature, applied stress, structure of single crystals, microstructure of polycrystalline ceramics, composition, stoichiometry of crystal phases, and environment.

The creep response of refractory materials in steady state has been expressed in different equation form. One of the popular forms is given by [30]:

$$\varepsilon = e^a t^b \sigma^n \exp\left(-\frac{Q}{RT}\right) \tag{52}$$

where: ε = creep strain

a, b = constant

σ = stress

n = stress exponent

Q = activation energy

R = gas constant

T = absolute temperature

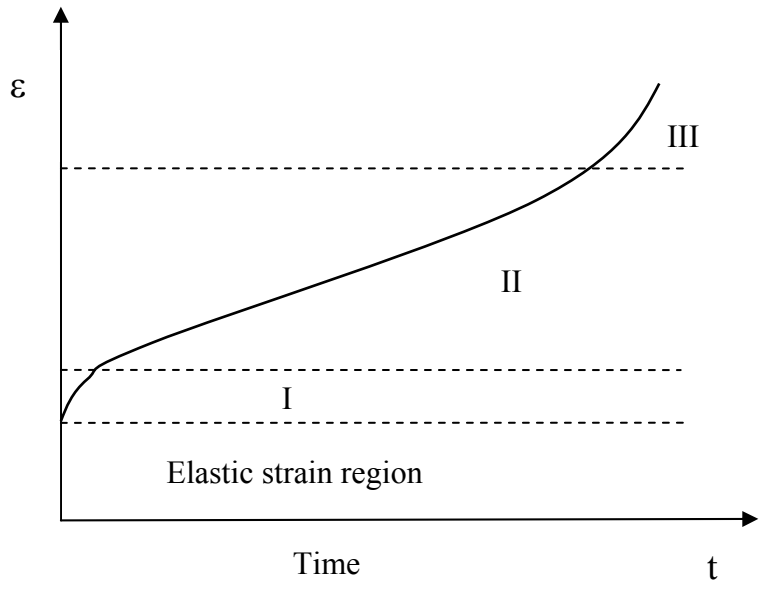

Figure 3.5. Typical creep curve for ceramic materials

Another popular equation is the Norton-Bailey Arrhenius creep equation[36] by setting the b = 1 in equation (52):

$$\dot{\varepsilon} = A\sigma^{n} \exp\left(-\frac{Q}{RT}\right) \tag{53}$$

where: $\dot{\varepsilon}$ = creep strain rate

A = constant

A recent unpublished data generated at ORNL indicate that the time dependent changes in the microstructure for some refractories can also affect the creep behavior in the absence of an applied stress, equation (53) can be modified by including a second temperature dependent term to account for this effect:

$$\dot{\varepsilon} = A\sigma^n \exp\left(-\frac{Q_c}{RT}\right) + B\exp\left(-\frac{Q_a}{RT}\right) \tag{54}$$

where, A and B are constants, Q_c is the activation energy for creep and Q_a is the activation energy for the microstructural-dependent aging.

4. FORMULATION OF THE GLASS FURNACE CROWN PROBLEM

A typical glass furnace crown system is shown in Figure 4.1 as refractory lining arch construction. The crown typically terminates at a skew at each end, and is supported by continuous horizontal steel beam along the exterior end of each skew. The skew transmits the vertical force to the supporting wall and transmits the horizontal force to the external steel beam. The steel beam is connected to vertical columns which are spaced at uniform intervals. The base of each vertical column is designed as a pin connection, allowing the column to rotate from the base without resistance. The top ends of each pair column are connected by a spring and bolt system. The spring stiffness is chosen to resist the crown horizontal thrust due to gravity load. The bolts are loosened periodically during the initial heat up to allow for the appropriate horizontal outward movement of the horizontal beams and skew bricks and the resulting crown expansion allowance.

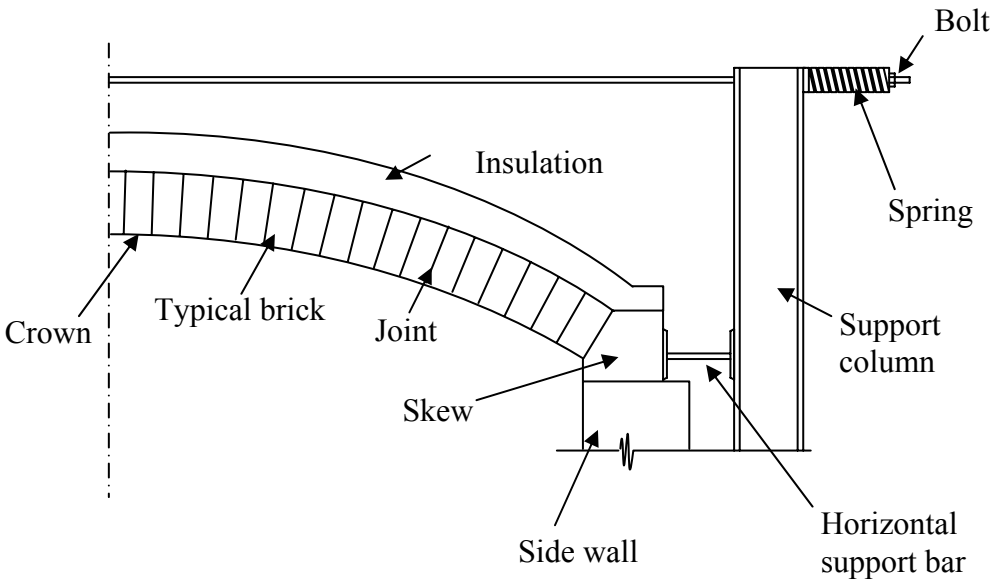

Figure 4.1. The support details of sprung arch

The primary load-carrying part of crown is shown as brick components. The crown consists of one or several layers of bricks. The bricks are connected by mortar or have dry joints. The crown is covered by insulation materials to decrease the heat loss.

4.1. FORMULATION

4.1.1. Two-Dimensional Theory of Thermoelasticity. In many engineering applications, three-dimensional problems may be idealized as two dimensional to simplify the analysis. If one of the dimensions is small in comparison with the other dimensions, then the stress in the direction of the small dimension is negligible. This case is called plane stress. On the other hand, if one dimension is extremely large in comparison to the other two dimensions, then the strain in this direction will be negligible. This condition is called plane strain[39]. Plane problems of both types are illustrated by Figure 4.2.

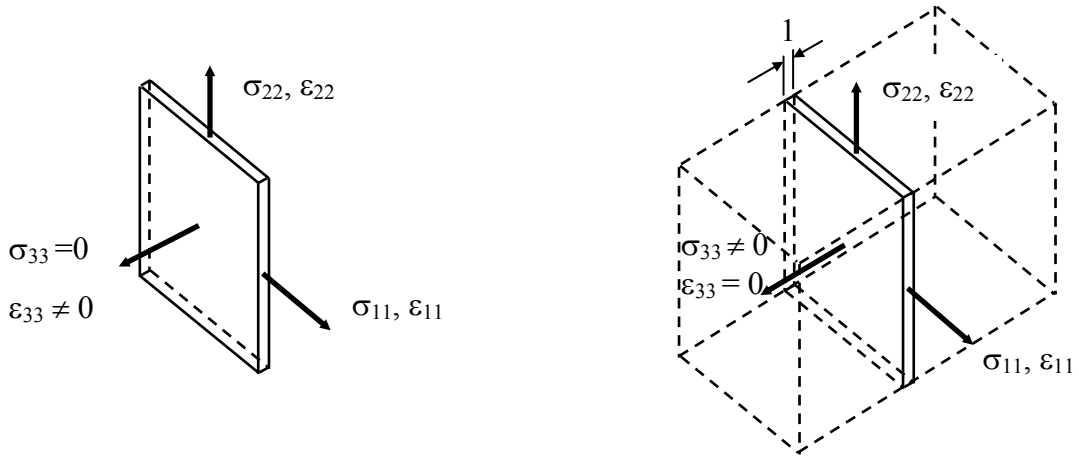

(a) Plane stress condition (b) Plane strain condition

Figure 4.2. Plane stress and plane strain conditions

In the absence of heat sources, the stationary two-dimensional heat conduction equations is written in terms of rectangular coordinates (x_1, x_2) as[40]:

$$\frac{\partial q_1}{\partial x_1} + \frac{\partial q_2}{\partial x_2} = 0 \tag{55}$$

where q_1 and q_2 are the components of the heat flux vector. For isotropic media, the Fourier heat conduction law is expressed as

$$q_1 = -k\frac{\partial T}{\partial x_1} \qquad q_2 = -k\frac{\partial T}{\partial x_2} \tag{56}$$

where T is the temperature which is a function of x_1 and x_2, and k is the thermal conductivity. Substituting equations (56) into (55), we get the two-dimensional Laplace equation governing the temperature field is obtained:

$$\nabla_1^2 T = 0 \tag{57}$$

The general solution of equation (57) can be expressed in terms of an analytic complex function $\theta(z)$:

$$T(x_1, x_2) = \frac{1}{2}\left[\ \theta(z) + \overline{\theta(z)}\ \right] \tag{58}$$

where $z = x_1 + ix_2$ and an overbar is used to indicate a conjugate complex quantity. The partial derivatives of temperature $T(x_1, x_2)$ with respect to coordinate variables x_1 and x_2 are given by

$$\partial T/\partial x_1 = \frac{1}{2}\left[\theta'(z) + \overline{\theta'(z)}\right] \qquad \partial T/\partial x_2 = \frac{1}{2}i\left[\theta'(z) + \overline{\theta'(z)}\right] \tag{59}$$

For the two-dimensional problems, the equilibrium equations (in the absence of body forces) and the compatibility equation are written as

$$\frac{\partial \sigma_{11}}{\partial x_1} + \frac{\partial \sigma_{12}}{\partial x_2} = 0 \tag{60}$$

$$\frac{\partial \sigma_{12}}{\partial x_1} + \frac{\partial \sigma_{22}}{\partial x_2} = 0 \tag{61}$$

$$\frac{\partial^2 \varepsilon_{11}}{\partial x_2^2} + \frac{\partial^2 \varepsilon_{22}}{\partial x_1^2} = \frac{\partial^2 \varepsilon_{12}}{\partial x_1 \partial x_2} \tag{62}$$

Based on the glass furnace crown construction and the plane problem theory, the glass furnace crown problem can be simulated as two-dimensional plane strain problem. In plane strain condition, the strain-stress relationship can be expressed by the following equations:

$$\varepsilon_{11} = \frac{\left(1-\nu^2\right)}{E}\sigma_{11} - \frac{\nu(1+\nu)}{E}\sigma_{22} + (1+\nu)\alpha T \tag{63}$$

$$\varepsilon_{22} = \frac{\left(1-\nu^2\right)}{E}\sigma_{22} - \frac{\nu(1+\nu)}{E}\sigma_{11} + (1+\nu)\alpha T \tag{64}$$

$$\varepsilon_{12} = \frac{1+\nu}{E}\sigma_{12} \tag{65}$$

where σ and ε are the stress and strain tensor, respectively, E is Young's modulus, μ is the shear modulus, and ν is Poisson's ratio.

By introducing the Airy stress function ϕ such that:

$$\sigma_{11} = \frac{\partial^2 \phi}{\partial x_2^2} \qquad \sigma_{22} = \frac{\partial^2 \phi}{\partial x_1^2} \qquad \sigma_{12} = -\frac{\partial^2 \phi}{\partial x_1 \partial x_2} \tag{66}$$

The equilibrium equations (60) and (61) are satisfied. Substitute equations (63) to (65) into the compatibility equation (62), yields the governing two-dimensional thermal stress equation:

$$\nabla^4 \phi = \frac{E}{1-\nu} \alpha \nabla^2 T \tag{67}$$

where

$$\nabla^4 \phi = \frac{\partial^4 \phi}{\partial x_1^4} + 2\frac{\partial^4 \phi}{\partial x_1^2 \partial x_2^2} + \frac{\partial^4 \phi}{\partial x_2^4} \tag{68}$$

4.1.2. Glass Furnace Operating Environment. The operating life of the glass furnace crown may be several years. The arch inner face is exposed to a temperature environment of 1600^{o}C to 1700 ^{o}C, because of effects of the insulation material, the temperature on the outer face of the crown can reach 1400 ^{o}C to 1600 ^{o}C[30]. The inner face of the crown is referred to as the hot face and the outer face is referred to as the cold face according to the temperature environment.

The initial heating of the glass furnace is done very slowly in order to avoid the stability problem of the crown due to the large expansion difference through the thickness. Once the tank reaches the operating temperature, cooling will not occur until the end of the glass furnace life or unless the refractories need to be repaired. Large thermal stresses are generated during heat up and cool down. The stiffness of the spring supporting system of the crown is set to resist the thrust due to gravity before heating up. The supporting bolts are loosened periodically during heating up to allow the crown to expand. Then the outward displacement of the crown is constrained after initial heating up.

4.1.3. Geometrical Parameters. Here consider only the crown with one layer of bricks, and because of symmetry, half crown was considered shown in Figure 4.3. The crown consists of one skew at the crown end and a half brick at the crown center, and

there are nine bricks between the skew end and the center brick. The brick-to-brick joints are chosen as dry (unmortared) joints.

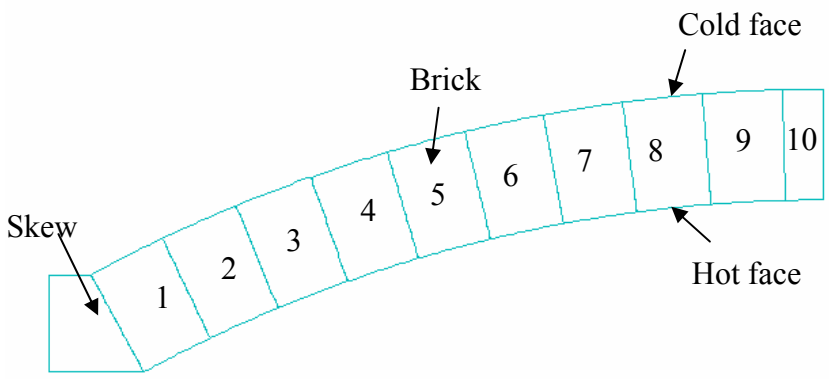

Figure 4.3. Schematic illustration of half arch

The bricks are numbered to as brick 1 to 10 from the arch skew side to the crown center. The inner face of the crown was referred to as the hot face and the outer face was referred to as the cold face according to the temperature environment. The weight of insulation materials are not considered, the effect of the insulation is assumed only acting on the cold face temperature.

The crown dimensions and specifications are provided by the glass and refractory industries and similar to that used by Schacht and Hribar[30]. Geometric parameters for the crown are given in Figure 4.4.

With reference to Figure 4.4, the thickness of crown t = 0.228 m, the inner radius r = 2.8 m, the half span S = 1.4 m, the center angle $\theta = 30^{o}$, and the length of skew bottom L = 0.2 m.

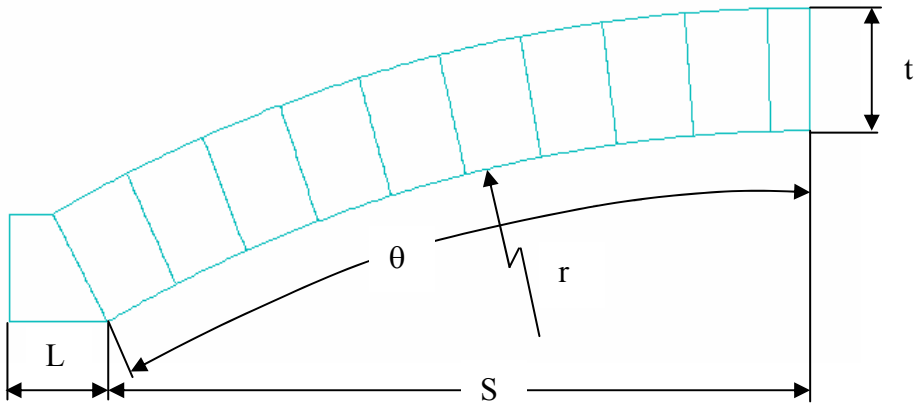

Figure 4.4. Geometry of arch considered in the model

4.1.4. Material Parameters. Temperature dependent material properties were used for mullite refractory, the properties data are from the tests conducted at the Oak Ridge National laboratory (ORNL) by Hemrick[19]. The thermal and mechanical data are given in Table 4.1.

Table 4.1. Material parameters of the skew and bricks

Temperature T (^{o}C)	Young's Modulus E (GPa)	Poisson Ratio ν	Density ρ (g/cm^3)	Thermal expansion α (1/^{o}C)	Thermal Conductivity K (W/m K)	Specific Heat C (J/gK)
23	143	0.238	2.70	5.3E-6	2.8	0.766
100	--					0.83
400	130					0.97
700	--					1.05
800	102					--
1000	--					1.10
1400	--					1.13

The creep data is given by the Norton-Bailey Arrhenius creep equation (53):

$$\dot{\varepsilon} = A\sigma^{n} \exp\left(-\frac{Q}{RT}\right) \tag{53}$$

the following values are used for the parameters:

$A = 6.76 \times 10^{-3}$

$n = 0.6$

$Q = 70$ kcal/mol

$R = 1.987$ cal/K

4.2. FINITE ELEMENT MODEL

As the creep laws provided by ABAQUS are unable to fit the experimental data, a creep subroutine is needed for the creep analysis. Because the creep tests are usually applied to single bricks, the bricks are under constant pressure and exposed to constant temperature environment with no temperature gradient through the brick. The glass furnace crown is made up of many bricks, there would be interaction between bricks and temperature gradients through the brick thickness. As a result, the stress developed in the brick is much different form the samples in the creep test. It is hard to compare the test result with the crown model results thereby verify the creep model.

A single brick creep model is needed to compare with the experimental data, and then this creep model is used in finite element analysis of the crown.

4.2.1. Finite Element Model of Single Brick. A two dimensional brick model was created as shown in Figure 4.5. The brick is symmetric about its center line, and is supported on a rigid base. A constant axial pressure P = 0.2 MPa was applied on the brick top face. The temperature field in the brick is constant at 1500^{o}C.

A quasi-static finite element analysis for single brick modeling was developed by creating the necessary finite element mesh using ABAQUS-CAE pre-processor package. ABAQUS-CAE has a very good interface between user and ABAQUS software, it provides all the tools from creating parts, assembly, mesh, until writing input file, running the model, it also provides tools for post processing.

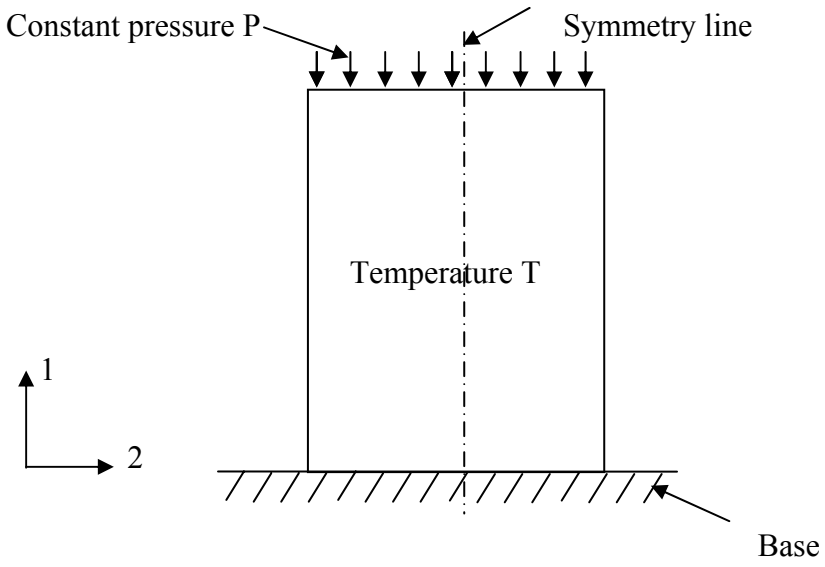

Figure 4.5. Schematic illustration of single brick model

As the geometry of the brick is simple and only the creep analysis is of interest, free mesh is used since it is easy to create. The mesh was made coarse in the model to save time and space.

The brick is modeled with 4-node bilinear coupled temperature-displacement solid plane strain elements (CPE4T). Figures 4.6 (a) gives the node and face numbering of the element and (b) gives the numbering of integration points for output[28].

Coupled temperature-displacement element CPE4T uses linear interpolation for the temperature and displacements. The elements have temperatures at all nodes. The thermal strain is taken as constant throughout the element because it is desirable to have the same interpolation for thermal strains as for total strains so as to avoid spurious hydrostatic stresses.

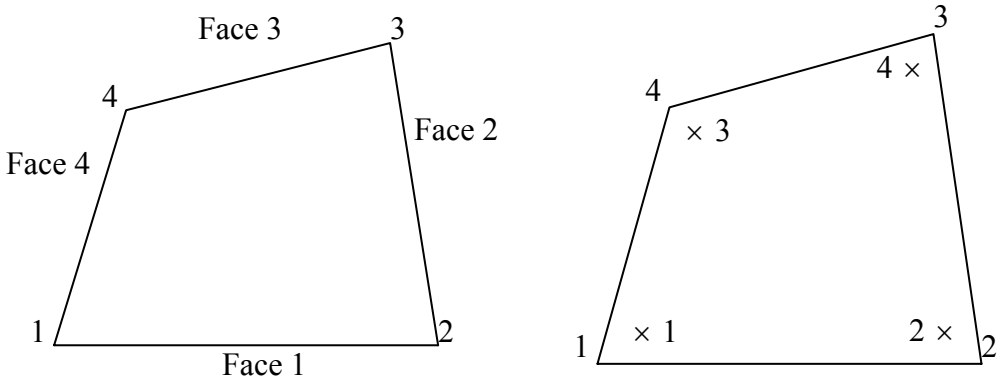

(a) Node and face numbering (b) Numbering of integration points

Figure 4.6. Schematic diagram of two-dimensional coupled temperature-displacement plane strain solid element (CPE4T)

The coordinate system is in rectangular coordinate system as shown in Figure 4.7. Axis 1 is the global x direction, axis 2 is the global y direction, and the z direction axis is not needed in two dimensional problems.

The creep behavior of mullite refractory is defined by user subroutine CREEP which will be illustrated in the next section. The subroutine is written in FORTRAN code. The creep subroutine will be called by ABAQUS for creep analysis when the option *CREEP=USER is used in the model.

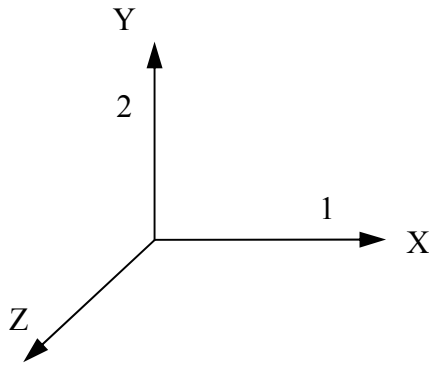

Figure 4.7. Rectangular coordinate system

4.2.2. Finite Element Model for the Arch. The glass furnace crown modeling in ABAQUS commercial finite element package was developed by creating the necessary finite element mesh using I-DEAS pre-processor package. The model generated in I-DEAS proved to be useful due to its ease of operation and the efficient exporting to create the necessary ABAQUS input files.

Because of the arch shape of glass furnace crown, it is convenient to have two different coordinate systems for skew and crown, respectively. ABAQUS provides an option *ORIENTATION to define a local coordinate system[19].

The global coordinate system of the model is Cartesian coordinate system, base on the geometry of the arch, it is convenient to use cylindrical coordinate system for the crown part. A cylindrical coordinate system is defined by giving the two points, a and b, on the polar axis of the cylindrical system, as shown in Figure 4.8. The local axes are X'=radial, Y'=tangential, Z'=axial.

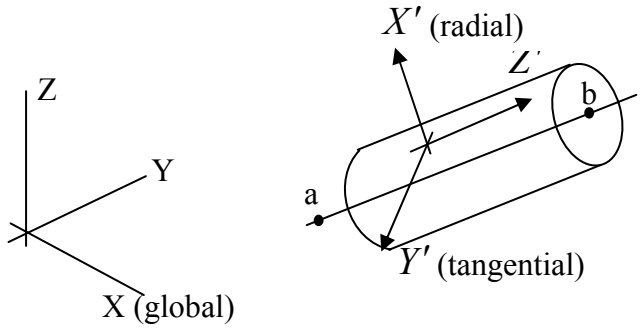

Figure 4.8. Definition of cylindrical coordinate system from rectangular coordinate system

Figure 4.9 gives the illustration of model coordinate systems, the skew is in rectangular coordinate, axis 1 is the global x direction, axis 2 is the global y direction, crown is in cylindrical coordinate system, axis R is the local radial direction, axis T is the local tangential direction.

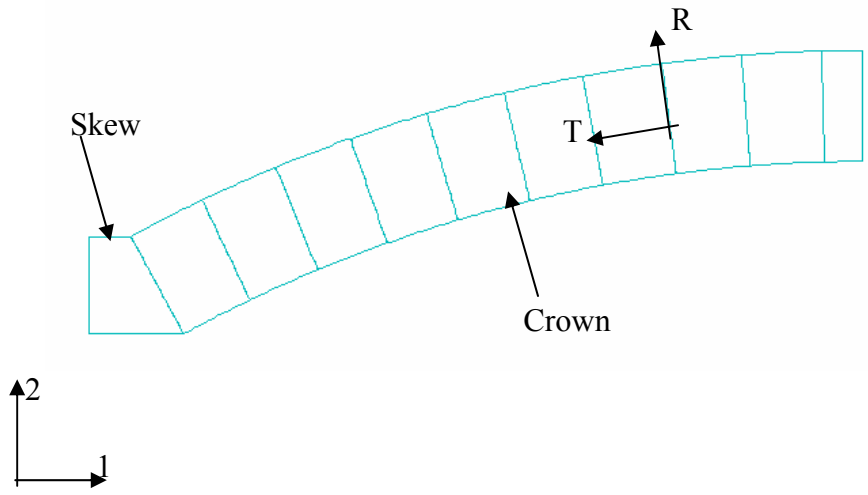

Figure 4.9. Schematic illustration of model coordinate systems

According to the arch construction and its support details, the tangential displacement of the arch center is constrained, the arch center can only move vertically. On the skew end, y direction displacement of the skew is constrained. During its initial heat up, the crown is free to expand in the x direction, and a constant force is applied on the skew end to resist the crown horizontal thrust and provide a small pressure on the crown, after initial heat up, the skew side will be fixed, the arch can not have horizontal movement anymore.

The mesh is optimazed to avoid sigularty developed due to contact and crack propagation problem. Optimum number nodes and elements are 6851 and 6300, respectively. Optimization of nodes and elements play a vital role in the convergence of problem and in reducing the machine time and memory space.

Mapped mesh is used rather than free mesh because it gives proper control on element size and element density. As the whole crown consists of single bricks which are in the same temperature environment and capable of separating, in order to avoid the singularity problem due to the contact property and crack propagation, the mesh was made very fine in the whole model.

The skew and crown bricks are modeled with 4-node bilinear coupled temperature-displacement solid plane strain elements (CPE4T) which has been introduced in single brick model.

The bricks and skew are initially bonded one by one. The bonded contact surfaces are defined by parameter *TYPE = CONTACT in option *INITIAL CONDITIONS. This option is used with the *DEBOND option to simulate the brick joints opening, i.e. crack propagation analysis[19]. For the crack propagation, there must be an initial existing crack,

so the four corners of brick are free of contact to simulate the initial crack. It is illustrated by Figure 4.10.

Debonding at the corners is also observed in experimental and industrial brick construction, so this assumption is valid.

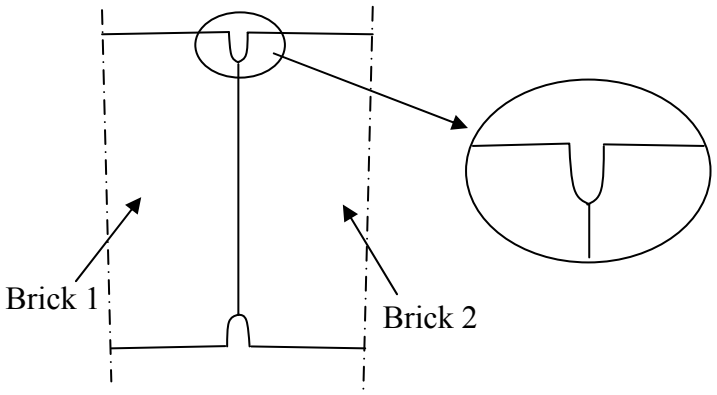

Figure 4.10. Brick contact surfaces illustration

The contact between two bricks is defined in terms of two surfaces that may interact with each other. These surfaces are called a "contact pair". The order in which the two surfaces are specified on the contact pair is critical. For each node on the first surface (the "slave" surface), ABAQUS attempts to find the closest point on the second surface (the "master" surface), as shown in Figure 4.11. The interaction is then discretized between the point on the master surface and the slave node[19].

Temperature gradients in the crown cause different amount of expansion through the thickness of the crown, it induces significant stress levels in the crown. As the arch

geometry changes, the new expanded crown does not fit the installed skew position due to two primary changes: the expanded size due to the average increase in temperature and the rotation due to the through thickness temperature differences, these changes cause the arch to transform from having all of its joints in contact to a three-hinged arch configuration. The brick joints will separate under this condition, and then affect the stress distribution and heat transfer. The creep in the refractory crown also affects stress distribution such as causing serious stress relief, and the failure behavior of refractiries at very high temperature is often dominated by creep effects as well.

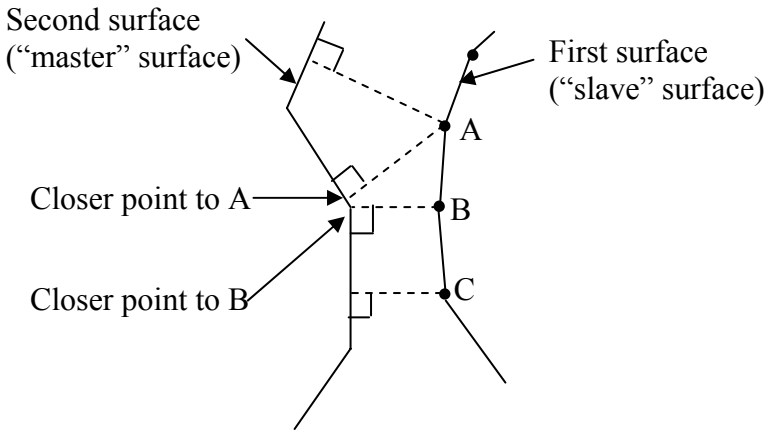

Figure 4.11. Contact and interaction discretization

Therefore, a fully coupled thermal-displacement analysis which includes crack propagation and creep analysis was conducted to simulate the crown operation conditions.

Transient heat transfer was used for the establishment of temperature field, a temperature of 1600^{o}C was applied on the crown hot-face and a steady state was defined

as when the cold face reaches around 1400 ^{o}C. This accounts for the thermal conductivity of the bricks, the effects of insulation and the heat loss on the cold face.

The brick joint opening is simulated as a propagating crack. In the model code, a critical stress criterion is selected for the crack propagation analysis. Figure 4.12 gives the illustration of the crack propagation process. The crack tip node debonds when the local stress across the interface at a specified distance ahead of the crack tip reaches a critical value at a critical distance ahead of the crack tip.

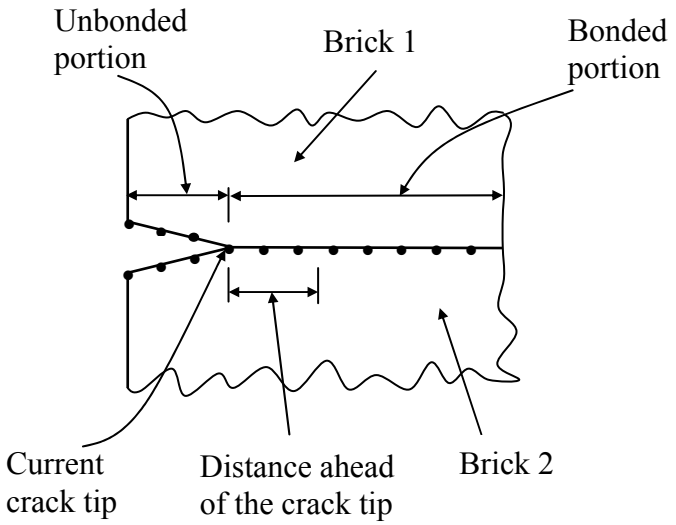

Figure 4.12. Critical stress criterion illustration

The critical stress criterion is defined as[19]:

$$f = \sqrt{\left(\frac{\hat{\sigma}_n}{\sigma^f}\right)^2 + \left(\frac{\tau_1}{\tau_1^f}\right)^2 + \left(\frac{\tau_2}{\tau_2^f}\right)^2}, \qquad \hat{\sigma}_n = \max(\sigma_n, 0) \tag{69}$$

where σ_n is the normal component of stress carried across the interface at the distance

specified; τ_1 and τ_2 are the shear stress components in the interface; and σ^f and τ_1^f are the normal and shear failure stresses, which must be specified. The second component of the shear failure stress τ_2 is not relevant in a two-dimensional analysis. Therefore, the value of τ_2^f need not be specified. The crack-tip node debonds when the fracture criterion, f reaches the value 1.0.

If the value of τ_1^f is not given or is specified as zero, it will be taken to be a very large number so that the shear stress has no effect on the fracture criterion[19].

The value of σ^f is specified as 500 Pa since the brick joints can not stands high tensile stress. And because the brick joint opening is controlled by the stress normal to the crack plane in this case, the value of critical shear stress doesn't need to be specified here.

The distance ahead of the crack tip is measured along the slave surface, as shown in Figure 4.12. The stress at the specified distance ahead of the crack tip is obtained by interpolating the values at the adjacent nodes.

Since the creep laws provided by ABAQUS can not be used for mullite refractory, the creep behavior of mullite is defined by user subroutine CREEP. The subroutine is written in FORTRAN code, it increases the functionality of ABAQUS option. The creep subroutine will be called by ABAQUS at all integration points of elements for creep analysis when the option *CREEP=USER is used in the model. The creep subroutine is coded as follow:

```
SUBROUTINE CREEP(DECRA,DESWA,STATEV,SERD,ECO,ESWO,P,QTILD,
    TEMP,DTEMP,PREDEF,DPRED,TIME,DTIME,CMNAME,LEXIMP,
    LEND,COORDS,NATATV,NOEL,NPT,LAYER,KSPT,KSTEP,KINC)
```

```
      INCLUDE 'ABA_PARAM.INC'
      CHARACTER*8 CMNAME
      DIMENSION DECRA(5),DESWAZ(5),TIME(2),COORDS(*)
C     DEFINE CONSTANT AND FUNCTION
      A=6.76E-3
      AN=0.6
      AENG=7.0e4
      ACONT=1.987
      DECRA(1)=A*QTILD**AN*EXP(-AENG/ACONT/TEMP)*DTIME
      RETURN
      END
```

Nonlinear creep problems are often solved efficiently by forward-difference integration of inelastic strains. This explicit method is computationally efficient because, unlike implicit methods, iteration is not required. Although this method is only conditionally stable, the numerical stability limit of the explicit operator is usually sufficiently large to allow the solution to be developed in a small number of time increments.

ABAQUS monitors the stability limit automatically during explicit integration[19]. If, at any point in the model, the creep strain increment ($\dot{\bar{\varepsilon}}\big|_t \nabla t$) is larger than the total elastic strain, the problem will become unstable. Therefore, a stable time step, ∇t_s, is calculated every increment by

$$\nabla t_s = 0.5 \frac{\varepsilon^{el}\big|_t}{\dot{\varepsilon}^{cr}\big|_t} \tag{70}$$

where $\varepsilon^{el}\big|_t$ is the equivalent total elastic strain at time t, the beginning of the increment, and $\dot{\varepsilon}^{cr}\big|_t$ is the equivalent creep strain rate at time t. furthermore,

$$\varepsilon^{el}\big|_t = \frac{\tilde{q}\big|_t}{\tilde{E}}, \tag{71}$$

where $\tilde{q}\big|_t$ is the Mises stress at time t, and

$$\tilde{E} = 2(1+\nu)\left(n : D^{el} : n\right) \approx 2.5\bar{E} \tag{72}$$

in which

$n = \partial\tilde{q}\big|_t / \partial\sigma$ is the gradient of the deviatoric stress potential,

D^{el} is the elasticity matrix, and

$\bar{E}$ is an effective elastic modulus, for isotropic elasticity $\bar{E}$ can be approximated by Young's modulus.

5. RESULTS AND DISCUSSION

In this chapter, the creep result of the single brick model is given to validate the creep model. After validating, the creep model is used for the whole glass furnace crown model. Then, the results of thermo-mechanical analysis during initial heat up are given. Last, the time dependent performance of the crown is given.

5.1. SINGLE BRICK MODEL RESULT

The creep strain result from the model is compared with the experimental data, the creep strain curves are given by Figure 5.1. The creep strain result from the model fits the experimental data very well. This result gives confidence that the creep model can be used for the simulation of whole glass furnace crown.

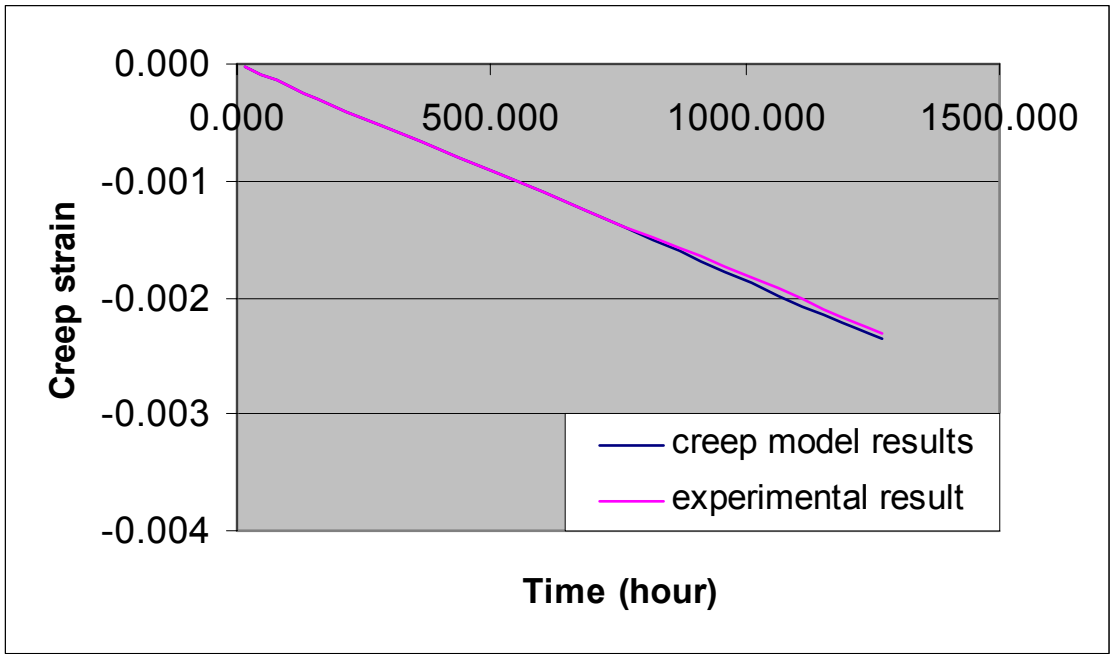

Figure 5.1. Single brick compressive creep strain curve

5.2 GLASS FURNACE CROWN MODEL RESULTS

5.2.1 Heat Transfer Results. Temperature field in the arch after initial heat up is given by Figure 5.2. The heat transfers from the crown hot face to its cold face gradually. In the end of initial heat up, the temperature decreases evenly through the thickness of the crown. The temperature on the hot face is 1600 ^{o}C and the temperature on the cold face is around 1450 ^{o}C, the arch end is the lowest temperature area. The lowest temperature is about 1025 ^{o}C.

Due to crack opening and because there is no insulation on the skew, the heat flow in the skew would be different from that in the crown bricks, leading to a discontinuous temperature distribution between the skew and the crown brick.

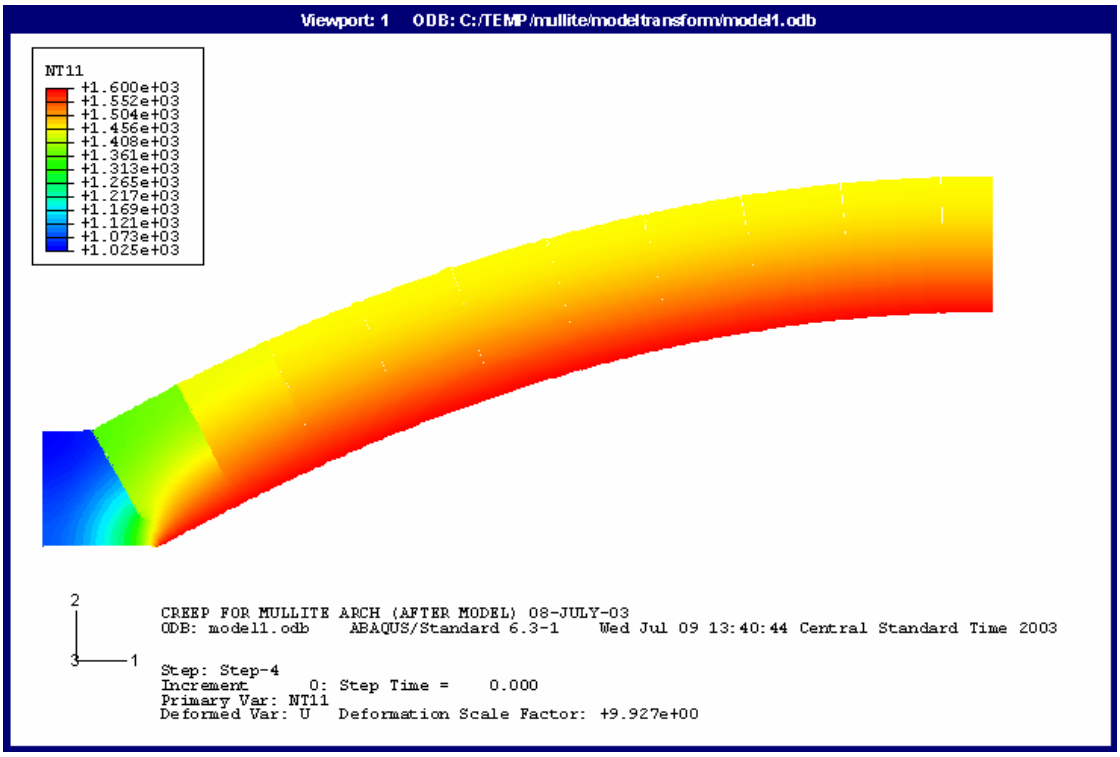

Figure 5.2. Temperature field of the arch after initial heat up

The change of arch center temperature through the crown thickness is given by Figure 5.3 (the zero thickness is defined on the crown hot face in this thesis), the temperature decreases from the hot face at 1600 ^{o}C to the cold face at about 1450 ^{o}C, the temperature gradient is the source of the thermal stresses and deformation of the crown.

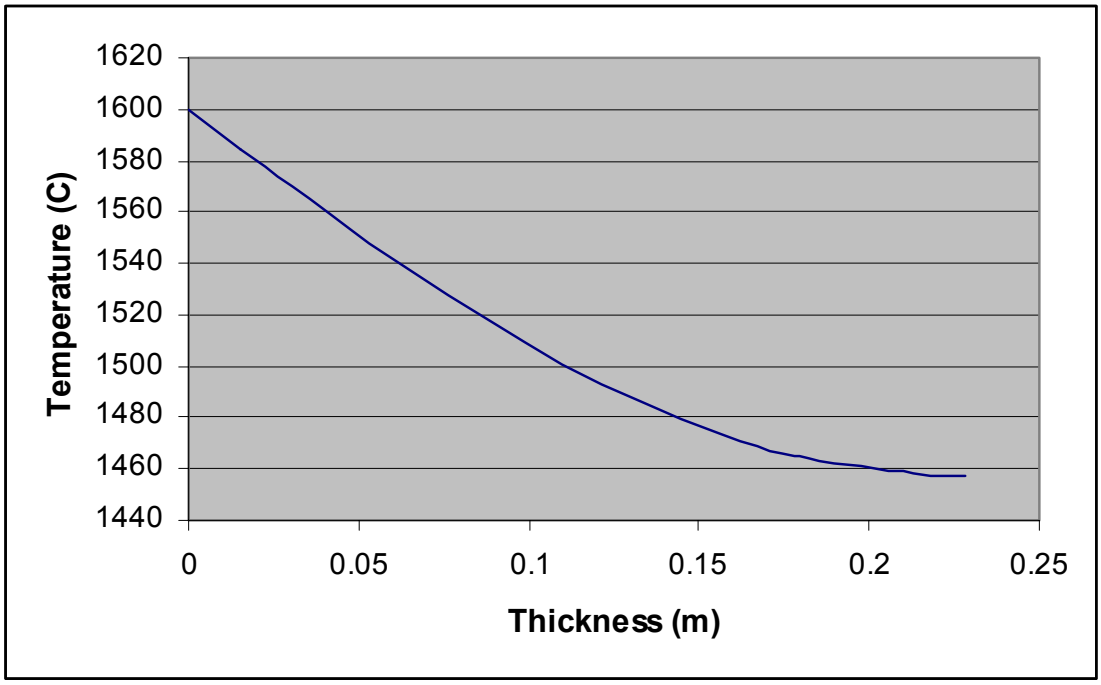

Figure 5.3. Through thickness temperature after initial heat up

5.2.2 Deformation During Heat Up. In the very beginning of initial heat up, when the hot face area reaches a very high temperature, the temperature on crown cold face is still at the room temperature. This results in a high temperature gradient in the crown. Temperature gradients in the crown cause differential expansion through the thickness of the crown and sequentially cause tensile stresses on the cold face and

compressive stresses on the hot face which is shown by Figure 5.4. Because the skew and crown are in different coordinate system, the stress in the skew shown in figure is the y direction stress, while the stress in the crown part in tangential stress.

Since the brick joints can not stand high tensile stresses, brick joints along the cold face open immediately. As the heat continually transfers through the bricks, the temperature gradients in the crown gets smaller and, stresses in the crown release, the differential expansion decreases, thereby decreasing the opening.

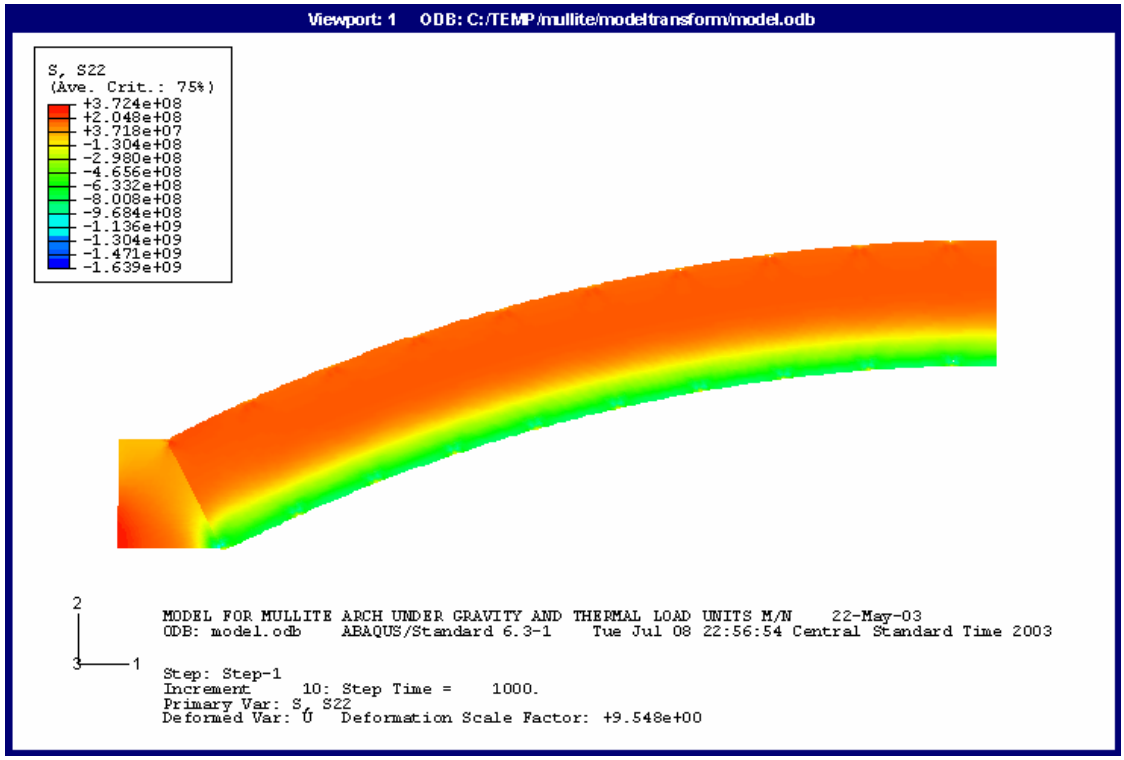

Figure 5.4. Tangential stress before brick joints open

Skew end x direction displacement is given in Figure 5.5. The arch moves outward rapidly in the beginning of heat up. As the temperature increases, the crown moves at a lower rate. At the end of initial heat up, the displacement of the arch end is approximately 0.0167 m. Then the skew end will be fixed for the subsequent analysis.

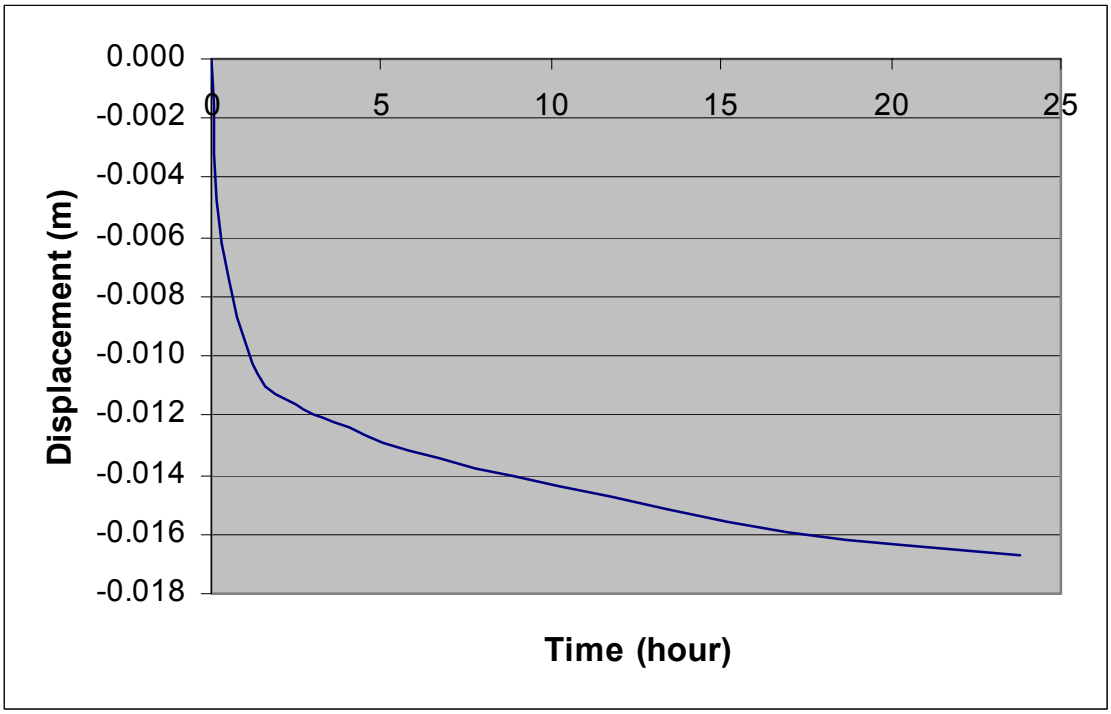

Figure 5.5. Skew end displacement during initial heat up

Figure 5.6 shows deformed arch after initial heat up compared with the original arch.

It illustrates that all the brick contact surfaces separated during heat up, the joint opening starts from the crown cold face and ends near the crown hot face. For the sake of discussion, the cracks are referred to as brick 1 to 10 from the arch skew side to the

crown center. Because of the thermal expansion and the brick openings, the size of the crown increases and moves up slightly during heat up. The rise of the arch center at the end of initial heat up is about 0.0125 m.

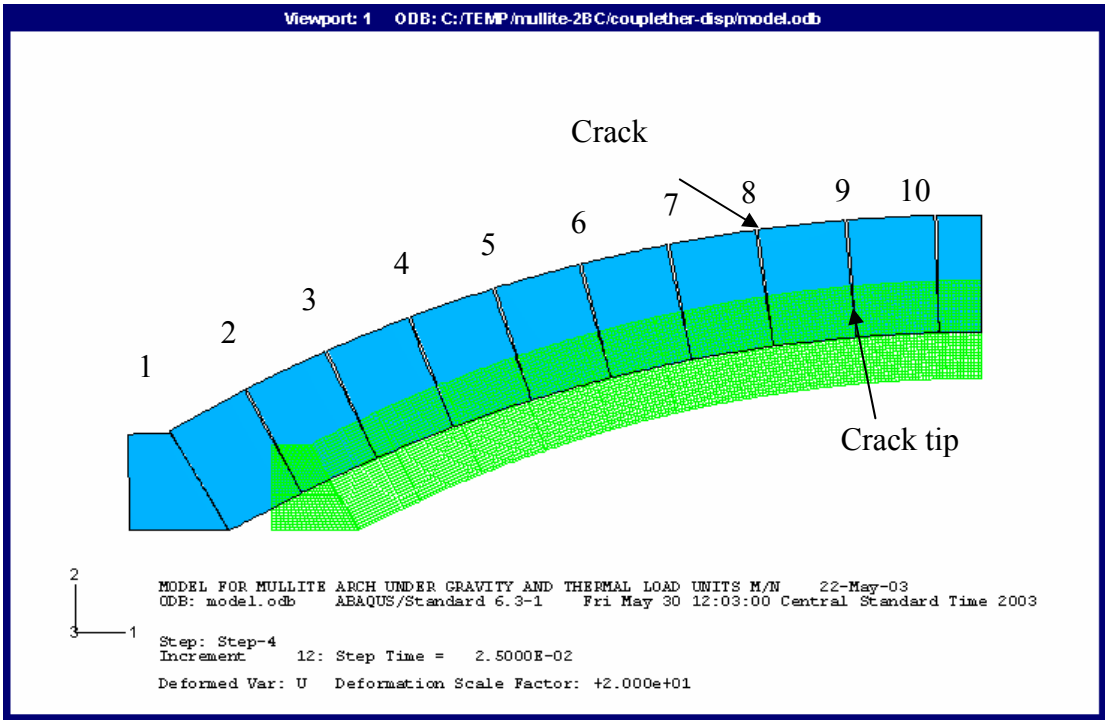

Figure 5.6. Deformed crown after initial heat up

5.2.3 Stress in the Crown During Heat Up. The stresses developed along the center line of brick 5 and brick 10 and the stresses along the crack 5 and crack 10 are chosen for discussion in below. Refer to Figure 4.3 and Figure 5.6 for the locations of bricks and cracks, respectively.

The tangential stress distribution after initial heat up is given in Figure 5.7. The through thickness tangential stress diagram of the crown is given in Figure 5.8.

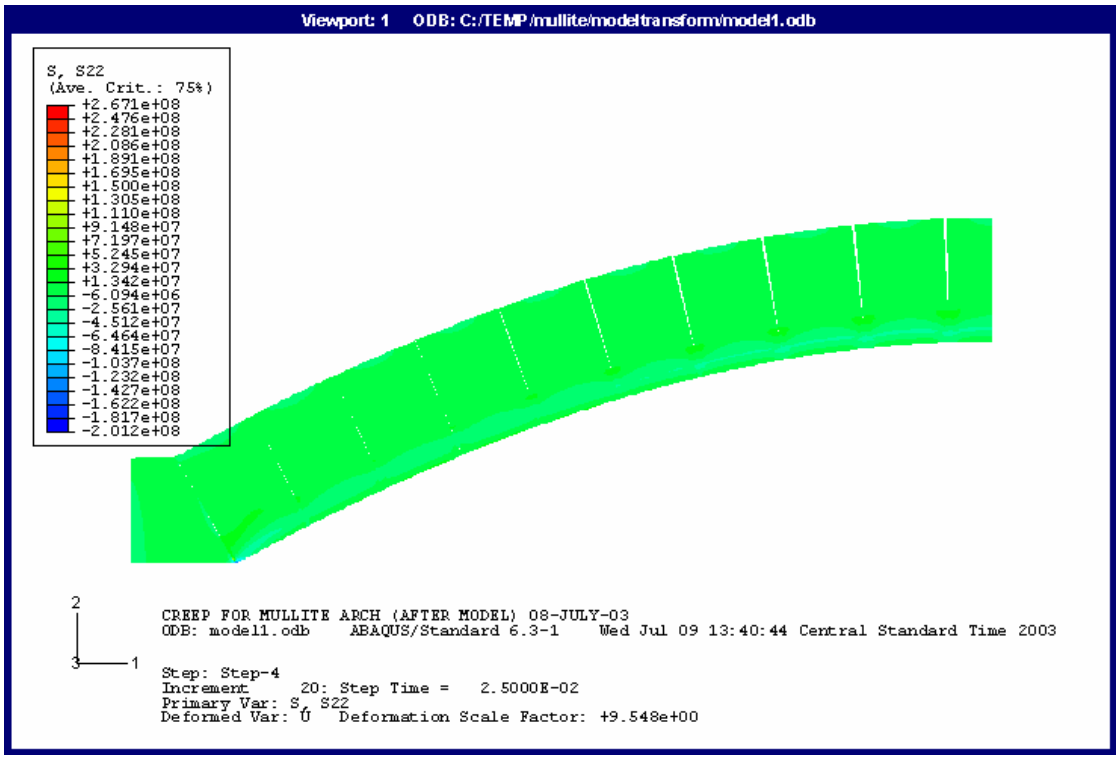

Figure 5.7. Tangential stress distribution in the crown after initial heat up

Because of the joint openings, the opened portions of the bricks are in free expansion state. The differential expansion caused by the temperature gradients produces the stresses in this part. Just like the stresses developed in pure bending specimen, compressive tangential stress is developed in the cold face of the bricks, tensile tangential stress is developed in the near hot face region of opened portion. Because of the shape of the brick corners defined before, the center of brick hot face experiences a tensile tangential stress as well. In the other part of the unopened portion of the brick, high compressive tangential stresses are developed. This agrees with the results of Schacht and Hribar[30]. The tangential stresses along the opened portion of the crack surface are tensile but quite small in comparison with the stresses inside the bricks. The crack tip regions

experience highest tensile stress which shows the crack tip singularity. The unopened portion along the crack plane experiences a stress coupled with compressive stresses on the hot face. The stresses inside the bricks range between ± 10 *MPa* in the opened portion, and from -25 *MPa* to 10 *MPa* in the unopened portion. The stresses along the cracks are less than 3 *MPa* in the opened portion, and from -35 *MPa* to 25 *MPa* in the unopened portion. The stresses developed in different bricks are almost in the same range.

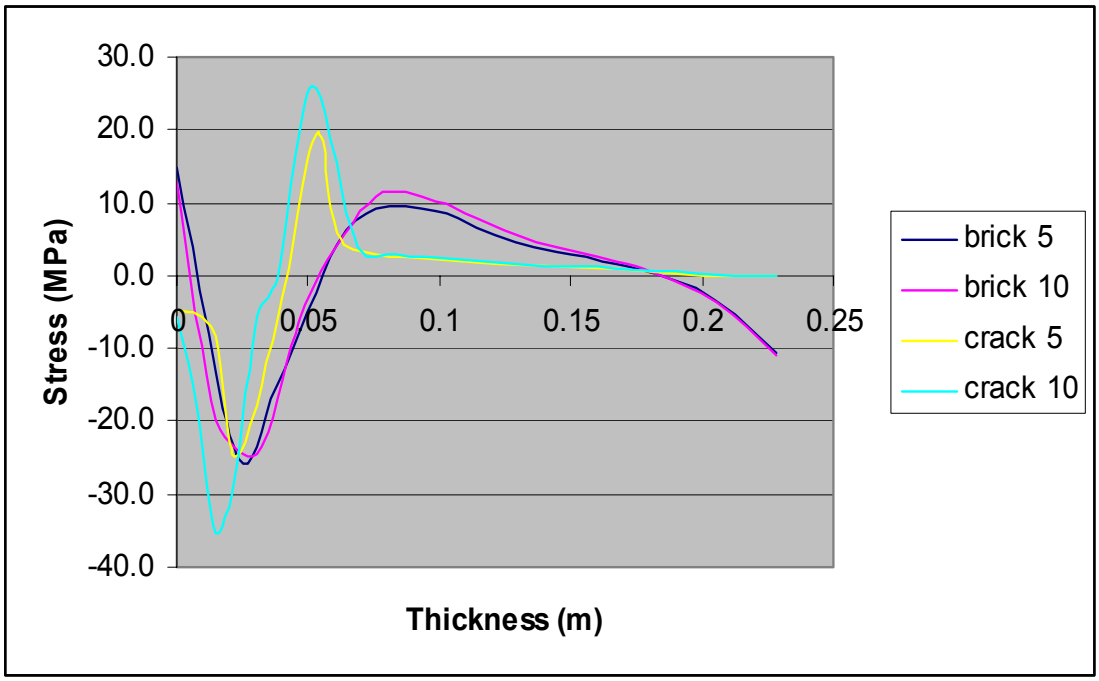

Figure 5.8. Through thickness tangential stress diagram after initial heat up

The radial stress distribution and through thickness radial stress diagram of the crown after initial heat up are given in Figure 5.9 and Figure 5.10, respectively.

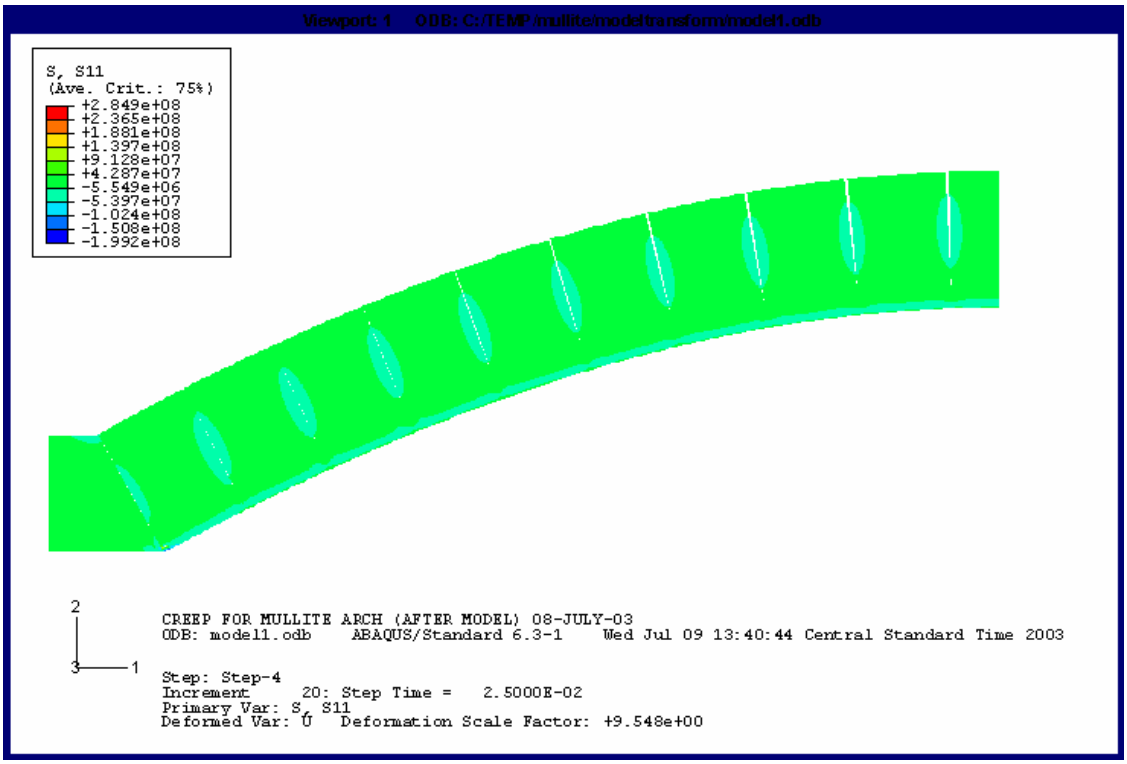

Figure 5.9. Radial stress distribution in the crown after initial heat up

Brick joints opening has no big effects on the radial stress developed in the crown. Compressive radial stress is developed along the crack plane except near the crack tip area, tensile stress is developed in the opened portion and compressive stress is developed in the unopened portion inside the bricks. The crack tip areas along the crack planes also experience highest tensile stresses. This result agrees with the results of Schacht and Hribar[30] again. The stresses inside the bricks are between 10 MPa and -15 MPa. The compressive stresses along the crack planes are less than 20 MPa, the tensile stresses around crack tips can reach 35 MPa.

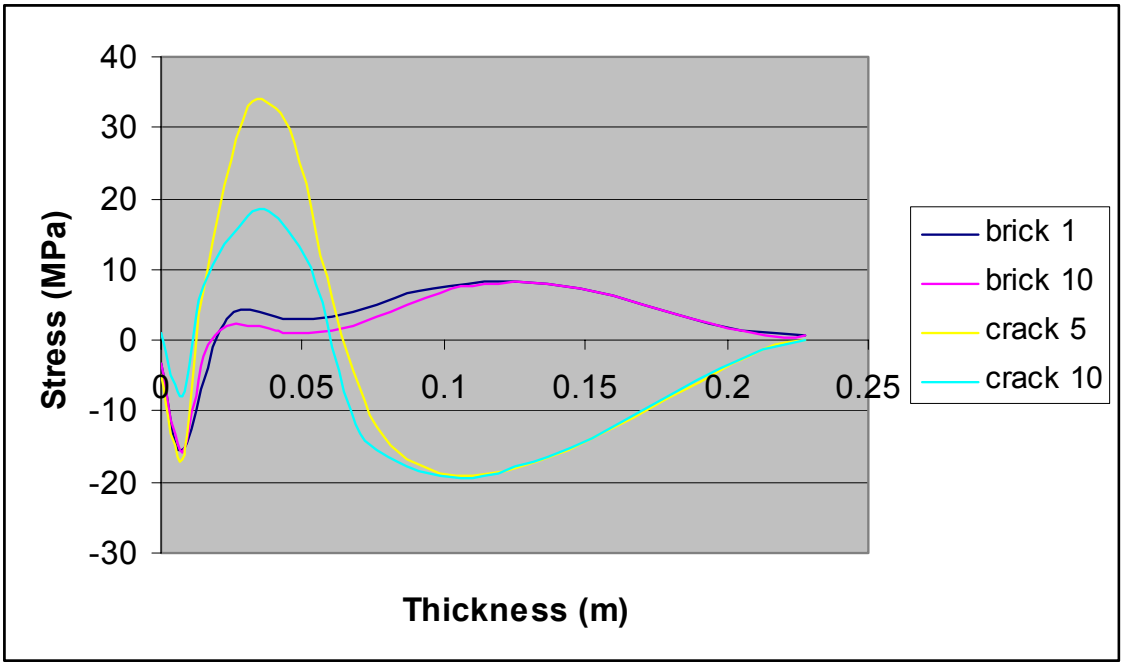

Figure 5.10. Through thickness radial stress diagram after initial heat up

5.2.4 Strain in the Crown During Heat Up. The strains in the crown are induced due to the stresses in the crown and the thermal expansion.

The tangential strain distribution and through thickness tangential strain diagram of the crown after initial heat up are given in Figure 5.11 and Figure 5.12, respectively. Refer to Figure 4.3 and Figure 5.6 for the locations of bricks and cracks, respectively.

Positive tangential strains are developed in the whole crown. The tangential strains developed inside the bricks decrease through the crown thickness from the hot face to its cold face. Because of the effects of high compressive stress developed along the brick contact surfaces, the tangential strains on the bricks contact surfaces unopened portion are less than the strain inside the unopened portion of bricks. Also, because the

brick corners are free of compression, the highest tangential strain occurs on the hot face along contact surface.

The strains developed both inside the bricks and on the contact surfaces except the brick corners are almost in the same range; they are from 0.0115 on the hot face to 0.0095 on the cold face. The results show that thermal expansion is the main source of strain. Compressive stress affects strain distribution in the unopened portion of the bricks.

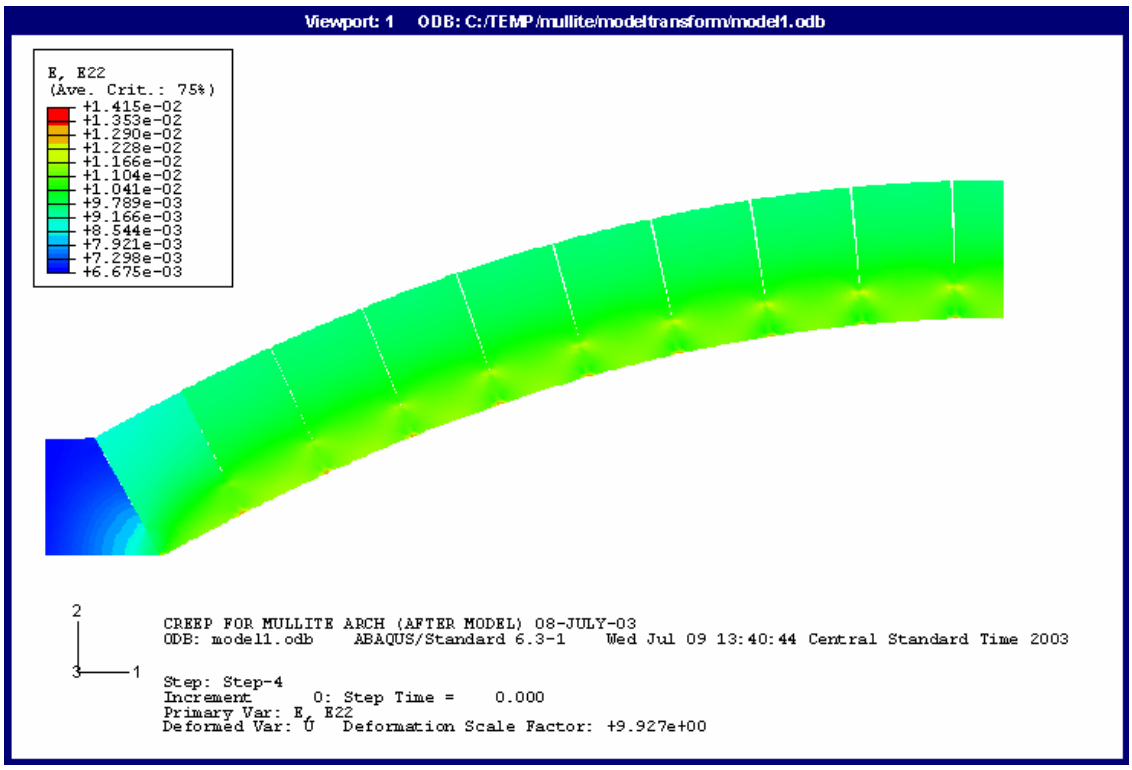

Figure 5.11. Tangential strain distribution after initial heat up

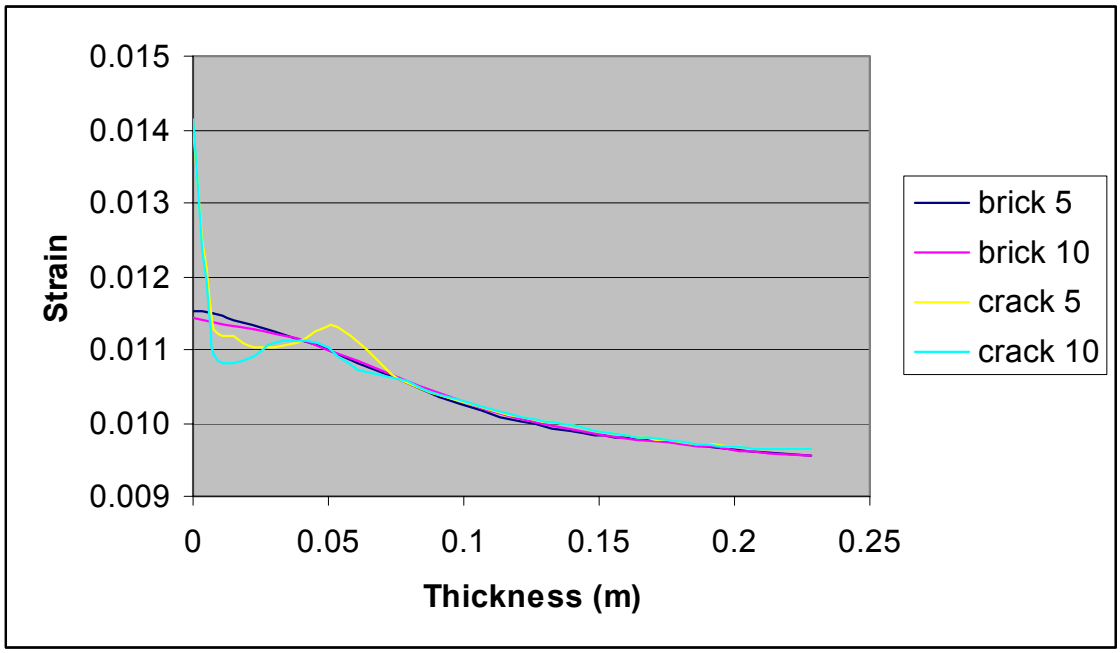

Figure 5.12. Through thickness tangential strain after initial heat up

The radial strain distribution and through thickness radial strain diagram of the crown after initial heat up are given by Figure 5.13 and Figure 5.14, respectively. Refer to Figure 4.3 and Figure 5.6 for the locations of bricks and cracks, respectively.

Positive radial strains are developed in the whole crown as well. The radial strains developed inside the bricks decrease through the crown thickness from the hot face to its cold face at a higher rate than the tangential strain. Due to the effects of the shape of the brick corners, the hot face radial strain along the contact surfaces is smaller than that of the hot face. Except the brick corners, the radial strains developed both inside the bricks and on the contact surfaces are within the same range, they are about 0.014 on the hot face and around 0.0095 on the cold face.

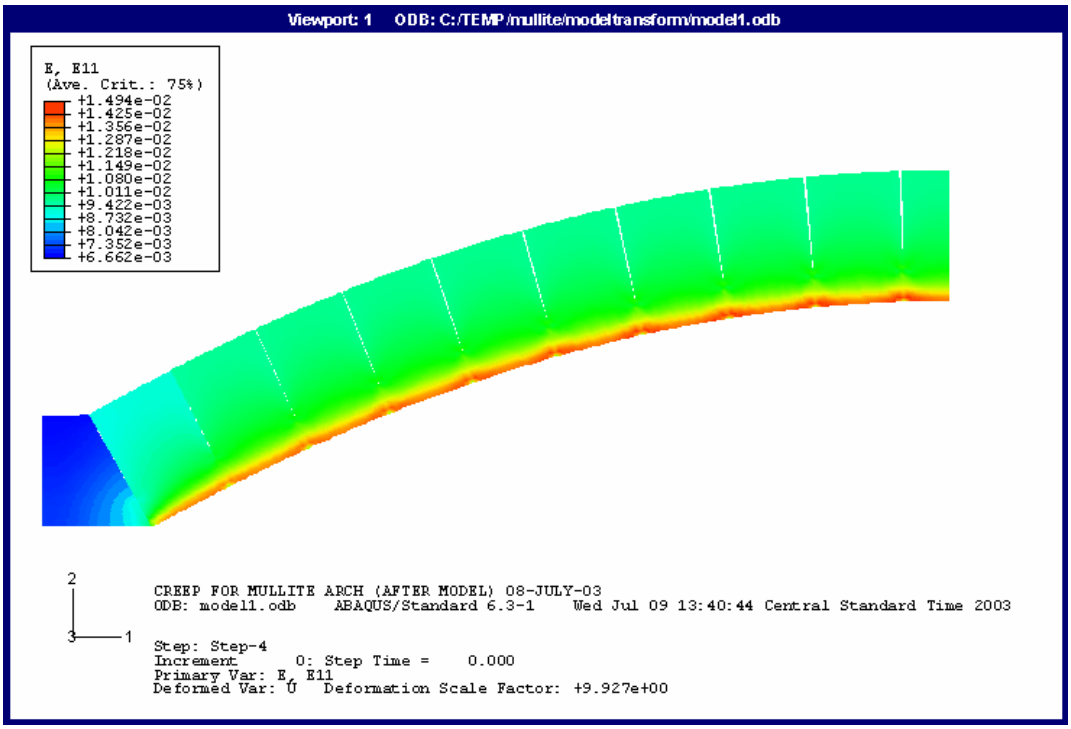

Figure 5.13. Radial strain distribution after initial heat up

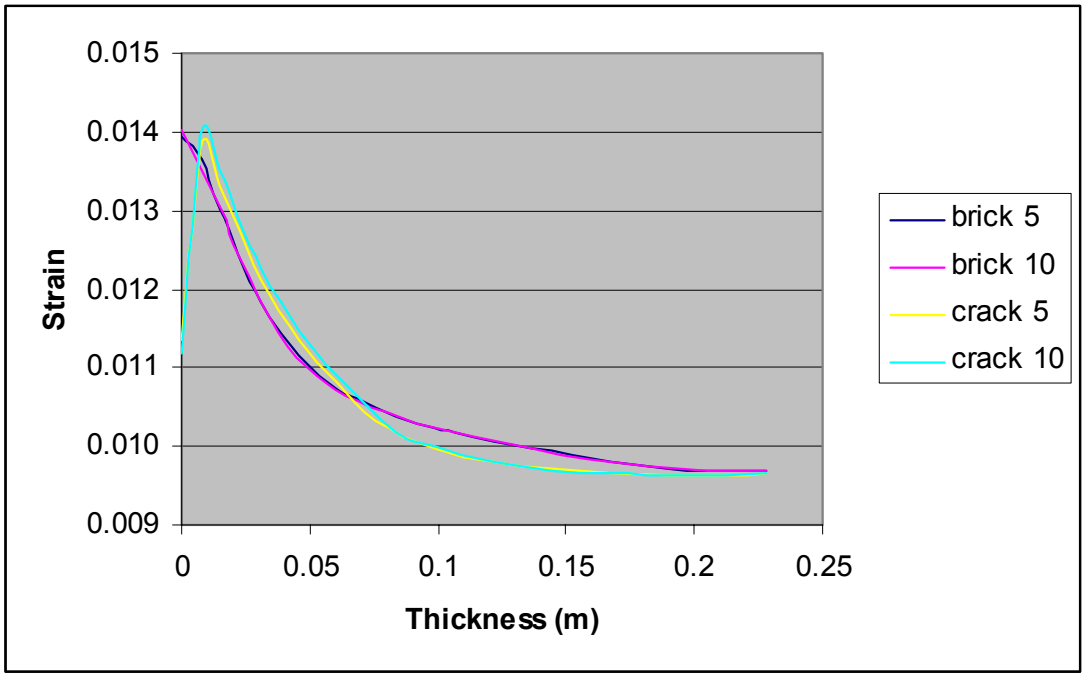

Figure 5.14. Through thickness radial strain after initial heat up

5.2.5 Time Dependent Performance. Creep is one of the dominant factors in the failure of refractories exposed to high temperature environment. The creep behavior of refractories will cause significant stress relief after the initial heat up. As a result, the crown will continually deform after initial heat up. So the time dependent stress, strain and the displacement curves are important to help to understand the performance of glass furnace crown.

Hot face tangential and axial stress versus time curves after initial heat up are given in Figure 5.15 and Figure 5.16, respectively.

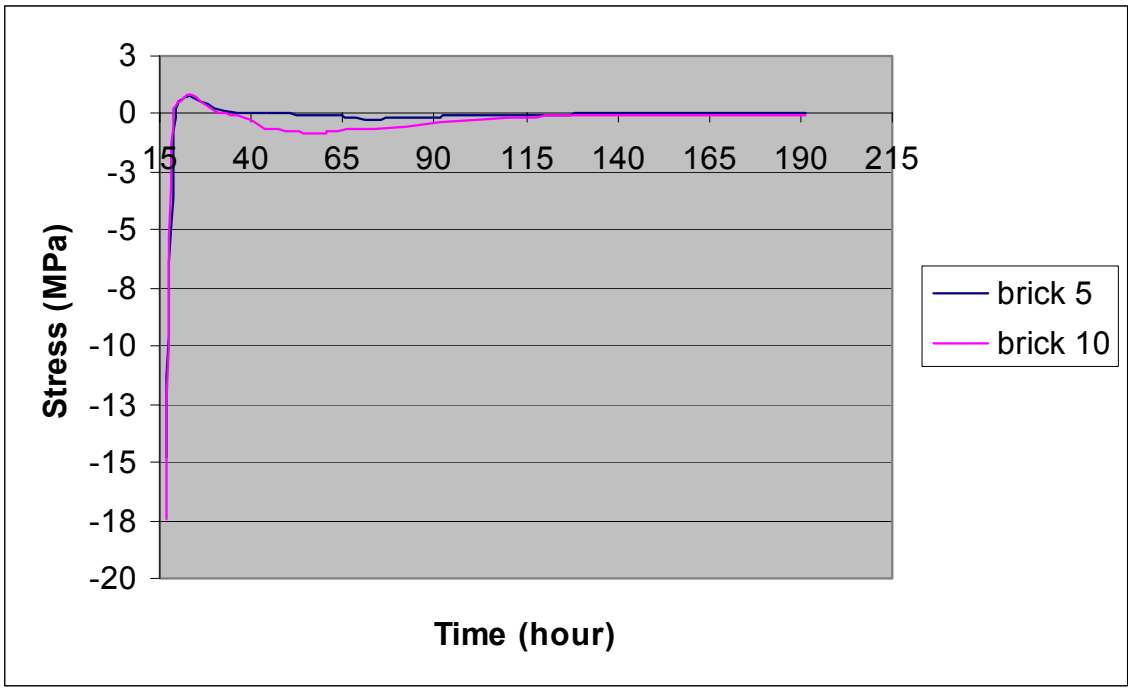

Figure 5.15. Hot face tangential stress relaxation

Both tangential and radial stresses release rapidly after initial heat up. The bricks undergo a compressive tangential stressed period after the stress relief until about 120 hour's service of the crown, the compressive stress in brick 10 is about 1 MPa , the stress in brick 5 is about 0.3 MPa , and then the tangential stress almost vanishes. The radial stress in the bricks reaches steady state earlier then the tangential stress, the stresses range from -0.03 MPa to 0.8 MPa after stress relief, and then almost vanish after 120 hours.

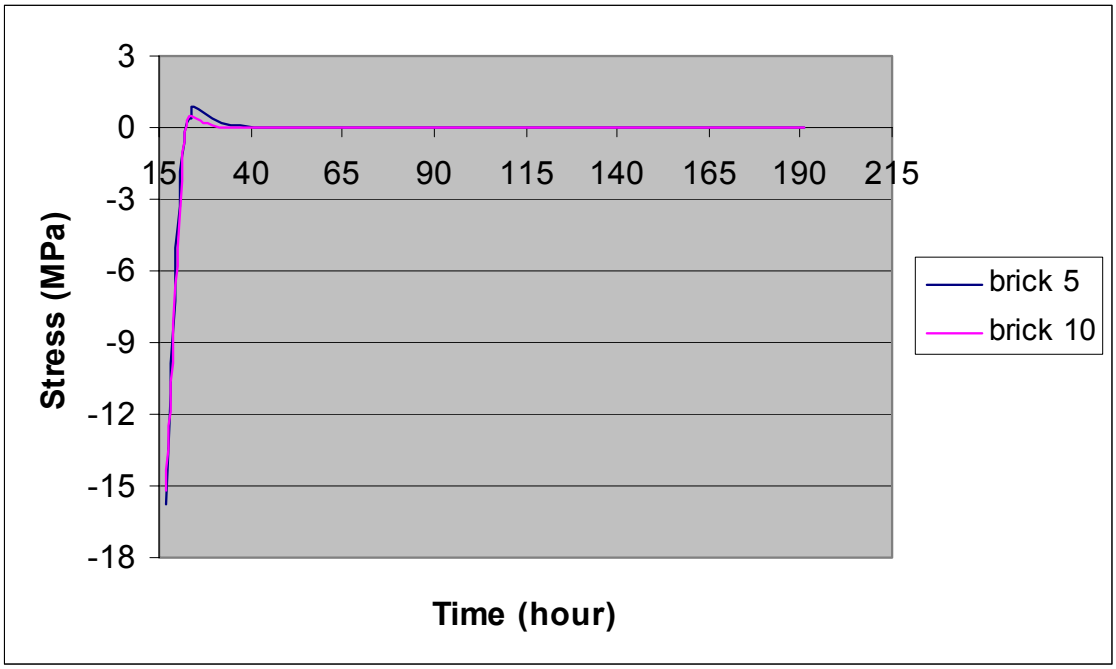

Figure 5.16. Hot face radial stress relaxation

Hot face accumulated strains in the tangential and axial directions started from the beginning of initial heat up are given in Figure 5.17 and Figure 5.18, respectively. Refer to Figure 4.3 and Figure 5.6 for the locations of bricks and cracks, respectively.

The results show that, hot face accumulated tangential strains increase gradually during initial heat up which is about 20 hours. The strains in different bricks are within the same range during this period. Thermal expansion is the main driving factor for the strains during initial heat up. After initial heat up, the stresses in the bricks cause the strains to change, the tangential strains continue to increase first as the high compressive stresses release, and then begin to decrease during the compressive tangential stress period. The accumulated tangential strains reach a steady state after 120 hours when the stresses vanish. Brick 10 has a higher creep strain rate and a lower steady state strain than brick 5, since brick 10 has higher compressive stress than brick 5.

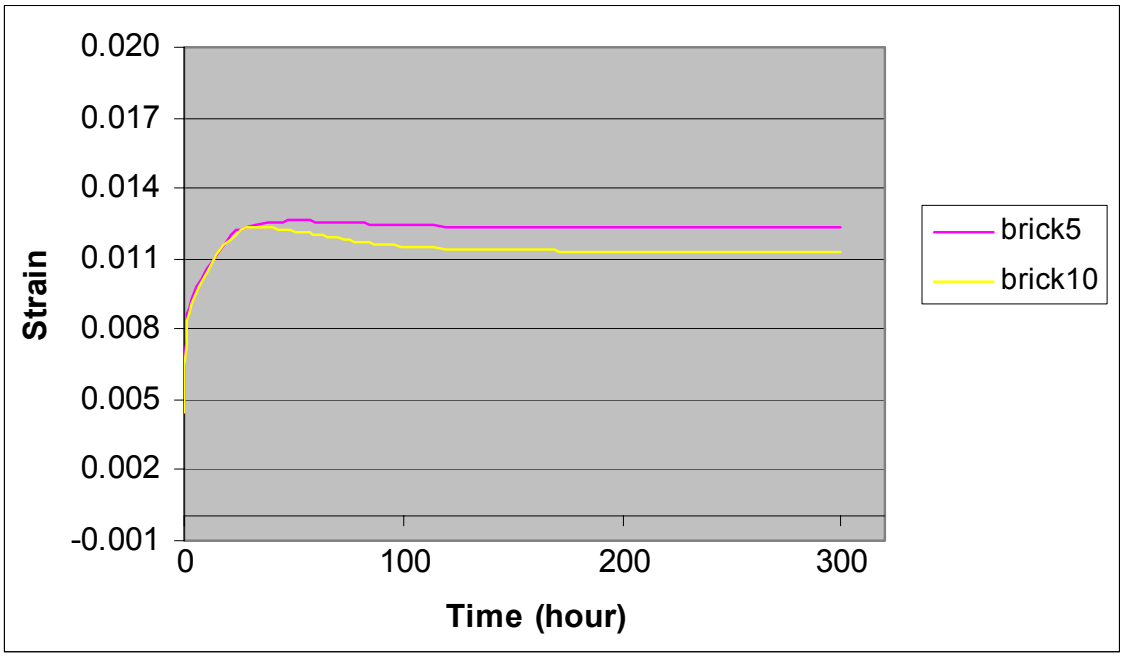

Figure 5.17. Hot face accumulated tangential strain

Hot face accumulated radial strains increase gradually during initial heat up as well. The strains in different bricks almost have the same range at about 0.01. Temperature is the main source of the strains during initial heat up. After initial heat up, the change of radial strain follows the change of radial stress. As the compressive radial stresses release rapidly, the radial strains increase rapidly; when the radial stresses are within a small tensile range, the radial strains increase slowly, the radial strains reach a steady state after 120 hours as the stress vanish.

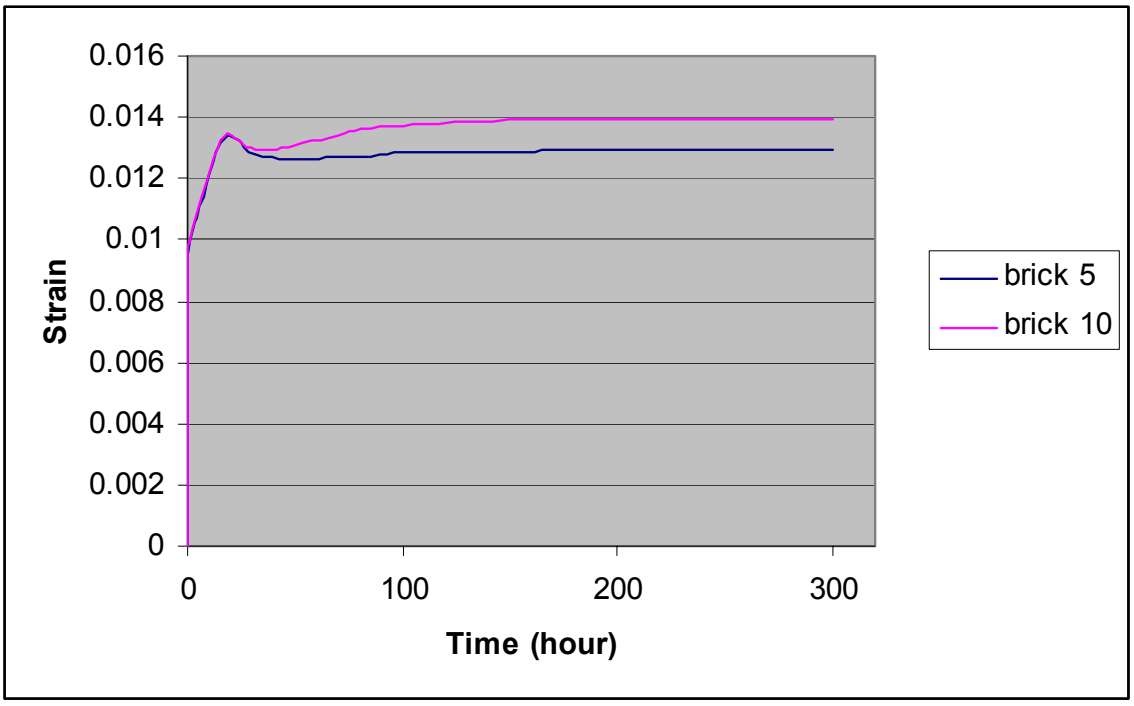

Figure 5.18. Hot face accumulated radial strain

The compressive creep strain from the model deviates somewhat from the experimental strain curve. This is because the real crown operational environment is

significantly different from that of the experimental condition. In the experiment, stress controlled creep test under constant temperature is conducted for single bricks. That is, the bricks are tested under constant pressure and there are no temperature gradients in the bricks. In the real glass tank crown, however, the crown consists of several bricks. The bricks interact with each other during service. The temperature changes through the thickness of bricks unlike in the single brick experiment. Also, the bricks open from their cold face joints. As a result, various stresses are developed in the bricks and the stresses developed in the crown are much higher than those of the single brick experiment.

Figure 5.19 gives the crown center displacement curves. The crown center displaces upwards gradually during initial heat up.

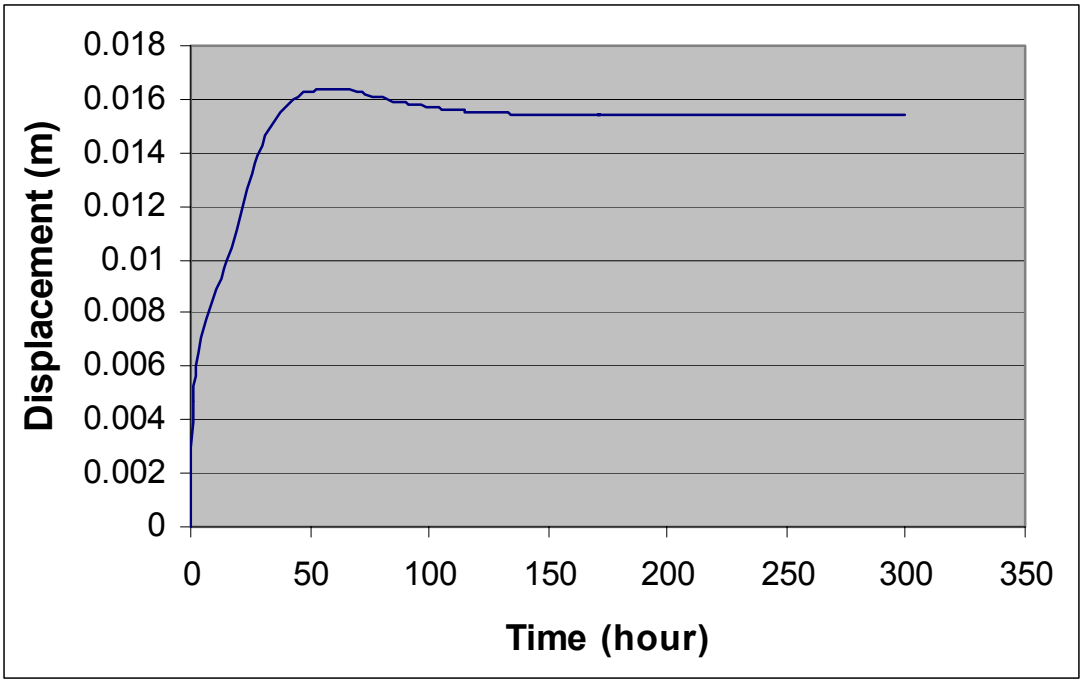

Figure 5.19. Crown center vertical displacement versus time curve

Because of the noticeable stress relief, the crown continues to move up at a higher rate after initial heat up. The displacement reaches the highest value of approximately 0.0166 m at around 60 hours, then runs down slightly and reaches its steady state, after about 120 hours as the stress vanish. Steady state crown center displacement is about 0.0155 m. The displacement of the crown is very small in comparison to its size.

All the results discussed above, the temperature field, the brick joint opening, and the rise of the crown from the model are similar to the reaction of the crown observed experimentally and industrially.

6. CONCLUSIONS

A coupled temperature-displacement, nonlinear finite element method is applied to investigate the compressive creep performance of single brick exposed to high temperature environment. After validating, the model is used to simulate the operating environment of glass furnace crown. Generally, the full scale tests of glass furnace crown operation are hard, prohibitively expensive and time consuming. A finite element modeling and simulation of the crown on the other hand would be economical and cost reductive. Symmetric 2D finite element modeling of glass furnace crown provides an effective finite element tool to evaluate the heat transfer, the thermo-mechanical and creep performance of glass furnace crown exposed to hightemperature environment and long term service. This model is helpful for understanding the performance of crown. Thereby help to select the crown refractories, optimize the crown geometry and estimate the expected glass furnace lifetime. This model will also help furnace operators to operate the glass furnace in a more efficient mode in the future.

The results show that, the temperature in the crown increases evenly from cold face to hot face through the thickness of the arch.

High temperature causes the crown to expand. Temperature gradients result in differential expansion through the thickness of bricks thereby resulting in very high stresses in the crown. Differential expansion and the high stresses in the crown cause brick joints to open from the crown cold face to hot face during initial heat up. Crown hot face is the most compressed area, crack tip regions have the highest tensile stresses during the initial heat up. After the initial heat up, significant stress relaxation occurs due

to creep behavior of the refractory materials. The stresses vanish in about 120 hours of service.

Crown hot face has the highest strain after initial heat up. Hot face strains increase gradually during the initial heat up. After the initial heat up, the strains increase slightly first and then begin to decrease, eventually reaching a steady state after about 120 hours. The steady state stress is almost zero.

The crown moves up slightly during initial heat up. The creep causes the crown to run up continually after initial heat up first, and then drop down slightly. The crown center displacement reaches its highest value of approximately 0.0166 m at around 60 hours of service. The crown reaches its steady state after about 120 hours of service. The steady state crown center displacement is about 0.0155 m. The displacement of the crown is very small in comparison to its size.

7. FUTURE WORK

Here, it has been shown that symmetric 2D simulation of glass furnace crown provides an effective finite element tool to investigate the thermo-mechanical and creeping performance of glass tank crown exposed to high temperature environment without corrosion. However, the corrosion of crown materials must be considered to simulate the realistic glass furnace crown operating condition. Further, size effect of the crown and use of different refractories materials need to be considered in the model. This will facilitate the optimization of the crown geometry and the selection of crown refractories. The FEA data should be validated, if at all possible, with the experimental results.

BIBLIOGRAPHY

1. C. P. Ross, "Looking Beyond the 'Oxy-Fuel Issues for Glassmaking in the 90s' Workshop," Ceram. Eng. Sci. Proc., 19[1] pp. 89-98, (1998)

2. E. D. Silva, Y. Bourhis, J. Y. Iatrides, B. Jurcik, B. V. Drasek and R. Ruiz, "Individual Oxy-Fuel Benefits Should Be Clear Before Conversion," Glass Industry, 76[9] pp. 8-12, (1995)

3. R. D. Moore and J. T. Brown, "Conversion of a Large Container furnace from Regenerative Firing to Direct Oxy-Fuel Combustion," Ceram. Eng. Sci. Proc., 13[3-4] pp.18-24, (1992)

4. M. Gridley, "Philosophy, Design, and Performance of Oxy-Fuel Furnace," Ceram. Eng. Sci. Proc., 18[1] pp. 1-13, (1997)

5. X. Buttol, R. Dramais and D. Gunn, "Refractories for Superstructures in Oxy-Fuel Fired Glass Furnaces: Are All Silica Products Equivalent?" Ceramic Engineering & Science Proceeding, 21[1] pp. 251-262, (2000)

6. G. Duvierre, A. Zanoli, Y. Boussant-Roux and M. Nelson, "Selection of Optimum Refractories for the Superstructure of Oxy-Fuel Glass Melting Furnaces," Ceram. Eng. Sci. Proc., 18[1] pp. 147-163, (1997)

7. H. T. Godard, L. H. Kotacska, J. F. Wosinski, S. M. Winder, A. Gupta, K. R. Selkregg and S. Gould, "Refractory Corrosion Behavior under Air-Fuel and Oxy-Fuel Environments," Ceram. Eng. Sci. Proc., 18[1] pp. 181-207, (1997)

8. A. A. Wereszczak, "Which superstructure refractories do glass makers desire creep data for?" Glass industry, pp. 17-18, November (1998)

9. G. Frohlich, "A Fused Silica Pumpable Refractory for Crown Damage Resulting from Oxy-Fuel Firing," Ceram. Eng. Sci. Proc., 20[1] pp. 107-113, (1999)

10. A. Gupta and S. M. Winder, " Testing Oxy-Fuel Furnace Crown Materials," Glass, 73[7] pp. 260-262, (1996)

11. L. H. Kotacska and T. J. Cooper, "Testing of Superstructure Refractories in a Gas-Oxy Atmosphere Against High-Alkali Glasses," Ceram. Eng. Sci. Proc., 18[1] pp. 136-145, (1997)

12. J. Leblanc, A. Burgunder, A. Gupta and S. Hope, "Performance and Economics of Furnace Crowns for Oxy-Fuel Glass Melting," Ceram. Eng. Sci. Proc., 21[1] pp. 237-249, (2000)

13. A. J. Faber and O. S. Verheijen, "Refractory Corrosion Under Oxy-Fuel Firing Conditions," Ceram. Eng. Sci. Proc., 18[1] pp. 109-119, (1997)

14. J. Boillet, W. Kobayashi, W. J. Snyder, C. A. Paskocimas, E. R. Leite, E. Longo and J. A. Varela, "Corrosion of Silica and Mullite Refractories Used in Glass Furnace Under 100% Oxy-Firing Process," Ceram. Eng. Sci., 17[2] 180-188, (1996)

15. I. N. W. Shulver, "Silica Refractories in the Glass Industry," Glass Technology, 29[5] pp. 170-173, (1988)

16. A. A. Wereszczak, M. Karakus, K. C. Liu, B. A. Pint, R. E. Moore and T. P. Kirkland, "Compressive Creep Performance and High Temperature Dimensional Stability of Conventional Silica Refractories," Oak Ridge National Laboratory Internal Report, (ORNL/TM-13757), 1999

17. A. A. Wereszczak, T. P. Kirland and W. F. Curtis, "Creep of CaO/SiO_2-Containing MgO Refractories," J. of Materials Science, 34 pp. 215-227, (1999)

18. J. G. Hemrick, and A. A. Wereszczak, M. Karakus, K. C. Liu, H. Wang, B. A. Pint, T. P. Kirkland and R. E. Moore, "Compressive creep and thermophysical performance of mullite refractories," Oak Ridge National Laboratory Internal Report, (2000)

19. J. G. Hemrick, "Creep Behavior and Physical Characterization of Fusion-Cast Alumina Refractories," PhD Dissertation, University of Missouri-Rolla, 2001

20. A. Gupta and D. Clendenen, "Observations for Field Experience with Fused Alumina Crowns," Ceram. Eng. Sci. Proc., 22[1] pp. 91-103, (2001)

21. C. Windle, "Rebonded Magnesia-Alumina Spinel the Oxy-Fuel Solution," International Ceramic, 1 pp. 41-43, (2000)

22. G. Boymanns, F. Gebhardt, M. Dunkl, and H. D. Schlacht, "Spinel bricks for highly stressed roofs in glass melting furnaces," Glasstech, 72[10] pp. 293-298, (2000)

23. S. C. Carniglia and G. L. Barna, "Handbook of Industrial Refractories Technology," NOYES Publications, (1992)

24. F. V. Tooley, " The Handbook of Glass Manufacture," 3rd Edition, Ashlee Publishing Co., Inc., (1984)

25. J. M. Sponn, "Calculation of Stresses in Glass Yank Refractories Via Numerical Modeling," Master Thesis, Alfred University, (1992)

26. M. R. Geise, "Prediction of Thermal Stresses and Safe Heating Rates for Fusion-Cast AZS Refractory Block Using Finite Element Analysis," Master Thesis, Alfred University, (1994)

27. M. Koyuncu and W. B. Carlson, "Numerical Calculation of Stresses in Glass Tank Refractories," The Glass researcher: bulletin of glass science and engineering, 7[2] pp. 4-5, (1998)

28. "ABAQUS/Standard User's Manual," Volume 1, Version 6.3

29. "Refractories Handbook," The Technology Association of Refractories, Japan, (1998)

30. C. A. Schacht, "Refractory Linings," Marcel Dekker, Inc., (1995)

31. R. B. Hetnarski, "Thermal Stresses I," Elsevier Science Publications B.V. ,(1986)

32. Y. A. Cengel and R. H. Turner, "Fundamentals of Thermal-Fluid Sciences," McGraw-Hill Higher Education, (2001)

33. T. L. Anderson, "Fracture mechanics – fundamentals and applications," 2nd ed., CRC Press, (1995)

34. W. N. Findley, J. S. Lai, and K. Onaran, "Creep and Relaxation of Nonlinear Viscoelastic Materials," Dover Publications, Inc. (1989)

35. D. Munz, T. Fett, "Ceramics," Springer-Verlag Berlin Heidelberg, (1999)

36. J. B. Wachtman, "Mechanical Properties of Ceramic," JOHN WILEY & SONS, INC. (1996)

37. M. E. Green, "Compressive Creep of Basic Refractories," Master Thesis, University of Missouri-Rolla, (1968)

38. B. S. Monton, "Compressive Creep of Magnesium-Aluminate Spinel Synthesized from Natural Raw Materials for Refractory Applications," Master Thesis, University of Missouri-Rolla, (1998)

39. T. J. Chung, "Continuum Mechanics," Prentic Hall, (1988)

40. R. B. Hetnarski, "Thermal Stresses II," Elsevier Science Publications B.V.,(1986)

VITA

Xiaoting Liang was born on October 11, 1977 in Panjin City, Liaoning Province, China. He completed his high school education in Panjin, China. After finishing high school, he completed his Bachelors of Engineering in Chemical Engineering from Tianjin University, China in June of 1997. Then, he worked as a mechanical engineer in Beijing Yanshan Petrochemical Company until 2001. He enrolled at the University of Missouri-Rolla for the Masters Program in Engineering Mechanics in the fall of 2001. He received his MS degree in August 2003.

During his tenure as a graduate student, he held positions of graduate teaching assistant in the fall of 2001 and the winter of 2002 and graduate research assistant in the Department of Ceramic Engineering until now.